Towards Single-Ion Detection and Single-Photon Storage in Rare-Earth-Ion-Doped Crystals

Alqedra, Mohammed

2022

Document Version:
Publisher's PDF, also known as Version of record

Link to publication

Citation for published version (APA):
Alqedra, M. (2022). *Towards Single-Ion Detection and Single-Photon Storage in Rare-Earth-Ion-Doped Crystals*. Atomic Physics, Department of Physics, Lund University.

Total number of authors:
1

LUND UNIVERSITY

PO Box 117
221 00 Lund
+46 46-222 00 00

TOWARDS SINGLE-ION DETECTION AND SINGLE-PHOTON STORAGE IN RARE-EARTH-ION-DOPED CRYSTALS

Mohammed Alqedra

Doctoral Dissertation
2022

SIGILLVM UNIVERSITATIS CAROLINÆ GOTHORVM
1666

Towards Single-Ion Detection and Single-Photon Storage in Rare-Earth-Ion-Doped Crystals

Mohammed Alqedra

LUND
UNIVERSITY

Thesis for the degree of Doctor of Philosophy
Thesis advisors: Dr. Andreas Walther, Prof. Stefan Kröll
Faculty opponent: Dr. Harald Schwefel

With the permission of the Faculty of Engineering at Lund University, the thesis will be publicly defended on Friday, the 3rd of June 2022, at 9.15 a.m. in Rydberg's hall, at the Department of Physics, Professorsgatan 1, Lund.

Organization
LUND UNIVERSITY

Division of Atomic Physics
Department of Physics
Box 118
SE–221 00 Lund
Sweden

Document name
DOCTORAL DISSERTATION

Date of disputation
2022-06-03

Sponsoring organization

Author
Mohammed Alqedra

Title and subtitle
Towards Single-Ion Detection and Single-Photon Storage in Rare-Earth-Ion-Doped Crystals

Abstract

Solid materials doped with rare-earth ions are considered an attractive platform for quantum information applications. One of the main reasons for this is the exceptionally long optical and hyperfine coherence times of the $4f^n$ states, due to the shielding provided by the outer lying 5s and 5p electrons. This enables a large number of quantum operations before the system loses its coherence. Another reason is the wide inhomogeneous line broadening ($\sim$ GHz), compared to the narrow homogeneous linewidth of individual ions ($\sim$ kHz), which gives rise to a large number of spectrally separated ions that can, in principle, be individually addressed. In order to make use of this feature, a reliable detection (readout) of single ions is required. The excited states of $4f - 4f$ transitions have relatively long lifetimes ranging from hundreds of microseconds to milliseconds. This leads to a low spontaneous emission rate, which renders a direct detection of an individual ion challenging.

Part of the research presented in this thesis addresses this issue by utilizing the Purcell effect to enhance the spontaneous emission rate of the ions. This can be achieved by placing nanocrystals doped with rare-earth ions inside a microcavity. The density of states inside the cavity is modified compared to the density of states in free space, and as a consequence, the lifetime of the excited state of the ion becomes shorter. Y_2O_3 nanocrystals doped with Nd^{3+} ions were investigated, the Nd^{3+} ions being candidate for a readout ion that could potentially be used to probe the state of co-doped qubit ions in a non-destructive measurement. A fiber based microcavity was constructed for use at cryogenic temperatures. A side of fringe locking scheme was implemented to increase the stability of the cavity. Scanning cavity microscopy was demonstrated and used at room temperature to locate the nanocrystals, and cavity coupling to the $4f - 4f$ transitions of the Nd^{3+} ions was achieved. Cryogenic measurements were performed and cavity enhanced detection of an ensemble of a few ions was demonstrated.

Another part of this research was focused on quantum memories. A quantum memory capable of storing a single photon and being able to retrieve it on demand with high fidelity are necessary for long distance quantum communication. The atomic frequency comb (AFC) scheme is an interesting quantum memory schemes that has been routinely demonstrated in rare-earth-ion-doped systems. To achieve on-demand storage, the standard AFC scheme is usually combined with bright optical pulses to transfer a stored photon into and out of the spin levels; referred to as the spin-wave storage scheme. However, these bright pulses create a high optical background, which makes it challenging to store and recall single photons. In this thesis, an extension of the standard AFC protocol that utilizes the linear Stark effect to perform noise-free, on-demand storage without the need for spin transfer pulses, is presented. The modified protocol was experimentally implemented in Pr^{3+}:Y_2SiO_5 using weak coherent states as a memory input. A signal-to-noise ratio (SNR) of 570 was achieved using an average of 0.1 photons per pulse for storage, limited by the detector dark current. An order of magnitude higher SNR was estimated for storage of single-photon Fock states. This SNR, to the best of the author's knowledge, is unsurpassed for the presented technique. A standard AFC analytical model was modified to incorporate the presented technique technique, and to investigate the storage performance of other materials for practical use in quantum networks. The Stark shift technique was also combined with the spin-wave storage scheme, providing another tool that could improve the performance of spin-wave storage at the single-photon level.

Key words

Single-ion detection, microcavities, quantum memory, rare-earth-ion-doped crystals

Classification system and/or index terms (if any)

Supplementary bibliographical information

Language
English

ISSN and key title
0281-2762, Lund Reports on Atomic Physics, LRAP-581

ISBN
978-91-8039-249-5(print)
978-91-8039-250-1(pdf)

Recipient's notes

Number of pages
157

Price

Security classification

I, the undersigned, being the copyright owner of the abstract of the above-mentioned dissertation, hereby grant to all reference sources the permission to publish and disseminate the abstract of the above-mentioned dissertation.

Signature ________________ Date 2022-04-27

Towards Single-Ion Detection and Single-Photon Storage in
Rare-Earth-Ion-Doped Crystals

Faculty of engineering
Department of Physics
Lund University

ISBN 978-91-8039-249-5(print)
ISBN 978-91-8039-250-1 (pdf)
ISSN: 0281-2762

Printed in Sweden by Media-Tryck, Lund University
Lund, 2022

NORDIC SWAN ECOLABEL
Printed matter
3041 0903

Media-Tryck is a Nordic Swan Ecolabel
certified provider of printed material.
Read more about our environmental
work at www.mediatryck.lu.se

MADE IN SWEDEN

ABSTRACT

Solid materials doped with rare-earth ions are considered an attractive platform for quantum information applications. One of the main reasons for this is the exceptionally long optical and hyperfine coherence times of the $4f^n$ states, due to the shielding provided by the outer lying 5s and 5p electrons. This enables a large number of quantum operations before the system loses its coherence. Another reason is the wide inhomogeneous line broadening ($\sim$ GHz), compared to the narrow homogeneous linewidth of individual ions ($\sim$ kHz), which gives rise to a large number of spectrally separated ions that can, in principle, be individually addressed. In order to make use of this feature, a reliable detection (readout) of single ions is required. The excited states of $4f-4f$ transitions have relatively long lifetimes ranging from hundreds of microseconds to milliseconds. This leads to a low spontaneous emission rate, which renders a direct detection of an individual ion challenging.

Part of the research presented in this thesis addresses this issue by utilizing the Purcell effect to enhance the spontaneous emission rate of the ions. This can be achieved by placing nanocrystals doped with rare-earth ions inside a microcavity. The density of states inside the cavity is modified compared to the density of states in free space, and as a consequence, the lifetime of the excited state of the ion becomes shorter. Y_2O_3 nanocrystals doped with Nd^{3+} ions were investigated, the Nd^{3+} ions being candidate for a readout ion that could potentially be used to probe the state of co-doped qubit ions in a non-destructive measurement. A fiber based microcavity was constructed for use at cryogenic temperatures. A side of fringe locking scheme was implemented to increase the stability of the cavity. Scanning cavity microscopy was demonstrated and used at room temperature to locate the nanocrystals, and cavity coupling to the $4f-4f$ transitions of the Nd^{3+} ions was achieved. Cryogenic measurements were performed and cavity enhanced detection of an ensemble of a few ions was demonstrated.

Another part of this research was focused on quantum memories. A quantum memory capable of storing a single photon and being able to retrieve it on demand with high fidelity are necessary for long distance quantum communication. The atomic frequency comb (AFC) scheme is an interesting quantum memory schemes that has been routinely demonstrated in rare-earth-ion-doped systems. To achieve on-demand storage, the standard AFC scheme is usually combined with bright optical pulses to transfer a stored photon into and out of the spin levels; referred to as the spin-wave storage scheme. However, these bright pulses create a high optical background, which makes it challenging to store and recall single photons. In this thesis, an extension of the standard AFC protocol that utilizes the linear Stark effect to perform noise-free, on-demand storage without the need for spin transfer pulses, is presented. The modified protocol was experimentally implemented in Pr^{3+}:Y_2SiO_5 using weak coherent states as a memory input. A signal-to-noise ratio (SNR) of 570 was achieved using an average of 0.1 photons per pulse for storage, limited by the detector dark current. An order of magnitude higher SNR was estimated for storage of single-photon Fock states. This SNR, to the best of the author's knowledge, is unsurpassed for the presented technique. A standard AFC analytical model was modified to incorporate the presented technique technique, and to investigate the storage performance of other materials for practical use in quantum networks. The Stark shift technique was also combined with the spin-wave storage scheme, providing another tool that could improve the performance of spin-wave storage at the single-photon level.

POPULAR SCIENTIFIC SUMMARY

In our attempt to understand the universe on a very small-scale, our classical intuition of how things work ceases to apply. Light and matter behaves like nothing we are familiar with from daily experience. During the first half of the last century, a new understanding of nature was developed describing this counter-intuitive behavior of light and matter on the atomic scale, this is now referred to as the First Quantum Revolution. According to this understanding, the behavior of small objects, such as photons and atoms, cannot be predicted with certainty, and at best, we can only estimate the probability that they will behave in certain ways. Today, we are living in the Second Quantum Revolution, in which attempts are being made to utilize the bizarre laws of quantum mechanics to develop new technologies that have the potential to revolutionize our lives and our understanding of the universe. The research described in this thesis is relevant for two such applications, namely, quantum computing and quantum memories.

While a classical computer encodes information using classical 'bits', which work like a switch that can either be ON (1) or OFF (0), a quantum computer uses quantum bits 'qubits' to encode information. A qubit is different from a classical bit in its ability to exist in both the 0 and 1 states at the same time, with different probabilities. This unique and counter intuitive feature is called superposition. This superposition feature is what would make future quantum computers capable of calculations that would be practically impossible using classical computers.

To understand the reason for this, we can compare how much information can be carried by a classical bit with that carried by a qubit. A classical bit carries only one piece of information at a time; either 0 or 1, while a qubit can carry two, corresponding to the probabilities of being in the 0 and the 1 states. In other words, a single qubit carries the equivalent of the information carried by two classical bits. If we scale this up to 300 qubits, 2^{300} classical bits would be required to carry the same amount of information carried by those 300 qubits, which is more than the number of elementary particles in the universe. This paves the way for much more efficient ways of solving certain types of problem much more rapidly than is possible for classical computers. However, superposition states are so fragile that their mere interaction with the surrounding environment could destroy them resulting in a loss of quantum information. The qubits used in this work were rare-earth ions placed inside crystals. These ions have many interesting features that make them interesting for quantum applications. For instance, such materials are capable of preserving quantum information for relatively long times when cooled down to cryogenic temperatures. However, it is very difficult to readout the states of these qubits, as it takes a relatively long time to retrieve the information stored in these ions due to the long lifetime of the excited states. The ability to reliably readout the state of the qubit is necessary to construct a practical quantum computer. The first part of this thesis describes an attempt to tackle the issue with too slow readout. It turns out that by modifying the electromagnetic environment surrounding the ions, it is possible to retrieve the stored information faster, and consequently, making the qubit state more readable. This can be achieved by placing nanocrystals containing the ions between two highly reflective mirrors separated by a few micrometers. By carefully tuning the separation between these two mirrors to specific distances, a resonance of the light emitted by the ions is achieved, and the rate at which the information is retrieved from the ion could be enhanced. The second part of this thesis deals with quantum memories, which is expected to be a crucial for future quantum technologies. Quantum memories are capable of storing quantum information carried by light, and retrieving it after a time set by the user, without destroying the fragile quantum information. Quantum memories are essential for future quantum computers to store information during processing, just as classical memories do in classical computers. Another interesting application that uses quantum memories is long-distance quantum communication. Classically, long-distance communication is achieved by sending light through optical fibers. However, this is associated with considerable losses due to absorption by the fiber. This is compensated for by having components called ‘repeaters’ along the communication path. These components read the information coming from the source, copy it, and resend after amplifying it. However, this can not be done when sending quantum information, as the very act of reading the quantum information, could destroy it. Nevertheless, ‘quantum repeaters’ can achieve the same goal without having to measure or copy the transmitted quantum information. To enable this, a long link is divided into shorter segments with manageable losses that can be connected together if each part can store the communicated information in a quantum memory.

Once again, rare-earth ions stand out as an appealing candidate for quantum storage. In this thesis, an extension to an existing quantum memory protocol is presented, in which electric fields were used as a means of control, allowing the on-demand retrieval of the stored light from the memory. Storage at the single photon level using rare-earth ions was achieved with an unprecedented signal-to-noise ratio. This could help in making long-distance quantum communication a reality.

List of Publications

This thesis is based on the following papers, which will be referred to in the text by their roman numerals.

I **Optical coherence properties of nanoscale Kramers' rare-earth ions for quantum applications**
Mohammed K. Alqedra*, Chetan Deshmukh*, Sebastian P. Horvath, Safi Rafie-Zinedine, Abdullah Abdelatief, Lars Rippe, Stefan Kröll, Andreas Walther, Bernardo Casabone, Hugues de Riedmatten, Diana Serrano, Shuping Liu, Alban Ferrier, Alexandre Tallaire, Hugues de Riedmatten, and Philippe Goldner;
(*Authors contributed equally).
Manuscript in preparation.

II **Noise-free on-demand atomic frequency comb quantum memory**
Sebastian P. Horvath*, Mohammed K. Alqedra*, Adam Kinos, Andreas Walther, Jan Marcus Dahlström, Stefan Kröll, and Lars Rippe;
(*Authors contributed equally).
Phys. Rev. Research **3**, 023099 (2021).

III **Stark control of solid-state quantum memory with spin-wave storage**
Mohammed K. Alqedra, Sebastian P. Horvath, Adam Kinos, Andreas Walther, Stefan Kröll, and Lars Rippe..
Manuscript in preparation.

ABBREVIATIONS

AFC	Atomic frequency comb
AOM	Acousto-Optic modulator
AWG	Arbitrary waveform generator
BSM	Bell-state measurement
CRIB	Controlled Reversible Inhomogeneous Broadening
DOS	Density of states
EIT	Electromagnetic Induced Transparency
EOM	Electro-optic modulator
FBFP	Fiber-based Fabry-Perot
FID	Free induction decay
FPGA	Field programmable gate array
FSR	Free spectral range
FWHM	Full width at half maximum
GEM	Gradient echo memory
PD	Photo diode
PMMA	Poly(methyl methacrylate)
QM	Quantum memory
RASE	Rephased amplified spontaneous emission
REIs	Rare-earth ions
ROSE	Revival Of Silenced Echo
PF	Purcell Factor
SCM	Scanning cavity microscopy
SEM	Scanning electron microscopy
SNR	Signal-to-noise ratio
SPAD	Single-photon avalanche diode
TLS	Two-level system

CONTENTS

Papers

CHAPTER 1

INTRODUCTION

At the end of the 19^{th} century, many scientists thought that most of the fundamental laws of nature had been discovered. A famous quote, attributed to Albert Michelson, captures this era: *"Our future discoveries must be looked for in the sixth place of decimals"*. At the turn of the 20^{th} century, a famous problem, referred to as the "ultraviolet catastrophe" challenged our classical understanding of nature. Classical physics predicted that an ideal black body in thermal equilibrium would radiate more energy at shorter wavelengths (hence the name), in complete contradiction to experimental observations. This was one of the key triggers for the development of quantum mechanics during the first quarter of the 20^{th} century, which resolved the ultraviolet catastrophe, and gave a more fundamental and accurate understanding of the universe.

The peculiar laws of quantum mechanics challenged our classical intuition which is based on the laws of classical physics. Based on the rules of quantum mechanics, the fundamental physical quantities, such as energy and momentum, are quantized, i.e. they can only have discrete values. Furthermore, within the framework of quantum mechanics, physical events are described by probabilistic laws instead of the deterministic ones, which also places a fundamental limit on how accurately we can predict certain physical quantities.

At the heart of quantum mechanics lie two fundamental concepts; the principle of quantum superposition and quantum entanglement. The principle of quantum superposition implies that a quantum object can exist in more than one state at the same time; thus an atom, for example, can be in a superposition state of being both excited and not excited, simultaneously. Quantum entanglement means that two entangled quantum objects cannot be described independently of each other, and regardless of the distance between them, measuring the state of one of them can provide information on the state of the other.

Despite the remarkable scientific and technological progress resulting from our quantum mechanical understanding of nature, the modeling of quantum systems emerged as another big challenge. To fully capture the quantum evolution of a few interacting quantum objects, it is necessary to keep track of every possible configuration of each of the interacting objects. Modeling such systems was found to be extremely difficult using classical computers as the computational power required becomes unrealistically high as the number of the interacting particles increases. Richard Feynman addressed this problem in a lecture he gave in 1981, during which he provided a new insight into the problem, which is summarized by his famous words: *"Nature isn't classical, dammit, and if you want to make a simulation of nature, you'd better make it quantum mechanical, and by golly it's a wonderful problem, because it doesn't look so easy"* [1]. This idea of using controlled quantum systems to simulate other quantum systems, or more generally, harnessing the phenomena of quantum physics to build a more powerful type of computer, initiated efforts directed at constructing quantum computers. A remarkable step in this direction was the quantum algorithm introduced by Peter Shor in 1994 for factoring large numbers [2, 3], which boosted the interest in the field due to the implications of this algorithm on cryptography. By the end of the 20^{th} century, it had become clear that quantum computers would not only enrich our understanding of quantum systems, but would also be able to solve certain problems more efficiently than classical computers. Several factors must be addressed before it will be possible to construct a functional quantum computer. One of these is the ability to preserve the superposition state of the qubit (quantum information unit) during the calculation. This problem is often referred to as decoherence, and the rate at which a superposition state deteriorates is quantified by the coherence time. The difficulty of preserving coherence while manipulating qubits led some physicists to even question the practicality of quantum computers [4, 5]. However, it turned out that it is possible to perform quantum computation reliably despite the decoherence problem by implementing some quantum error-correcting codes [6, 7].

In attempts to overcome the problem of decoherence, several physical systems have been investigated over the past three decades as possible platforms for a quantum computer. Crystals doped with rare-earth ions (REIs) emerged as an interesting platforms thanks to the exceptional optical and spin coherence properties of the $4f-4f$ transitions when cooled to 4 K [8]. This stems from the fact that these inner $4f-4f$ transitions are well shielded by the outer 5s and 5p electrons, which act as a Faraday cage protecting the 4f electrons from the environment. Additionally, the resonance frequency of each ion in a crystal will depend on the surrounding crystal field it is exposed to, which leads to a spread in the resonance frequencies of the ions. This frequency spread is on the order of a few GHz, compared to the much narrower linewidth of individual ions which is on the order of a few kHz. This high density of frequency channels that can be easily addressed by tuning the laser frequency is another feature that makes REIs interesting for quantum computing and quantum applications in general. Another advantage of REI systems is the dipole-dipole interaction between neighbouring ions, which can be used to perform fast logical operations between different qubits.

1.1 Single rare-earth ion readout

One of the challenges of using REI doped crystals for quantum computing is the long excited state lifetime of the $4f-4f$ transitions. This is due to the fact that these transitions are dipole forbidden in a free ion. However, when these ions are doped into a crystal, the crystal field perturbs the ions wave function of the ions and, as a result, the forbidden $4f-4f$ transitions become weakly allowed with an oscillator strength ranging between $10^{-9}-10^{-6}$. The ions ions also will have permanent electric dipole moments in their ground and excited states. The long excited state lifetime leads to low spontaneous emission rates, making it difficult to optically detect (i.e., readout) the state of a single rare-earth qubit ion. An alternative readout scheme has been implemented in which a single qubit is formed from a spectrally narrow ensemble of REIs [9]. However, in this scheme, it is difficult to ensure a large number of ensemble-based qubits that are strongly interacting with each other, making it unscalable. The fast and reliable readout of a single qubit state and the ability to scale the number of qubits are two essential requirements for the realization of quantum computers [10].

Another readout scheme utilizes optical microcavities to enhance the spontaneous emission rate from the excited state of the REI, by modifying the electromagnetic environment surrounding the ion inside the cavity. Using a high finesse cavity with a small volume, the lifetime of some REIs can be shortened by orders of magnitude compared to what it is in free space, leading to an enhanced spontaneous emission rate. The extent of this enhancement is quantified by the Purcell factor. In this scheme, one can either use the cavity to enhance the emission from the qubit ion directly, or from a neighbouring readout ion that interacts with the qubit ion and probes its state in a non-destructive measurement.

1.2 Quantum memory for single photons

Quantum memories are used to store a single photon and retrieve it on-demand without distorting its quantum state (high fidelity)

[11]. The ability to perform this kind of storage plays an important role in many quantum applications. In optical quantum computer schemes, quantum memories are used for signal synchronization such that different quantum operations can be timed appropriately [12, 13]. An on-demand single photon source is another key component of optical quantum computers, which could also rely on optical quantum memories[11]. Another important application utilizing quantum memories is long-distance quantum communication. Signal losses due to absorption and scattering in optical fiber and free space, respectively, prevents the use of these channels for quantum information transmission over long distances. Quantum repeaters can be used to overcome this limitation and enable long-distance quantum key distribution [14], an important component of which is an on-demand high fidelity quantum memory. On-demand retrieval of the stored photons usually requires strong optical pulses, which creates high levels of optical noise, making it challenging to filter out the stored photon from the noise.

1.3 Overview of the thesis work

Two main projects were carried out during the course of this work. The first was an attempt to use a fiber based microcavity to detect single Nd^{3+} ions used to dope a nanocrystal. The second project was carried out to demonstrate single-photon storage in a noise-free quantum memory.

In the first project, Y_2O_3 nanocrystals were doped with Nd^{3+} ions to investigate Nd^{3+} ions as a candidate readout ion. The optical properties of the ions were spectroscopically characterized to assess their suitability for this application. A cryogenic fiber-based Fabry-Perot (FBFP) microcavity was built and tested with the aim of enhancing the spontaneous emission from Nd^{3+} . Scanning cavity microscopy (SCM) was used to locate the nanocrystals, and cavity-enhanced spectroscopy was performed at both room temperature and cryogenic temperature. Although single ion detection was not achieved, a slight enhancement of the emission enabled the detection of an ensemble of a few ions.

In the second project, an extension of the atomic frequency comb (AFC) quantum memory scheme, in which it was combined with the Stark effect, was introduced to enable noise free, and on-demand control of the storage. The scheme was realized experimentally in a Y_2SiO_5crystal doped with Pr^{3+} . The storage of classical light intensities and weak coherent states was achieved with an unprecedented signal-to-noise ratio (SNR). A standard AFC model was modified to incorporate the extension of the memory scheme, and based on the results of the modified model, different materials were investigated to achieve longer storage times. Stark control was also combined with the on-demand spin-wave storage to improve the noise performance of the scheme at the single photons regime.

1.4 Outline of this thesis

The thesis chapters are outlines as follows: Chapters 2 and 3 provide the relevant background on which this work was based on. Chapter 2 presents a brief overview of the spectroscopic properties of REIs, and their potential for quantum computing. Chapter 3 presents the theory of cavity-enhanced light-matter interactions. The strong and weak coupling regimes are described. A brief overview of different microcavity platforms is presented, focusing on the FBFP microcavity. The cavity parameters used throughout the thesis are also defined.

Chapters 4 and 5 present the work performed towards single Nd^{3+} ion detection. Chapter 4 presents the measured spectroscopic properties of Nd^{3+} . The single-ion qubit readout scheme is described and the potential of using Nd^{3+} ions to readout the state of a qubit is discussed. Chapter 5 describes the experimental work performed using the microcavity. This includes a description of the cavity and its components, room temperature characterization of the cavity parameters, SCM, room temperature and cryogenic detection of Nd^{3+} ions.

Chapter 6 and 7 focus on quantum memories. Chapter 6 presents an extension introduced into an existing two-level quantum memory protocol which allows for noise-free, on-demand readout. This extension is based on the Stark shift, which is also discussed in this chapter. In Chapter 7, the experimental realization of the on-demand quantum storage of single photons with an unprecedented SNR is presented. Work towards the application of the Stark extension to a three-level quantum memory (spin-wave storage scheme) is also presented, together with efforts to use the Stark shift to coherently manipulate light using rare earth ions.

Appendix A, presents an overview of a closed-cycle cryostat that was custom made to host the next-generation microcavity.

CHAPTER 2

RARE-EARTH IONS FOR QUANTUM APPLICATIONS

All the experimental work described in this thesis is based on REI-doped crystals. This chapter presents an overview of these ions, highlighting their spectroscopic properties and their potential in quantum computing.

2.1 Spectroscopic properties of rare earth ions

The rare-earth elements comprise the 15 lanthanide elements in the periodic table, starting with lanthium, with an atomic number of 57, and extending to lutetium, with an atomic number of 71, in addition to yttrium and scandium. Rare-earth elements were first discovered in 1787, when Johan Gadolin found a mixture of rare-earth elements, among other elements, in a mineral from a mine in the village of Ytterby in Sweden. This mineral was initially called ytterbite after the village in which it was discovered, and was later given the name gadolinite in memory of Gadolin. A few years later, Gadloin identified the different components of the mineral, and found that 38% was a previously unidentified element, which was given the name yttrium, after the village. Over the next few decades, several elements with similar chemical properties were discovered, and these later formed what are referred to today as the rare-earth elements. Despite their naming, these elements are found at relatively high abundances in the earth's crust. However, it is difficult to chemically extract and isolate them. During the 20^{th} century, rare-earth elements found many interesting applications in lasers, electronics, displays, and many other fields. More recently, REIs have attracted attention as a platform to realize quantum applications such as quantum memories and quantum computers, thanks to their unique spectroscopic properties.

2.1.1 Level structure

The electronic configuration of the lanthanide elements is based on Xe, which has filled 5s and 5p shells. Overall, the electronic configuration can be written [Xe]4f^{n}5d^{m}6s^2, where the 5d shell is empty (m = 0) for all the lanthanide elements apart from for La, Ce, Ga, and Lu, which have one electron in the 5d shell (m = 1). The 4f shell filling ranges from n = 0 to a maximum of 14 electrons. Although the 5s and the 5p shells have lower energy levels than the 4f shell, they are more spatially extended. This 'cloud' of 5s and 5p electrons around the inner 4f shell shields it from the surrounding environment, which is one of the main reasons behind the appealing properties of these ions for quantum applications. In general, lanthanides occur as either doubly (RE^{2+}) or a triply (RE^{3+}) charged ions when used to dope solids. Throughout the this work, insulating crystalline host doped with trivalent REIs have been used. For trivalent RE ions, the electrons are removed from the outer 5d and 6s shells, and the 4f shell is only partially occupied (0-13 electrons). Ions with an odd (even) number of electrons in the 4f shell are called Kramers (non-Kramers) ions. When doping crystals with REIs, the crystal field disturbs the wave functions of the REIs, and as a result, the otherwise forbidden 4f-4f transitions become weakly allowed. These weak 4f-4f transitions are normally very sharp and have good coherence properties, due to the shielding by the outer 5s and 5p shells, as mentioned above. The energy levels of the trivalent REIs were first calculated by Dieke for ions doped in $LaCl_3$ [15], and at a later stage refined by Carnell et al. [16]. Figure 2.1 shows the Dieke diagram for REIs doped in LaF_3 from reference [17]. In the diagram, the different states are labeled as ${}^{2S+1}L_J$, where S is the spin angular momentum, J is the angular angular momentum, and L is the total orbital angular momentum with $L = S, P, D, F, \cdot$, corresponding to 0, 1, 2, 3, $\cdots$. It should be noted that although the crystal field splitting varies from host to host, the overall structures shown in the Dieke diagram are qualitatively similar for other hosts. This is due to the fact that the splitting of the free-ion levels due to the crystal field is generally less than the free-ion level separation.

Suitable doping concentrations of REIs in a crystalline host provides a high density of optically active REIs naturally trapped in the crystal, with spectroscopic properties similar to those of a free ion, but the crystal is much easier to handle than a free-ion. In order to obtain long the coherence times required in quantum information applications, these crystals are cooled to cryogenic temperatures of $\sim$ 4 K. This reduces the density of the crystal lattice phonons, which is one of the main decoherence channels. In all the experiments described in this thesis, superfluid helium-4 was used to cool the crystals down to $\sim$ 2.1 K.

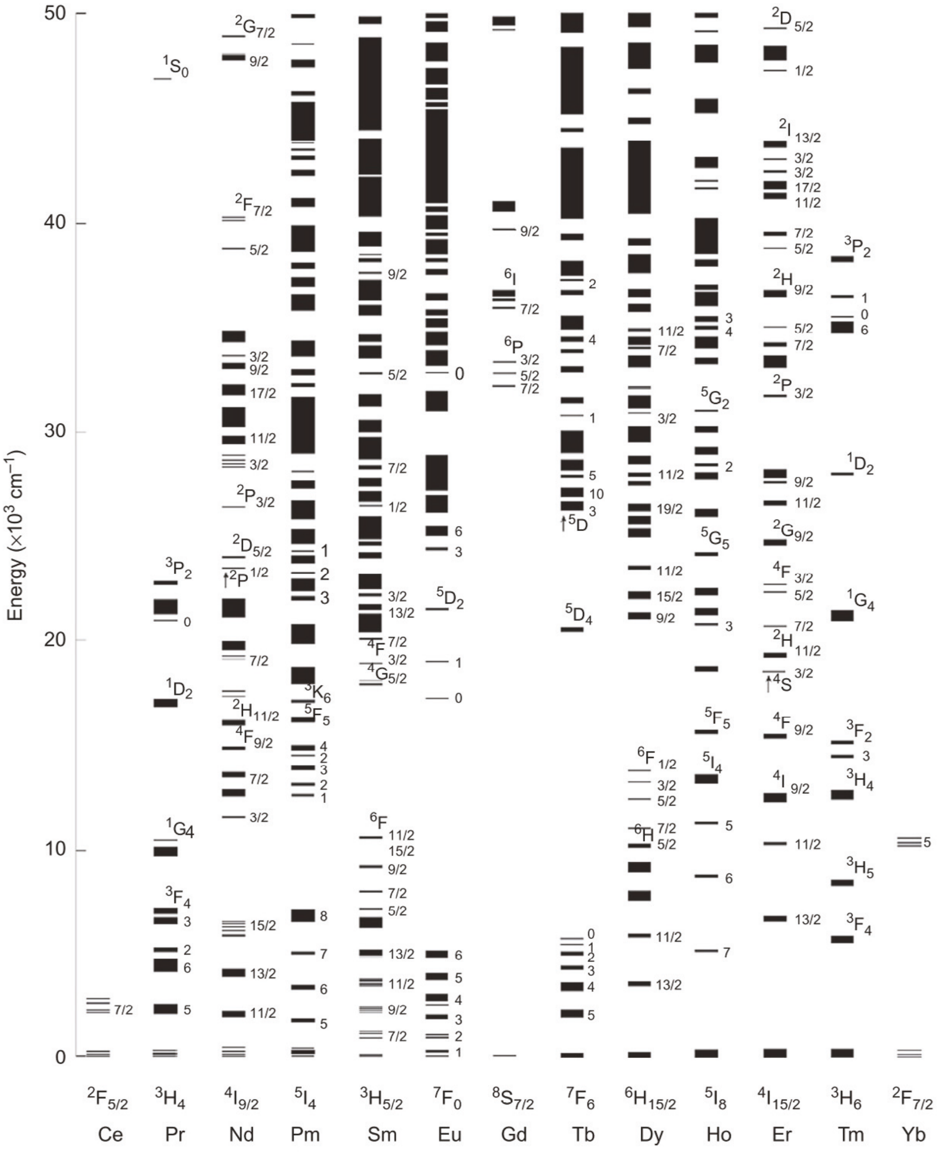

Figure 2.1: Dieke diagram for trivalent rare-earth ions in LaF_3, based on calculated free-ion and crystal field splittings. The overall structures shown here is similar in other hosts, because the crystal field splitting of the free ion levels is generally less than the free-ion level separation. Figure reprinted with permission from [17].

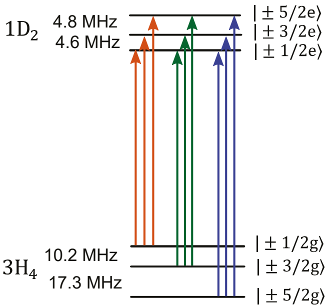

Figure 2.2. *Hyperfine energy level structure of the* $^3H_4 \rightarrow {}^1D_2$ *transition in* Pr^{3+}*:*Y_2SiO_5 *at site 1, with the nine possible transitions indicated by the arrows [21].*

2.1.2 Hyperfine structure

The hyperfine energy level structure in REI-doped crystals plays an important role in many quantum information processing applications, including some of the work presented in this thesis. For REIs that have a nuclear spin greater than 1/2, each of the crystal field levels splits into doubly degenerate hyperfine levels under zero magnetic field. Depending on the ion and on the host, the hyperfine frequency splitting is in the range of a few MHz to a few GHz. The hyperfine levels of the ground state can have exceptionally long lifetime at cryogenic temperatures. For example, a lifetime of 20 days have been reported in $\mathrm{Eu^{3+}{:}Y_2SiO_5}$ [18]. The coherence lifetime of these states can also be rather long, which is why they are used as qubit states in quantum computing applications [9], and for long-duration storage of quantum states [19, 20].

g\e	$\pm\|1/2e\rangle$	$\pm\|3/2e\rangle$	$\pm\|5/2e\rangle$
$\pm\|1/2g\rangle$	0.56	0.38	0.06
$\pm\|3/2g\rangle$	0.39	0.60	0.01
$\pm\|5/2g\rangle$	0.05	0.02	0.93

Table 2.1: Relative oscillator strength for the nine possible transitions of $\mathrm{Pr^{3+}{:}Y_2SiO_5}$ [21].

Since $\mathrm{Pr^{3+}{:}Y_2SiO_5}$ has been used $\mathrm{Pr^{3+}{:}Y_2SiO_5}$ in the quantum memory experiments presented in Chapter 7, its hyperfine structure will be highlighted. The only naturally abundant isotope (^{141}Pr) has a nuclear spin of 5/2, which means that both the $^3\mathrm{H}_4$ ground state and the $^1\mathrm{D}_2$ excited state in $\mathrm{Pr^{3+}{:}Y_2SiO_5}$ split into three hyperfine levels $|\pm1/2\rangle$,$|\pm3/2\rangle$,$|\pm5/2\rangle$, as shown in Figure 2.2. Each of the hyperfine levels in the ground state couples to the three hyperfine levels of the excited state, giving rise to nine possible transitions. The coupling between different levels is quantified by the relative oscillator strength of the relevant transition, as shown in Table 2.1. Due to the inhomogeneous broadening of the $^3\mathrm{H}_4 \rightarrow {}^1\mathrm{D}_2$ transition, each driving field with a certain frequency will thus be resonant with the nine transitions for nine different groups of ions at the same time.

2.1.3 Kramers ions

Kramers REIs are trivalent ions with an odd number of 4f electrons, and consequently have a half-integer total angular momentum J. For Kramers ions, the crystal field splits each of the $^{2S+1}L_J$ states into $j+1/2$ doubly degenerate levels, called Kramers doublets, which can be further split into two single levels by applying an external magnetic field. In general, only the lowest energy doublet has a long population lifetime at cryogenic temperatures, while the other doublets are short-lived due to the phonon coupling which causes a rapid relaxation to the lowest energy doublet. This means that the coupling between a ground and an excited state in a Kramers ion is usually between the lowest energy doublet in the two states. The typical level structure of a Kramers ion is shown in Figure 2.3

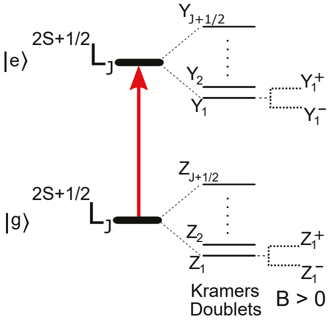

Figure 2.3. *Level structure of a Kramers ion showing the doublets of the ground (excited) state, denoted* Z_1, Z_2, $\cdots$ $Z_{J+1/2}$ (Y_1, Y_2, $\cdots$ $Y_{J+1/2}$).

2.1.4 Homogeneous lines and Inhomogeneous broadening

There are two key classes of broadening mechanisms that affect the observed optical lines in REIs. One mechanism is experienced equally by all ions regardless of its location in the crystal, and is called homogeneous broadening. In the other mechanism, called inhomogeneous broadening, local variations in the crystal affect different ions differently.

Homogeneous broadening

For a free isolated ion, the homogeneous linewidth of a certain transition is given by:

$$\gamma_0 = \frac{1}{2\pi T_1} \tag{2.1}$$

and is thus only limited by the lifetime T_1 of the excited state. This broadening is originally due to the Heisenberg time/energy uncertainty principle. When the ions are in a crystal, they will be exposed to several dynamic processes that will affect the same transition of all ions in the same way, causing the homogeneous linewidth to broaden. One such broadening process is thermal broadening caused by the coupling of crystal lattice phonons to the transition. These phonons, and consequently its contribution to the homogeneous broadening, can be significantly reduced by cooling the crystal to temperatures under 4 K, t.

Another mechanism that contributes to homogeneous broadening is fluctuations in the nuclear spin of the host, which can be reduced by choosing a host with low nuclear magnetic moment such as Y_2SiO_5 or Y_2O_3 . Similarly, fluctuation in the electronic spins is another contributor. This can be reduced, for example by applying suitable magnetic fields, to either cause Zeeman splitting that in turn affects the spin dynamics, or to 'freeze out' electronic spin fluctuations. Furthermore, when an ion is optically excited from the ground state, the electric field environment surrounding it will be perturbed due to the difference between the permanent electric dipole moment of the ground and the excited state. The optical transitions of nearby ions can be affected by this dynamic perturbation, depending on the spatial separation between the ions. This homogeneous broadening mechanism can be reduced by either reducing the doping concentration such that the ions are, on average, too far apart to affect each other, or by using low intensities for optical excitation.

As a consequence of the above broadening mechanisms, the homogeneous linewidth of the transition will not only be limited by the lifetime of the excited state. It will additionally be limited by the pure dephasing time ($T_2^\star$), which describes how long a superposition state between the excited and the ground state can last before it loses it phase information, or dephases. The homogeneous broadening due to the dephasing processes is given by Equation 2.2.

$$\gamma^\star = \frac{1}{\pi T_2^\star} \tag{2.2}$$

By ombining the homogeneous broadening effects given in Equations 2.1 and 2.2, the overall homogeneous broadening γ can be written as:

$$\gamma = \gamma_0 + \gamma^\star = \frac{1}{\pi T_2} = \frac{1}{2\pi T_1} + \frac{1}{\pi T_2^\star} \tag{2.3}$$

where $\frac{1}{T_2} = \frac{1}{2T_1} + \frac{1}{T_2^\star}$ is called the coherence lifetime, and describes the total dephasing time due to the lifetime limit and the dephasing processes. The maximum coherence time that can be obtained is $2T_1$ when all the dephasing mechanisms have been eliminated. Long coherence times are very desirable for quantum information application, as will be explained in more detail in the next section. This is also one of the main features of REIs which makes them appealing as a platform for quantum information applications.

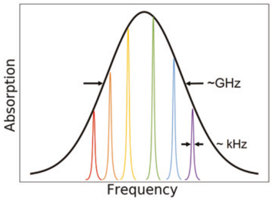

Figure 2.4. *A graphical illustration of the inhomogeneous line broadening. Different ions will have different resonance frequencies depending on their local environment, indicated by the narrow peaks with different colors. The overall absorption structure formed by the different ions gives rise to the inhomogeneous line.*

Inhomogeneous broadening

Inhomogeneous broadening is caused by effects that perturb different ions differently. For REI in a crystals, such local effects are caused by imperfect crystal growth, impurities, or simply the size difference between the dopant REI and the host ion it replaces. This creates local static strains in the crystal such that different REIs are surrounded by slightly different electric environments. As a result, the central frequencies of the optical transitions of the doping ions are shifted by different amounts depending on the local environment, giving rise to an inhomogeneous absorption line (Γ_{inh}) with a linewidth much broader than the homogeneous linewidth (Γ_h) as shown in Figure 2.4 [22, 23]. The inhomogeneous linewidth is on the order of GHz for REIs. Increasing the concentration of the REIs leads to further broadening of the homogeneous line [18].

The combined feature of broad inhomogeneous lines and narrow homogeneous lines could also be utilized for quantum information application, providing a large number of frequency channels

$\frac{\Gamma_{inh}}{\Gamma_h}$ that can be addressed independently and easily by tuning the frequency of the light source.

2.2 Potential for Quantum computing application

The multiple features of the REIs presented in the previous section make it an attractive system for quantum computation. These features include the long optical and spin coherence times, the combination of narrow homogeneous linewidths and wide inhomogeneous linewidths which gives rise to a large number of spectrally addressable frequency channels (qubits), and the electric dipole-dipole interactions that can be used to perform quantum operations. DiVincenzo's criteria summarise the requirements of a quantum computer based on a given system [10]. The main requirements for an REI-based quantum computer are summarized below.

Individually addressable and controllable qubits

Two of the ground hyperfine levels of an REI can be used as qubit states when cooled down to < 4 K. These states can be addressed and controlled through optical transitions to an excited state. Due to the inhomogeneous broadening discussed in 2.1.4, different qubit ions can have distinct resonance frequencies, making it possible to address different qubit ions spectrally.

Interacting qubits (quantum gates)

When used to dope solids, REIs can have permanent electric dipole moments in their ground and excited states. This means that ions can interact with each other through an electric dipole-dipole coupling. For example, when an ion is driven to an excited state, the resonance frequency of the neighboring ions can be detuned as a result of the dipole-dipole interaction. The amount of this detuning depends on the differences in the dipole moments between the ground and the excited state, and on the spatial separation between the ions. This interaction can be used to enable fast interactions between qubits.

Long coherence times

The coherence time of the qubit should be much longer than the time it taken to perform a quantum gate operation, so that a large number of operations can be performed before the qubit loses its coherence. At liquid helium temperatures, the coherence time of the ground hyperfine levels of REIs can reach seconds, with the longest reported being hours in Eu^{3+}:Y_2SiO_5 under certain conditions [8], while the lifetime can be days [18]. The typical duration of the optical π pulse used to drive the qubit ion between the hyperfine states and the excited state is on the order of hundreds of nanoseconds. This allows for a large number of operations within the coherence time of the qubit.

Qubit readout

Reliable measurement of the final state of the qubit after the operations is imperative. Direct optical detection of a single ion in REI systems is challenging due to the exceptionally long lifetimes of the excited states, and consequently, the low spontaneous emission rates. This problem was addressed in this work, and will be covered in more detail in Chapters 4 and 5. It should be noted that an alternative scheme that uses an ensemble of REIs to represent one qubit has been demonstrated [9]. When the qubit is represented by an ensemble of ions, it is difficult to achieve a large number of qubits that can strongly interact with each other since the ions composing the qubits are randomly distributed within the crystal. While this ensemble based scheme works for conceptual demonstrations, it is not scalable.

Scalability

A large number of qubits will be required to build a useful quantum computer. Scalability means that the resources required to operate such a quantum computer must not scale exponentially with the number of qubits. The ability to detect single REIs is a crucial requirement to enable scalability in REI-based quantum computing.

Chapter 3

Cavity-Enhanced Light-Matter Interactions

Part of the work presented in this thesis is based on using optical microcavities to enhance light interaction with the weak transitions of the REIs, and thus improve their functionalities for quantum information applications. The aim of this chapter is to give a basic theoretical description of the enhanced light-matter interactions in optical cavities. The different coupling regimes are discussed, with a focus on the Purcell enhancement. An overview of several microcavity platforms is presented, and the fiber-based microcavity, which is used in this work, is highlighted. The most important parameters associated with fiber-based microcavities are presented.

3.1 Why do we need cavities?

In order to understand the benefit of using optical cavities in the context of light-matter interactions, it is useful to first consider these interactions in free space. Consider the case of a freely propagating optical mode focused to a beam waist of ω_0 and interacting with a two-level dipolar emitter. The probability of this interaction taking place depends on how well the light mode is overlapped by the dipolar emitter. This can be expressed more quantitatively by introducing the absorption cross-section, σ_{abs}, of the dipolar emitter, which describes the probability of absorption of an incoming light mode with a wavelength λ. The absorption cross-section can be thought of as the effective area over which that atom can affect the incoming light wave, which is different from the geometrical area of the atom. For a two-level system (TLS), the maximum absorption cross section at resonance is defined as [24]:

$$\sigma_{abs} = \frac{3\lambda^2}{2\pi} \tag{3.1}$$

In general, in order for a significant part of a beam mode to interact with the atoms, the area of the focused beam (A $= \pi\omega_0^2/4$, where ω_0 is the beam waist) must be comparable to the absorption cross section given by Equation 3.1 [25]. Assuming that the incoming light beam has a power P_{in}, the ratio of the scattered light by the atom (P_{sc}) to the incoming beam is given by:

$$\text{Scattering Ratio} = \frac{P_{sc}}{P_{in}} = \frac{\sigma_0}{A} \tag{3.2}$$

The absorption cross section for the 892 nm $^4\mathrm{F}_{3/2} - {}^4\mathrm{I}_{9/2}$ transition of a free Nd^{3+} ion is 0.38 $\mu\mathrm{m}^2$. Using Equation 3.2, the scattering ratio for an incoming Gaussian beam focused to a 100 μm waist size on the Nd^{3+} ion is $\sim 7.8 \times 10^{-5}$, which is extremely small. The intuitive way to increase the interaction probability in free space is by decreasing the beam area. However, the beam size cannot be decreased indefinitely in free space as it will eventually be restricted by the diffraction limit. Furthermore, when tightly focused, only part of the focused beam will have a polarization allowing to interact with the dipolar emitter, which further reduces the scattering ratio. The limitations of free-space light-atom interactions is discussed in detail elsewhere [26–28]. The restrictions above make it challenging to realize light-matter interaction at the single-atom level in free space, and consequently limit applications in quantum information that are based on efficient coupling between light and atoms. This is a reason why optical optical cavities are required.

An optical cavity is a device that traps photons within a well-defined volume for a certain period of time. Photons can be confined in several ways, corresponding to different cavity platforms. A simple optical cavity can be formed by two mirrors, with reflectivities R_1 and R_2, that reflect light such that it circulates in a closed loop confined in space, and eventually forms a standing wave. The number of times the light 'bounces' between the two mirrors is quantified by cavity *finesse*, $\mathcal{F}$, which describes the quality of the cavity. The cavity finesse can be written in terms of the reflectivities of the mirrors as:

$$\mathcal{F} = \frac{\pi(R_1R_2)^{\frac{1}{4}}}{1-\sqrt{R_1R_2}} \tag{3.3}$$

If the atom is placed in such a cavity instead of free space, the scattering ratio given by Equation 3.2 increases by a factor of $\mathcal{F}/\pi$ [25]. This means that the probability of an interaction taking place between the circulating light and the atom becomes more likely. The strength of the interaction depends on the properties of the cavity and properties of the atom and the coupling between the two. The next section describes these interactions more quantitatively.

3.2 Light-matter interactions in a cavity

Let us consider a simple two level atom with a resonant angular frequency ω_a interacting with light with an angular frequency ω_c inside an optical cavity. The dynamics of such a system are described by the Jaynes-Cummings (JC) model, which relies on quantum treatment of the two-level system and the quantized light field.

The complete Hamiltonian of the cavity-atom system is given by the JC Hamiltonian, which can be written:

$$\hat{H} = \hat{H}_a + \hat{H}_c + \hat{H}_{a.c}, \tag{3.4}$$

where:
$\hat{H}_a = \hbar\omega_{eg}\frac{\hat{\sigma}_z}{2}$ is the atom Hamiltonian, with $\hbar\omega_{eg}$ representing the energy difference between the ground and the excited states of the TLS, $\hbar$ is the reduced Planck constant, $\sigma_z =$ is the Pauli z matrix.
$\hat{H}_c = \hbar\omega_c\hat{a}^\dagger\hat{a}$ is the Hamiltonian for a single-cavity mode field, where $\hat{a}^\dagger$ and $\hat{a}$ are the annihilation and creation operators[1] of a photon in the cavity, respectively.
$\hat{H}_{a.c} = \hat{\boldsymbol{\mu}} \cdot \hat{\mathbf{E}}_c$ is the Hamiltonian describing the coupling between the atom and the cavity mode. Here, $\hat{\mu}$ is the atomic dipole moment operator, which can be expressed in terms of the transition dipole moment $\boldsymbol{\mu}_{\mathbf{ge}}$ and the atomic raising $\hat{\sigma}^+$ and lowering $\hat{\sigma}^-$ operators[2], such that $\hat{\boldsymbol{\mu}} = \boldsymbol{\mu}_{\mathbf{ge}}(\hat{\sigma}^+ + \hat{\sigma}^-)$. $\hat{\mathbf{E}}_c$ is the quantized electric field operator, which can be written as $\hat{\mathbf{E}}_c = \sqrt{\frac{\hbar\omega_c}{2\epsilon_0 V}}\boldsymbol{\epsilon}(\hat{a}^\dagger + \hat{a})$, where ϵ_0 is the vacuum permittivity, $\boldsymbol{\epsilon}$ is the field polarization vector, and V is volume of the field mode in the cavity. From this, the atom-cavity interaction term can be rewritten as:

$$H_{a.c} = \boldsymbol{\mu}_{\mathbf{ge}}\sqrt{\frac{\hbar\omega_c}{2\epsilon_0 V}}\boldsymbol{\epsilon}(\hat{\sigma}^+ + \hat{\sigma}^-)(a^\dagger + a) \tag{3.5}$$

This Hamiltonian contains four terms. Two of them contain the operators $\hat{\sigma}^+\hat{a}$ and $\hat{\sigma}^-\hat{a}^\dagger$, which, when expressed in terms of time dependent operators, evolve at the optical frequency $\Delta = (\omega_{eg} - \omega_c)$. The other two terms contain the operators $\hat{\sigma}^+\hat{a}^\dagger$ and $\hat{\sigma}^-\hat{a}$, which evolve at an optical frequency of $(\omega_{eg} + \omega_c)$. When the atomic transition frequency ω_{eg} and the cavity mode frequency ω_c are close, the oscillation of the $\hat{\sigma}^+\hat{a}^\dagger$ and $\hat{\sigma}^-\hat{a}$ terms will be much greater than Δ. The processes associated with the fast oscillating terms in this case do not contribute to the resonant atom-cavity dynamics, and are thus omitted in what is called the rotating wave

---

[1] The annihilation operator $\hat{a}$ reduces the number of photons in the cavity by one, while the creation operator $\hat{a}^\dagger$ increases the number by one

[2] The lowering operator $\hat{\sigma}^-$ acts on the excited state, $|e\rangle$, and converts it to the ground state, $|g\rangle$, while the raising operator acts on the $|g\rangle$ state and convert to the $|e\rangle$ state

approximation. This can also be understood from energy conservation prospective as follows. The term $\hat{\sigma}^+\hat{a}^\dagger$ is associated with a process in which the atom is excited and a photon is added to the field, while the term $\hat{\sigma}^-\hat{a}$ is associated with an atomic transition from the excited state to the ground state, and a photon lost by the field. Neither of these processes is energy conserving, and both can thus can be ignored. On the other hand, the term $\hat{\sigma}^+\hat{a}$ is associated with a transition to the excited state and the absorption of a photon, while $\hat{\sigma}^-\hat{a}^\dagger$ corresponds to a transition to the ground state accompanied by the emission of a photon. Using this rotating wave approximation, the atom-cavity interaction term then becomes:

$$H_{a.c} = \boldsymbol{\mu}_{\mathbf{ge}} \sqrt{\frac{\hbar\omega_c}{2\epsilon_0 V}} \boldsymbol{\epsilon} (\hat{\sigma}^+\hat{a} + \hat{\sigma}^-\hat{a}^\dagger) \tag{3.6}$$

The strength of the atom-cavity coupling is proportional to the coupling between the atomic dipole and the field. This coupling strength constant is given by:

$$g = \frac{\boldsymbol{\mu}_{\mathbf{ge}}.\mathbf{E}}{\hbar} = \sqrt{\frac{\omega_c}{2\hbar\epsilon_0 V}} \mu_{\mathbf{ge}}.\epsilon \tag{3.7}$$

It should be noted that here $\boldsymbol{\mu}_{\mathbf{ge}}$ and $\mathbf{E}$ are vectors, not operators. The coupling constant g can be used to rewrite Equation 3.6 as follows:

$$H_{a.c} = \hbar g(\hat{\sigma}^+\hat{a} + \hat{\sigma}^-\hat{a}^\dagger) \tag{3.8}$$

The complete Jaynes-Cummings Hamiltonian can be rewritten in terms of the three different Hamiltonians discussed above:

$$\hat{H} = \hbar\omega_{eg}\frac{\hat{\sigma}_z}{2} + \hbar\omega_c\hat{a}^\dagger\hat{a} + \hbar g(\hat{\sigma}^+\hat{a} + \hat{\sigma}^-\hat{a}^\dagger) \tag{3.9}$$

When the coupling constant $g = 0$ the Hamiltonian reduces to only the first two terms with no interaction between the atom and the cavity field. This case is not of interest in the present discussion. Instead, we will focus on the case of cross interaction between the atom and the cavity mode. The strength of this interaction depends on three factors, as discussed below [29].

- The cavity photon decay rate ($\kappa = \frac{1}{\tau_c}$): where τ is the lifetime of a photon inside the cavity, i.e. the time at which the light has $1/e$ of its initial energy left in the cavity. This decay rate is completely dependent on the properties of the cavity. As the light oscillates inside the cavity, part of its energy will be lost in each oscillation cycle due to being partially transmitted through the mirror, or due to absorption and scattering within the cavity. The lower this energy loss, the lower is the decay rate of the cavity. The ratio of the total energy stored in the cavity to the energy lost per oscillation cycle is called the cavity quality factor Q. The quality factor is more commonly used to quantify the cavity decay rate, and the relation between the two is given by:

$$\kappa = \frac{1}{\tau_c} = \frac{\omega_c}{Q} \tag{3.10}$$

- The atomic dephasing rate (or homogeneous linewidth of the relevant transition) γ: which depends on both the excited state lifetime, T_1, and the dephasing lifetime, T_2, (see Section 2.1.4 for more details). Apart from coupling to the cavity mode, an excited atom could decay through several other channels, for example, non-radiative decay, or decay to other levels through transitions that are not resonant with the cavity. These alternative decay channels outside the cavity mode are considered as losses in the atom-cavity interaction picture, and are quantified by the homogeneous linewidth of the transition defined by Equation 2.3.
- The atom-cavity coupling rate, g, which quantifies the strength of the interaction between the atom and the cavity. As can be seen by Equation 3.7, it is dependent on the cavity resonant frequency, ω_c, the atomic dipole moment of the relevant transition, $\boldsymbol{\mu}_{\mathbf{ge}}$, and the cavity mode volume, V.

These three different rates are combined in a parameter called the atom-cavity cooperativity (C), which is written [25]:

$$C = \frac{g^2}{2\kappa\gamma} \tag{3.11}$$

The atom-cavity interaction can be categorized into two regimes depending on the above factors: the *strong coupling regime* and the *weak coupling regime (or Purcell regime)*. These two regimes are described in detail in the following sections.

3.2.1 Strong coupling regime

Strong coupling is achieved for $C \gg 1$ (or $g \gg \kappa, \gamma$). In this regime, an atom in the excited state will not spontaneously decay irreversibly to the ground state, as it would in free space. Instead, it will undergo a quantum oscillation, where the atom decays by emitting into the cavity mode, and is repeatedly excited by the same cavity mode. This is sometimes referred to as oscillatory spontaneous emission [30]. To understand the origin of these oscillations, we will consider an atom-cavity system with n photons in the cavity mode. As described by the Hamiltonian in Equation 3.9, the eigenenergies of this Hamiltonian can be written [30–32]:

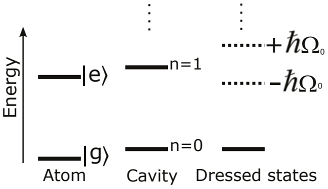

Figure 3.1.

$$E_{\pm n} = \hbar\omega_c(n + \frac{1}{2}) \pm \frac{\hbar}{2}\Omega, \tag{3.12}$$

where Ω is called the generalized Rabi frequency, given by:

$$\Omega = \sqrt{\Delta^2 + 4g^2(n+1)} \tag{3.13}$$

The corresponding eigenstates of the eigenenergies described by Equation 3.12 are called the dressed states, and are a characteristic of the strong coupling regime. To gain an intuitive understanding of these states, let us consider the case where in the initial state of the atom-cavity system, there is one atom in the excited state, and no photons in the cavity ($|e,0\rangle$). The time evolution of this system based on the Hamiltonian given above will consist of oscillations between two states: an excited atom with no photons in the cavity ($|e,0\rangle$), and an atom de-excited to the ground state and one photon emitted into the cavity mode ($|g,1\rangle$).

$$|e,0\rangle \rightarrow |g,1\rangle \rightarrow |e,0\rangle \rightarrow |g,1\rangle \dots \tag{3.14}$$

In other words, the strongly coupled atom-cavity system is made up of a superposition state of the two possible non-interacting terms of the atom and the cavity. The oscillation between these two states is called the vacuum Rabi oscillation, and the frequency of this oscillation is the Rabi frequency (Ω) defined by Equation 3.13, and in this case ($\Delta = \omega_{eg} - \omega_c = 0, n = 0$) $\Omega_0 = 2g$. Consequently, the energy splitting between these two states is $\hbar\Omega_0$. The energy manifold of the atom, cavity and the Rabi splitting of the dressed states is shown in Figure 3.1 The corresponding dressed state of this system is given by [30]:

$$|\pm,0\rangle = \frac{1}{\sqrt{2}}[|e,0\rangle \pm i\,|g,1\rangle \tag{3.15}$$

The probability of finding the atom in the excited state at a given time is given by [30]:

$$P_e(t) = cos^2(\frac{\Omega_0 t}{2}) = cos^2(gt) \tag{3.16}$$

which, as motioned above, describes an oscillation at Rabi frequency, Ω_0. This can be generalized to any atom-cavity state with a higher number of photons n in the cavity mode, with an exception for the ground state $|g,0\rangle$, i.e. the atom in the ground state and no photons in the cavity. This state does not split into dressed states, and is not affected by the atom-cavity coupling.

In the discussion above, an ideal atom-cavity system that is not affected by the surrounding environment was assumed. The effects of the environment are captured by the cavity decay rate, κ, and the atomic decay rate, γ. When taking these effects into account, the atom-cavity dynamics is described by the Lindblad master equation, a detailed description of which can be found elsewhere [30]. In practice, the effect of these losses would be that the Rabi oscillations discussed above will decay over time. In other words, the probability of finding the atom in the excited state given by Equation 3.16 will decrease exponentially.

The first demonstration of the strong coupling regime using an optical cavity was achieved with cesium atoms [33], where it was experimentally shown that the coupling strength is proportional to $\sqrt{N}$, where N is the number of atoms. This was followed by several experimental demonstrations using different atom/cavity systems.

In the case of crystals doped with REIs, the electric dipole moment of the relevant $4f-4f$ transitions is generally weak. Since the coupling constant, g, is directly proportional to the dipole moment (Equation 3.7), the $g \gg \kappa$ condition becomes practically out of reach, and consequently the strong coupling regime cannot be achieved for the $4f-4f$ transitions of REIs. Nevertheless, there are some REIs, such as Ce^{3+} , with a strong $4f-5d$ transition that could possibly reach the strong coupling regime. These transitions are often in the ultraviolet (UV) range, which is a difficult wavelength to operate the cavities at due to the high scattering losses by the cavity mirrors and the samples.

3.2.2 Weak coupling regime

The weak coupling regime, also referred to as the Purcell regime, is achieved when $C > 1$ $(\kappa \gg g \gg \gamma)$. In this regime, the cavity decay rate is higher than the atom-cavity coupling rate, which means that a photon emitted by an excited atom would escape the cavity before it can be re-absorbed by the atom, and hence spontaneous emission is irreversible here. The characteristic of this regime is that the spontaneous emission rate of the atom is higher in the cavity that for an atom in free space. This enhancement of spontaneous emission is also referred to as the Purcell effect. The magnitude of this enhancement is obtained by comparing the transition decay rate of an atom "weakly" coupled to a cavity to that of an atom in free space. This effect was first predicted by Purcell for a system of nuclear magnet moment at radio frequency coupled to a resonant electrical circuit [34]. The first experimental observation of the enhancement of atomic spontaneous emission was by Haroche, in an experiment performed with Rydberg atoms of sodium coupled to a superconducting cavity [35].

We will now consider a TLS with a ground state $|g\rangle$ and an excited state $|e\rangle$. Assuming that it is initially in the excited state, the probability of finding the system in the excited state can be written:

$$P_e(t) = e^{-\Gamma t} \tag{3.17}$$

Here, Γ is the decay rate from $|e\rangle$ to $|g\rangle$. This decay rate can be described by Fermi's golden rule, which is given by [29]:

$$\Gamma = 2\pi\,\rho(\omega)\,g^2 = \frac{2\pi}{\hbar^2}\,\rho(\omega)\,\left|\langle \boldsymbol{\mu}_{ge}.\mathbf{E}_v\rangle\right|^2\,, \tag{3.18}$$

where $\rho(\omega)$ is the spectral density of states (DOS). Note that the definition of the coupling constant g given by Equation 3.7 for a TLS coupled to a cavity was used in the equation above.

Fermi's golden rule states that the decay rate depends on the coupling strength between the ground state $|g\rangle$ and the excited state $|e\rangle$, which is represented by $\langle \boldsymbol{\mu}_{ge}.\mathbf{E}_v\rangle$, the transition matrix element of the interaction Hamiltonian between the two states. Here we consider the case with no external electric field, which means that $\mathbf{E_v}$ will be the vacuum field, with a magnitude given by $E_v = \sqrt{\frac{\hbar\omega}{2\epsilon_0 V}}$. Using Equation 3.7, the coupling contribution can be written:

$$g^2 = \xi^2\frac{\omega\mu_{eg}^2}{2\hbar\epsilon_0 V}, \tag{3.19}$$

where the factor ξ denotes the normalized dipole orientation with respect to the vacuum field polarization. In free space, $\xi^2 = \frac{1}{3}$, which results from averaging over all possible orientation of the dipole moment with respect to the field polarization. V is the volume of the vacuum field mode.

Furthermore, based on Fermi's golden rule, the transition decay rate in Equation 3.18 also depends on the DOS, $\rho(\omega)$, which refers to the number of states that the system can decay to per unit energy per unit volume. The DOS depends on the surrounding environment, which implies that the spontaneous emission rate is not an intrinsic property of the TLS (or the emitter in general) only, but is alsoadditionally affected by the surrounding environment. The enhancement of the spontaneous emission rate when the TLS is placed inside a cavity within the weak coupling regime would effectively be the ratio of the DOS in the cavity to the DOS in free space.

The DOS in free space is given by:

$$\rho(\omega) = \frac{\omega^2 V}{\pi^2 c^3} \tag{3.20}$$

A detailed derivation of this can be found in Appendix C in Ref. [29]. Substituting for the coupling strength, Equation 3.19, and the spectral mode density in free space, Equation 3.20, in Equation 3.18, the spontaneous emission rate in free space (Γ_f) can be written:

$$\Gamma_f = \frac{1}{3}\,\frac{\mu_{eg}^2\omega^3}{\pi\hbar\epsilon_0 c^3} \tag{3.21}$$

The radiative lifetime of the transition is then defined as the inverse of this decay rate, i.e. $T_1 = \frac{1}{\Gamma_f}$.

We will now calculate the DOS of the cavity. Consider a TLS with resonant angular frequency ω_a inside a cavity with a resonant angular frequency ω_c and a decay rate κ. The DOS in the cavity takes a Lorentzian form with a linewidth given by the cavity decay rate κ:

$$\rho(\omega) = \frac{1}{\pi} \frac{\frac{\kappa}{2}}{(\frac{\kappa}{2})^2 + (\omega_c - \omega)^2} \tag{3.22}$$

In the special case of a resonant system, where the angular frequency of the TLS is the same as the resonance of the cavity ($\omega_a = \omega_c$), the DOS can be written:

$$\rho(\omega_c) = \frac{2}{\pi\kappa} = \frac{2Q}{\pi\omega_c}, \tag{3.23}$$

where Equation 3.10 was used to write κ in terms of the cavity quality factor, Q, and cavity resonance, ω_c, which is the same as the cavity resonance here. It is useful to rewrite the DOS given by Equation 3.22 for the general case ($\omega_c \neq \omega_a$) in terms of Q, such that:

$$\rho(\omega_a) = \frac{2Q}{\pi\omega_c} \frac{(\frac{\kappa}{2})^2}{(\frac{\kappa}{2})^2 + (\omega_c - \omega_a)^2} \tag{3.24}$$

Knowing the density of state for a cavity with a mode volume V, and using the coupling contribution given by Equation 3.19, the spontaneous emission rate in the cavity (Γ_c) can be obtained using Fermi's golden rule (Equation 3.18), which gives:

$$\Gamma_c = \xi^2 \frac{2Q\mu_{eg}^2}{\hbar\epsilon_0 V} \frac{(\frac{\kappa}{2})^2}{(\frac{\kappa}{2})^2 + (\omega_c - \omega_a)^2} \tag{3.25}$$

In the resonant case ($\omega_c = \omega$), this expression reduces to:

$$\Gamma_c = \xi^2 \frac{2Q\mu_{eg}^2}{\hbar\epsilon_0 V} \tag{3.26}$$

It should be noted here that even when coupled to a cavity, dipolar emitters can radiate photons into free space from the open sides of the cavity. This emission rate depends on the solid angle, $\Delta\Omega$, spanned by the cavity mirror at the emitter position. For a dipolar emitter polarized at right angles with respect to the cavity axis, the emission rate out of the cavity sides (Γ_{cf}) can be written [36]:

$$\Gamma_{cf} = \Gamma_f \left(1 - \frac{3\Delta\Omega}{8\pi}\right) \tag{3.27}$$

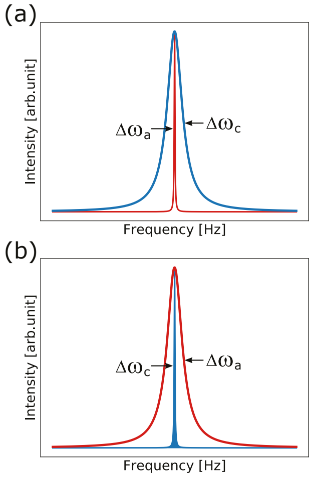

Figure 3.2. *(a) A narrow atomic transition in resonance with a wider cavity resonance ($\omega_c \gg \omega_a$). In this case the spontaneous emission of the whole atomic transition will be enhanced, the magnitude depending on Q and V as stated in Equation 3.29. (b) A case where the atomic transition is wider than the cavity linewidth, and only the blue shaded part of the atomic transition will be affected by the cavity enhancement, which in this case depends on the transition quality factor, Q_a, given by Equation 3.30*

which holds for $\Delta\Omega \ll 4\pi$. For cavities with $Q\lambda^3/V \gg 4\pi$, the enhanced emission into the cavity mode dominates the fraction emitted into free space. The emission into free space is thus not considered in the following discussions.

A key figure of merit in the weak coupling regime is the *Purcell factor (P)*, which describes the effect of the cavity on the spontaneous emission rate of a TLS. The Purcell factor is written:

$$P = \frac{\Gamma_c}{\Gamma_f} = \frac{3\xi^2 Q \frac{\lambda^3}{n}}{4\pi^2 V} \frac{(\frac{\kappa}{2})^2}{(\frac{\kappa}{2})^2 + (\omega_c - \omega_a)^2} \tag{3.28}$$

Note that the angular frequency has been replaced by $\frac{2\pi c}{\lambda/n}$, where λ is the wavelength of the light in vacuum, and n is the refractive index inside the cavity. In the resonant case, and assuming that the electric dipole of the TLS is perfectly overlapped by the cavity mode ($\xi = 1$) the Purcell factor simplifies to:

$$P = \frac{3}{4\pi^2} \frac{Q}{V} \left(\frac{\lambda}{n}\right)^3, \tag{3.29}$$

For the discussion above, it was assumed that the cavity decay rate, κ, was faster than the atomic dephasing rate γ. In terms of linewidths, this corresponds to a transition linewidth of $\Delta\omega_a$, which is much narrower than the cavity resonance linewidth, $\Delta\omega_c$, as shown in Figure 3.2 (a). This is generally the case when coupling REIs in crystals to a cavity at cryogenic temperatures as will be discussed in Chapter 5. In this case, the Purcell factor depends on the cavity quality factor, Q, and on the cavity mode volume, V. If, on the other hand, the cavity linewidth is narrower than the transition linewidth of the TLS, only the part of the transition linewidth that is spectrally overlapped by the cavity linewidth will be affected by the cavity enhancement, as shown in Figure 3.2 (b). This means that the Purcell factor will be effectively reduced by approximately a factor of $\frac{\Delta\omega_a}{\Delta\omega_c}$. In this case, the cavity quality factor in Equation 3.29 is replaced by the TLS quality factor, Q_a, which is given by:

$$Q_a = \frac{\omega_a}{\Delta\omega_a}, \tag{3.30}$$

where ω_0 is the transition frequency. At room temperature, the $4f - 4f$ transitions of REIs have wide homogeneous linewidths due to the coupling with thermal phonons, which is the dominant dephasing channel. When coupling REIs to high Q-cavity at room temperature, the second case discussed above would be more likely.

So far we have discussed a simple TLS with $|g\rangle$ and $|e\rangle$ states, which is helpful in understanding the dynamics. However, a real atom has a much more complex level structures, and when it is excited to an upper level, it may decay to several ground levels with different probabilities. The probability of decaying to a specific ground level is expressed by a factor called the branching ratio B. The Purcell factor for an atomic transition coupled to a cavity will be further reduced by the branching ratio for that transition.

The weak coupling regime is relevant for the work presented in this thesis using REIs. Although the $4f-4f$ transitions are generally weak, with relatively low electric dipole moments, their decay rate can still be affected by a cavity with suitable values of the quality factor and cavity mode volume. A high Q and a small V are the important requirements to obtain a strong Purcell effect.

3.3 Microcavity platforms for REIs

The need for small cavity mode volumes and high quality factors triggered the development of different microcavity platforms [37]. Several of these platforms have been adopted within the REIs community over the last few years to overcome the low spontaneous emission rate of the weak $4f-4f$ transitions through the Purcell effect. The group of Professor Faraon at the California Institute of Technology (Caltech, PA, USA) uses nanophotonics cavities fabricated directly on the REIs doped crystal by focused-ion-beam [38–40]. A nanophotonic cavity is generally formed by machining a periodic lattice structure of holes in a slab of material. By introducing defects on the lattice structure, usually some intentionally missing holes, the Bragg reflection condition can be achieved for a certain wavelength, and light with that wavelength will thus be confined within the lattice structure. This approach allows for very small mode volume ($V < \lambda^3$), where λ is the wavelength of the circulating light. Quality factors on the order of 10^3-10^4 have been demonstrated using those systems in the near-infrared range [39, 40]. A similar approach based on nanophotonic cavities has been adopted by Professor Thompson's group at Princeton University (NJ, USA). In this approach, the nanophotonic structure is formed by an array of holes machined on a silicon waveguide, which is then bonded on top of a polished REI doped crystal [41–43]. REIs close the crystal surface couple to the nanophotonic cavity mode through the evanescent electric field. The cavity mode volume and quality factor obtained using this approach are similar to those mentioned above. Both of these schemes work best when coupled to transitions in the near-infrared range, but the performance is degraded in the visible range due to the large scattering losses, which reduces the cavity Q.

Another approach, which has been adopted by Professor Wrachtrup's group in Stuttgart university (Stuttgart, Germany) is based on whispering-gallery mode (WGM) microcavities [44–46]. This kind of cavities is based on the total internal reflection of light circulating within a microdisc. The microdiscs are fabricated from a thin film of lithium niobate doped with a REI. Quality factors on the order of $10^4 - 10^5$ and a mode volume of $\sim 50\lambda^3$ have been reported at 980 nm using this approach [47].

The cavity used for the work described in this thesis and adopted by the quantum information group at Lund university, is based on an open-access FBFP microcavity. This scheme has also been adopted by the group of Professor Hunger at Karlsruhe Institute of Technology (KIT, Karlsruhe, Germany), and by Professor Riedmatten's group at the Institute of Photonic Sciences (ICFO, Barcelona, Spain). A Fabry-Perot cavity is formed of two reflective mirrors between which the light can circulate. In the FBFP microcavity used in the present work, one of the mirrors is machined on the end-facet of an optical fiber, which allows for very small mode volume $\sim \lambda^3$ [48–50]. A similar Fabry-Perot cavity approach has also been adopted by Professor Reiserer's group at the Max Planck Institute of Quantum Optics (Garching, Germany) [51]. In their case, the cavity is formed of two macroscopic mirrors separated by tens of micrometers, with a thin film of REIs doped crystal embedded in between.

A more detailed discussion of different microcavity platforms employing REIs can be found in the review by Kinos *et al.* [52].

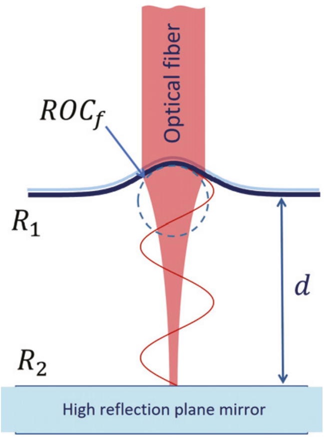

Figure 3.3. *Schematic showing a FBFP cavity with cavity length d, Fiber mirror reflectivity R_1, plane mirror reflectivity R_2, fiber mirro radius of curvature ROC_f.*

3.4 Fiber-Based Fabry-Perot cavity

In this section, the most important parameters associated with the Fabry-Perot cavity will be discussed, focusing on the parameters relevant for the FBFP microcavities used in this work.

Consider a FBFP microcavity with mirror reflectivities R_1 and R_2 and a cavity length d, with a light wave with a wavevector $k = \frac{2\pi}{\lambda}$, where λ is the wavelength of the light. The resonance condition is achieved when the light wave reproduces itself after one round trip in the cavity, i.e. after travelling a distance $2d$. The resonant light wave is called a cavity mode. For wave reproduction to occur the phase shift, ϕ , must be $q2\pi$ after a round trip, where q is a positive integer referred to as the mode number. The phase shift can also be expressed as $\phi = k2d$, and thus the resonance condition can be expressed:

$$\lambda_q = \frac{2d}{q} \qquad \nu_q = q\frac{c}{2d}, \tag{3.31}$$

where $\nu = c/\lambda$ is used to express the resonance condition in the frequency domain. From the wavelength expression, it can be seen that at resonance, the cavity length must be an integer number of half wavelengths.

3.4.1 Free spectral range

The free spectral range (FSR) of the cavity is defined as the separation between two neighbouring resonant modes. This can be written as:

$$FSR_\nu = \nu_{q+1} - \nu_q = \frac{c}{2d}, \tag{3.32}$$

The FSR of a cavity is determined by the cavity length. For FBFP microcavities, the cavity length is generally on the order of a few μm, which corresponds to an FSR in the order of a few tens on THz. The FSR can also be defined in terms of the wavelength of the light traveling through the cavity. Here, a fixed cavity length is assumed, and the FSR is defined as the difference in wavelength difference between two successively resonant wavelengths:

$$FSR_\lambda = \frac{\lambda_q^2}{2d}, \tag{3.33}$$

For a monochromatic cavity input, the FSR can also be expressed in terms of physical distance using the resonance condition $d = q\lambda/2$, which gives:

$$FSR_d = \frac{\lambda}{2} \tag{3.34}$$

which means that a new resonance fits into the cavity for every $\lambda/2$ increase in the cavity length.

There are three ways to measure the cavity FSR:

- Using a light source with a narrow linewidth as the cavity input, and scanning the light wavelength across two successive cavity resonances. This measures FSR_ν and FSR_λ.
- Using a broadband light source as the cavity input. Most of the light will be filtered out, and only resonant modes will be transmitted through the cavity. The FSR can be measured between two neighboring modes. This also measures FSR_ν and FSR_λ.
- Using a single wavelength light source as the cavity input, and scanning the cavity length across multiple resonances. This method will measure FSR_d.

Due to the large FSR in FBFP microcavities, the first method is difficult to used as it requires a narrow linewidth laser with a scan range of tens of THz. Therefore, the second and third methods were used in this work. Furthermore, the cavity length is usually also determined using the second method as well. The cavity length scan range is calibrated using the third method since the absolute displacement between the resonances is known, $\lambda/2$

3.4.2 Finesse and linewidth

So far, it has been assumed that the light reflects back and forth an infinite number of times within the cavity, and the implication

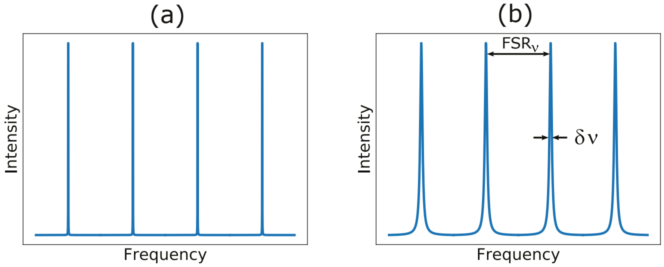

Figure 3.4: (a) The modes of an ideal cavity without any losses. (b) The modes of a realistic cavity. Here the modes have a Lorentzian shape with a defined linewidth $\delta\nu$. FSR_ν is the free spectral range defined by Equation 3.32.

of this is that the cavity resonances are described by infinitely sharp peaks defined by different mode numbers as shown in Figure 3.4 (a). In reality, some of the light may leak out of the cavity as it oscillates, and the cavity modes would thus have a non-zero linewidth $\delta\nu$ that depends solely on the cavity losses. These losses may be due to transmission through the cavity mirrors, or absorption and scattering in the medium inside the cavity or the mirrors. A realistic cavity transmission is shown in Figure 3.4 (b). The cavity linewidth was defined in Equation 3.10, in terms of the angular frequency, as the decay rate of light in the cavity. This decay is generally very fast and not trivial to measure. Alternatively, the cavity linewidth can be written in terms of the cavity FSR_ν and cavity losses, such that:

$$\delta\nu = FSR_\nu \frac{Losses}{2\pi}, \tag{3.35}$$

which is defined here in units of linear frequency. Another important figure of merit for cavities is the *finesse* $\mathcal{F}$, which was defined in Equation 3.3 in terms of the mirror reflectivities R_1 and R_2. In this definition, it was assumed that the cavity losses are solely due to partial transmission through the mirrors, and thus the real finesse is generally less than that calculated using Equation 3.3. An alternative definition of the finesse that takes other sources of loss into account can be written as the ratio between the FSR and the cavity linewidth, $\delta\nu$:

$$\mathcal{F} = \frac{FSR_\nu}{\delta\nu} = \frac{2\pi}{Losses} \tag{3.36}$$

3.4.3 Quality Factor

The quality factor Q is another important cavity parameter that quantifies the deviation from the ideal lossless case. It is defined as the ratio of the total energy oscillating within the cavity to the energy dissipated per cycle, which can be written as:

$$Q = 2\pi \frac{\text{Energy stored}}{\text{Energy dissipated per cycle}} \tag{3.37}$$

The cavity quality factor can also be expressed as the ratio between the central frequency ν_q of the cavity mode and the mode linewidth, $\delta\nu$, such that:

$$Q = 2\pi \frac{\nu_q}{\delta\nu} = q\mathcal{F} \tag{3.38}$$

where the definition of ν_1 in Equation 3.31 and the definition of $\mathcal{F}$ in Equation 3.32 were used to write Q in terms of $\mathcal{F}$. From this expression, it is clear that higher quality factors are obtained from longer cavities.

3.4.4 Mode waist and mode volume

One of the main advantages of FBFP microcavities is their rather small mode volume, which is essential to obtain high Purcell factor. The minimum cross-sectional beam radius within the cavity is referred to as the cavity mode waist, ω_0, and is generally defined as [48]:

$$\omega_0 \approx \sqrt{\frac{\lambda}{\pi}} \left(d \frac{ROC_1\, ROC_2}{ROC_1 + ROC_2} \right)^{\frac{1}{4}} \tag{3.39}$$

Here ROC_1 and ROC_2 are the radii of curvature of the two cavity mirrors, and d is the cavity length. The cavity used in this work consisted of a fiber micro-mirror with (ROC_f) on the order of tens of micrometers, and a planar substrate mirror. When the radii of the mirrors are not comparable, the expression above is rewritten as [48]:

$$\omega_0 \approx \sqrt{\frac{\lambda}{\pi}} (d\, ROC_f)^{\frac{1}{4}} \tag{3.40}$$

Given the cavity mode waist and the length of the cavity, the mode volume can be obtained using [48]:

$$V = A.d = \frac{\pi}{4} \omega_0^2 d, \tag{3.41}$$

where $A = \pi\omega_0^2/4$ is the effective mode area. This shows that a short cavity and a small ROC_f are necessary to obtain a small mode volume, and consequently a stronger Purcell effect.

3.4.5 Fiber-cavity coupling

One of the main advantages of the FBFP microcavity is that the fiber is used both as a mirror and for direct coupling of the light into and out of the cavity, without the need for additional optics to match the input mode to the cavity mode. In this case, the coupling efficiency depends on mode matching between the cavity mode and the mode of the fiber. This can be approximated for a single-mode fiber by [48]:

$$\epsilon = \left(\frac{2w_f w_m}{w_f^2 + w_m^2} \right)^2 \tag{3.42}$$

where w_f is the mode field radius of the fiber, and w_m is the cavity mode's radius. To put this into perspective, we consider the mode field radius of the single-mode fibers used for the cavity experiments performed in this work, which was 3 μm. For a cavity resonant with the 892 nm transition of Nd^{3+} , with a length of 8λ, and a fiber micro-mirror with ROC$_f$ = 30 μm, the cavity mode radius on the mirror would be $\sim$ 2 μm. In this case, the mode-matching efficiency of cavity mode well-aligned with the fiber axis would be $\sim$ 85%.

3.4.6 Purcell factor in terms of finesse and mode waist

The Purcell factor was expressed in Equation 3.29 in terms of Q, which is proportional to the cavity length, and the mode volume, which is inversely proportional to the cavity length. Consequently, there is a trade off between Q and V to get to the optimal Purcell factor. The Purcell factor can also be written in terms of the cavity Finesse, $\mathcal{F}$, and the mode waist ω_0:

$$P = \frac{3}{4\pi^2} \frac{q\mathcal{F}}{A.d} \left(\frac{\lambda}{n} \right)^3 = \frac{6}{4\pi^2} \frac{\mathcal{F}}{A} \left(\frac{\lambda}{n} \right)^2 \tag{3.43}$$

where the relations given in Equations 3.31, 3.38 and 3.41 were used in this expression. This is the definition used throughout Chapter 5 to estimate the Purcell factors in the experiments.

CHAPTER 4

NEODYMIUM AS A CANDIDATE READOUT ION

One of the main scalable REIs based quantum computing schemes relies on using a dedicated readout ion to probe the state of single qubit ions [53, 54]. In this scheme, fluorescence will only be emitted by the readout ion if the qubit is prepared in one of its two possible quantum states. Consequently, the state of the qubit ion can be identified, depending on the detected fluorescence emission. This readout scheme has been discussed in detail in Refs. [54–58].

In this chapter, the spectroscopic properties of neodymium ions, Nd^{3+} , in Y_2O_3 nanocrystals are investigated as a candidate readout ion. The single qubit ion readout scheme and the requirements of the combination of readout and qubit ions are discussed in Section 4.1. The spectroscopic properties of Pr^{3+}-Nd^{3+}:Y_2O_3 investigated are then presented in Section 4.2. Finally, the potential of Nd^{3+} as a readout ion is discussed in Section 4.3.

4.1 Overview of the single-ion qubit Readout scheme

In an REI-based quantum computing scheme, scalability requires the ability to readout the final state of a single qubit ion, as discussed in Section 2.2. Direct readout of the qubit state by measuring its fluorescence is challenging for two main reasons. Firstly, the spontaneous emission rate is rather low due to the long lived excited state. One way to overcome this problem is to use the Purcell effect to enhance the spontaneous emission rate. The second problem, however, is that there is a finite probability that the excited qubit ion will decay to any of the hyperfine ground states, which are used as qubit states, leading to a loss of the quantum information. This also means that the qubit transitions can not

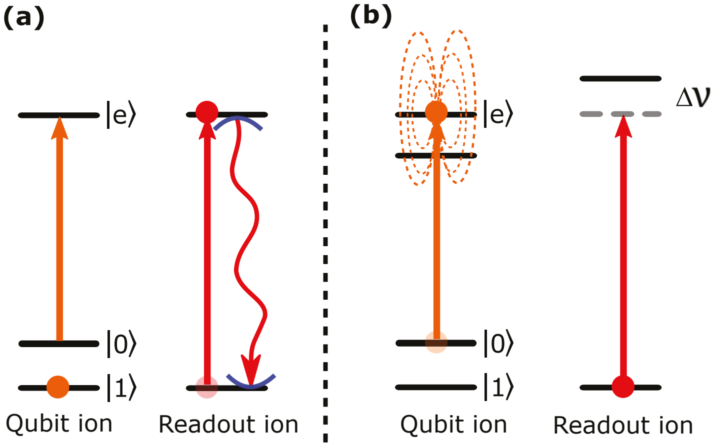

Figure 4.1: The readout scheme of a single qubit ion using a separate readout ion. The scheme and the figure are described in the text.

be cycled to yield sufficiently high fluorescence signal, which is important for high-fidelity readout of the qubit state.

An alternative approach, adopted in this work, is to couple the qubit ions to a separate readout ion. The readout ion itself is coupled to a high finesse cavity to enhance its spontaneous emission via the Purcell effect, and to use its fluorescence to identify the qubit state in a non-demolishing measurement. The single-ion readout scheme discussed here utilizes the fact that REIs can have permanent electric dipole moments μ_g and μ_e in their ground and excited states, respectively. Consequently, neighboring ions can affect each other via permanent electric dipole-dipole interactions. The interaction mechanism between a readout ion used to probe the state of a neighboring qubit ion is illustrated in Figure 4.1 (a) for the case of a qubit in state $|1\rangle$ and in Figure 4.1 (b) for the case of a qubit in state $|0\rangle$. The readout scheme can be summarized as follows:

- A π pulse resonant with the $|0\rangle \rightarrow |e\rangle$ transition of the qubit ion is applied, after which the transition of the readout ion is driven by a resonant field. The transition of the readout is coupled to a resonant high-finesse microcavity to enhance the spontaneous emission of the excited state if the ion is excited.

- When the qubit is in state $|1\rangle$, as shown in Figure 4.1 (a), the π pulse resonant with $|0\rangle \rightarrow |e\rangle$ does not excite the qubit ions, and the qubit ion thus has no effect on the readout ion in this case. The neighboring readout ion is then excited by a resonant driving field. The emission of the excited state is enhanced and collected by the cavity. This process can be cycled many times to increase the collected fluorescence signal. In the case illustrated here, the collected fluorescence indicates that the qubit was in the $|1\rangle$ state.

- When the qubit is in state $|0\rangle$, as shown in Figure 4.1 (b), the qubit will be driven to the $|e\rangle$ state by the resonant π pulse. As a result of the change in the permanent electric dipole moment, the transition of the neighboring readout ion is shift by $\Delta\nu$, which depends of $\Delta\mu_{eg} = \mu_e - \mu_g$ and on the separation between the ions. Consequently, the readout driving field will no longer be resonant with the detuned transition of the readout ion. Thus the readout ions will not be driven to the upper level when excited, and no fluorescence signal will be produced. The absence of the fluorescence signal in this case indicates that the qubit was in the $|0\rangle$ state.

Certain requirements must be fulfilled by both of the qubit ion and the readout ion for this scheme to work. For the qubit ion, long optical and hyperfine coherence times are essential to preserve the quantum state. In this respect, Eu^{3+} is one of the most promising qubit candidate ions, with an optical coherence time of 2.6 ms [59], and a ground hyperfine coherence time as long as hours in Y_2SiO_5host under certain conditions in Y_2SiO_5host [8]. $Pr^{3+}$is another interesting qubit candidate that has been extensively investigated, and was used in the first demonstration of spin qubit gates [9]. In Y_2SiO_5host, Pr^{3+}has an optical coherence time of 152 μs [60], and a hyperfine coherence time of 42 s [61].

Regarding the readout ion, a short excited state lifetime with a high fluorescence yield at the single ion level is necessary to obtain a sufficiently large difference between the number of photons collected from the readout ion in the two possible qubit states, to ensure efficient readout of the qubit state. Furthermore, a narrow homogeneous linewidth of the readout ion and a strong permanent electric dipole-dipole interaction with the qubit ion are necessary [57]. The interaction must be strong enough to shift the resonance frequency of the readout ion by a few homogeneous linewidths such that it is off-resonance with the driving field, as was shown in 4.1 (b). In addition, the transition of the readout ion will need to be cycled to yield sufficiently high fluorescence, which means that long lived trapping energy levels must be avoided. Spectral overlaps between the qubit ion and the readout ion must also be avoided as this could reduce the fluorescence yield, and more importantly, could perturb the qubit state if, for example, the emission of the readout ion was absorbed by the qubit ion [62].

In this work, Nd^{3+} ions in Y_2O_3 nanocrystals and coupled to a microcavity to reduce the excited state lifetime was investigated as a candidate readout ion. The spectroscopic properties are discussed in the next section.

4.2 Spectroscopic properties of Nd^{3+}:Y_2O_3 nanocrystals

Neodymium is the fourth rare earth element with an atomic number of 60. The electronic configuration of the trivalent ion Nd^{3+} is [Xe]4f^3. There are seven stable isotopes of neodymium, ^{142}Nd, ^{143}Nd, ^{144}Nd, ^{145}Nd, ^{146}Nd, ^{148}Nd, ^{150}Nd. The five isotopes with even atomic numbers have zero nuclear spin, and a combined abundance of 79.5%, while the remaining two, with an odd atomic mass number, have a nuclear spin of 7/2 and a combined abundance of 20.5%. The isotopes without nuclear spin are simpler to work with as they naturally give closed cycling transitions at no magnetic fields, and thus only these ions will be considered here. Two Nd^{3+}:Y_2O_3 samples were investigated in the present work, both were prepared by the group of Professor Philippe Goldner at CNRS, Paris. The first sample that was investigated in this work was Y_2O_3 ceramic doped with Nd^{3+} ions at a concentration of 100 ppm. The other kind of sample investigated was Y_2O_3 nanocrystals with an average diameter of 380 nm, co-doped with Nd^{3+} and Pr^{3+}at concentrations of 100 ppm and 500 ppm, respectively. A detailed description of the synthesis processes can be found in Paper I. A third nanocrystal sample with an average diameter of 160 nm was investigated in the cavity experiments. (The characteristics of this sample are described in the next chapter.)

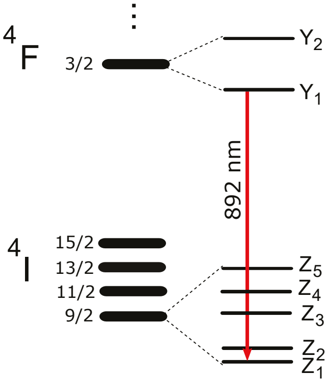

Figure 4.2. *Relevant energy level structure of a Nd^{3+} in a crystal, showing the Kramers doublets of the ground and the upper levels. The zero phonon line (ZPL) $Y_1 \rightarrow Z_1$ transition indicated by the red solid line was investigated in this work.*

4.2.1 Level structure

The emission and absorption characteristics of Nd^{3+}:Y_2O_3 have been previously investigated by Walsh *et al* [63]. The relevant level scheme of the Nd^{3+} ion in Y_2O_3 is shown in Figure 4.2. When excited to the $^4F_{3/2}$ state, the ion can decay to four possible ground manifolds, $^4I_{9/2}$, $^4I_{11/2}$, $^4I_{13/2}$, and $^4I_{15/2}$, with branching ratios of 51.4%, 43.5%, 5%, and 0.1%, respectively [63]. The transition of interest in the present work is the $^4F_{3/2} - {}^4I_{9/2}$ transition, which has one of the highest oscillator strengths of all the rare earth 4f-4f transitions [64]. Since Nd^{3+} is a Kramers ion, the crystal field splits the $^4I_{9/2}$ state to 5 Kramers doublets (Z_1-Z_5), and the $^4F_{3/2}$ to two Kramers doublets (Y_1 and Y_2). Each of the doublets can be further split into two singlets in the presence of a magnetic field. Figure 4.3 shows the florescence spectrum of the $^4F_{3/2}(Y_1) - {}^4I_{9/2}(Z_1)$, with the five peaks corresponding to decays to the five Kramer doublets. The Zero phonon line (ZPL) between the lowest Kramer doublets, ($^4F_{3/2}(Y_1) - {}^4I_{9/2}(Z_1)$), at a wavelength of 892 nm has a total branching ratio of 23%. A high branching ratio implies a high collection efficiency of the fluorescence at this line, which is one of the reasons why this transition is investigated for application in single-ion readout.

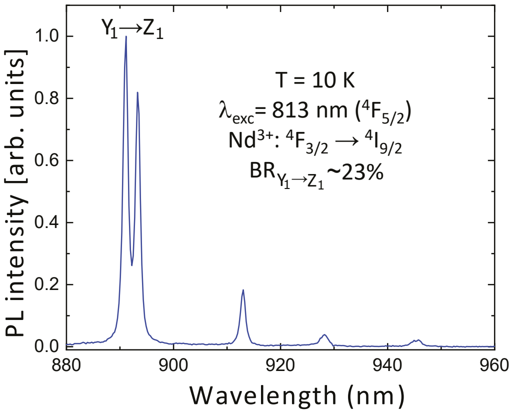

Figure 4.3: Fluorescence spectrum of Nd^{3+} in Pr^{3+}-Nd^{3+}:Y_2O_3 nanocrystals at 10 K. The measurement was performed by Diana Serrano at CNRS, Paris. A 813 nm laser was used to excite the ions to the $^4F_5/2$ level, which decays non-radiatively to the relevant $^4F_3/2$ level. The five peaks shown in the figure correspond to decays to the five possible Kramers doublets (Z_1-Z_5) of the $^4I_{9/2}$ shown in Figure. 4.2

4.2.2 Experimental setup

The optical setup used for the spectroscopic characterization of Nd^{3+}:Y_2O_3 is shown in Figure 4.4. A CW Ti:sapphire laser operating at a wavelength of 892 nm was used to target the $^4F_{3/2}(Y_1) - {}^4I_{9/2}(Z_1)$ transition. A double pass AOM was utilized for pulse shaping. In order to compensate for intensity fluctuations, 10% of the light was focused into a reference detector before the sample. The rest of the light ($\sim$10 mW) was focused on the sample. The sample was fixed to a copper holder with a pinhole, and was mounted inside a bath cryostat at 2.15 K. The nanocrystal powder was contained in a custom-made holder where the thickness of the powder layer was $\sim$500 μm. Since the samples were highly scattering, a lens was mounted on the same copper holder after the sample to collimate the fluorescence signal. The transmission was then focused onto an APD. A 900 nm long-pass filter was inserted before the detector to filter out the excitation light while transmitting the fluorescence when measuring the lifetime and the inhomogeneous linewidth.

4.2.3 Inhomogeneous linewidth and lifetime

The inhomogeneous linewidth of the $^4F_{3/2}(Y_1) - {}^4I_{9/2}(Z_1)$ transition was measured by scanning the excitation wavelength while detecting the fluorescence emitted at $\lambda > 900$ nm. The results

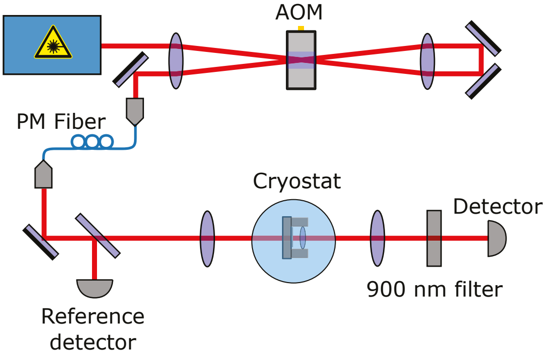

Figure 4.4: Optical setup used in the Nd^{3+} spectroscopy experiments.

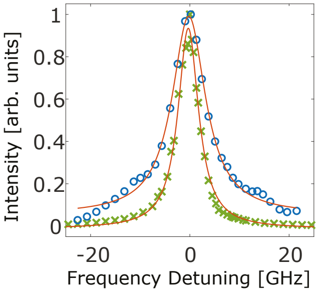

Figure 4.5. *Inhomogeneous linewidth of the ZPL of* Nd^{3+} *in* Pr^{3+}*-*Nd^{3+}*:*Y_2O_3 *for the ceramic sample (green crosses), and for the nanocrystals sample (blue circles). The red lines show a Lorentzian fits, from which linewidths of 5 GHz and 8.2 GHz were extracted for the ceramic and the nanocrystal samples, respectively.*

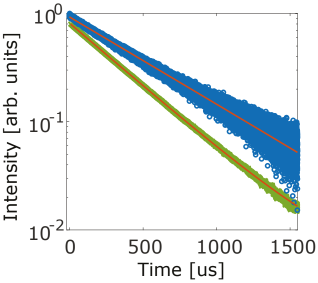

Figure 4.6. *Lifetime of the excited state of* Nd^{3+} *in the* Y_2O_3 *ceramic sample (green crosses), and in the* Pr^{3+}*-*Nd^{3+}*:*Y_2O_3 *nanocrystals sample (blue circles). The red lines show single exponential fits, which give lifetimes of 373* μs *and 540* μs *for the ceramic and the nanocrystal samples, respectively.*

of this measurement are shown in Figure 4.5. For the ceramic sample, an inhomogeneous linewidth of 5 GHz was extracted from a Lorentzian fit to the measured fluorescence, with the line centered at 892.17 nm. The line was blue shifted to 892.16 nm for the nanocrystal sample, with a broader linewidth of 8.2 GHz. The blue shift and the broadening of the line in the nanocrystal sample can be attributed to the high content of Pr^{3+}which was doped at concentration of 500 ppm [18, 65, 66]. The excited state lifetime (T_1) was also measured by pulse excitation of the transition followed by fluorescence detection. An exponential fit to the fluorescence decay, shown in Figure 4.6, gave T_1 of 373 μs and 540 μs for the ceramic and nanocrystals, respectively. Previous studies have shown a reduction in the lifetime of Eu^{3+} ions doped in Y_2O_3 nanocrystals when they were embedded in a PMMA layer with a refractive index of ~ 1.5 [67, 68]. This could explain the reduced lifetime observed in the ceramic sample compared to the nanocrystals since the change in the refractive index surrounding the ions in the ceramic is much less than that in nanocrystals. The lifetime measurement of the excited state gives some indication of the microcavity parameters that will be required for single-ion readout.

4.2.4 Homogeneous linewidth

The homogeneous linewidth of the ${}^4F_{3/2}(Y_1) - {}^4I_{9/2}(Z_1)$ transition was measured using the two-pulse photon echo technique [69]. The pulse sequence is illustrated in Figure 4.7. First, a $\pi/2$ pulse is applied to excite the ions into a superposition state. Due to the inhomogeneous broadening of the ions, they start to dephase. A second π pulse applied after a time τ flips this dephasing, such that the ions are in phase again after a time τ after the second pulse. When the atoms are in phase, they coherently emit a strong photon echo since atoms in phase emit with a quadratic dependence of the number of atoms, compared to atoms emitting with random phases. Since the nanocrystal sample used here was highly scattering, both pulses used had the same pulse area, 400 ns long with a power of 10 mW. The 900 nm long-pass filter was removed for these measurements since the echo is emitted in the same mode as the excitation pulses. The waiting time between the two pulses was increased stepwise while observing the photon echo at each time. The decay was fitted with the following exponential [23]:

$$I(\tau) = I_0 \times e^{(-4\tau/T_2)} \tag{4.1}$$

where I is the intensity of the echo at different delays τ between the two pulses, I_0 is a normalization constant, and T_2 is the coherence time, which is related to the homogeneous linewidth according to Equation 2.3. A coherence time of 5.14 μs corresponding to a homogeneous linewidth of 62 kHz was measured at a temperature of 1.6 K. The homogeneous linewidth measurement was repeated at different temperatures to investigate the dephasing mechanisms, and the results can be seen in Figure 4.8.

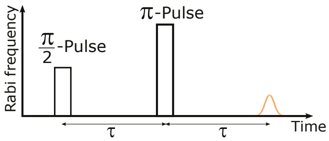

Figure 4.7. *A two-pulse photon echo sequence. A $\pi/2$ pulse excites the ions into a superposition state, after which the ions start to dephase. A π pulse is applied after a time τ, which flips the dephasing and leads to rephasing and the emission of a strong photon echo a time τ after the second pulse.*

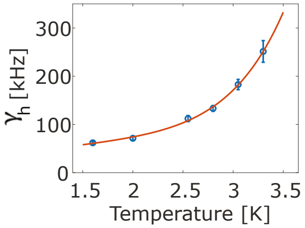

Figure 4.8. *Homogeneous linewidth as a function of temperature. The measurement (blue) was fitted to Equation 4.2 (orange). The error bars represent 95% confidence intervals obtained from fitting the echo decays to Equation 4.1.*

The homogeneous linewidth was fitted to the following function [70]:

$$\gamma_h(T) = \gamma_0 + \alpha_{TLS}T + \alpha_R T^7, \tag{4.2}$$

where T is the temperature, and γ_0 is the linewidth extrapolated to 0 K, which was extracted from the fit and found to be 20 kHz. α_{TLS} quantifies the dephasing due to coupling to TLS which is a fluctuation between TLS configurations with similar energy that leads to a loss of coherence. The contribution of TLS dephasing was $\alpha_{TLS} = 24$ kHz. α_R quantifies dephasing due to coupling to two-phonon Raman processes [71], which was found to be $\alpha_R =$ 23 Hz//K^7.

The homogeneous linewidth was also investigated at different magnetic fields. The photon echo decay showed some modulation when certain fields were applied, as can be seen in Figure 4.9. The decay curve was fitted to the following equation [72]:

$$I(\tau) = I \times e^{(-4\tau/T_2)} \times [1 + (m \times cos^2(\omega t/2)], \tag{4.3}$$

where m is the modulation amplitude, and ω is the modulation frequency, which ranges from 200 kHz to 900 kHz. This is the same range of modulation observed in Nd^{3+}:YVO$_4$, which was attributed to superhyperfine interactions between the Nd^{3+} ions and the nuclear spin of the surrounding Y^{3+} ions in the host, which contributes to the broadening of the homogeneous line. A more detailed discussion of the magnetic field dependence can be found in Paper I. Due to the combination of low output power from the dye laser system at 619 nm wavelength, and the highly scattering nature of the nanocrystal sample, it was not possible to observe a

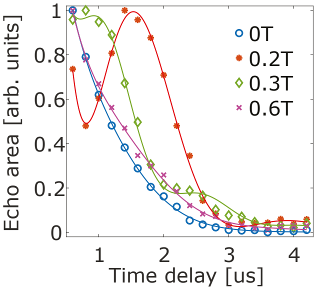

Figure 4.9. *Photon echo decays at different magnetic fields.*

photon echo when trying to excite the Pr^{3+}ions with two pulses. This prevented the investigation of the interaction between the Nd^{3+} and Pr^{3+}ions.

4.3 Estimations of readout fidelity

In order to estimate the readout fidelity of a single qubit ion, Pr^{3+}in our case, through the fluorescence of the Nd^{3+} readout ion coupled to a high-finesse cavity, the model proposed by Debnath *et al* was used [55]. This model is based on a Bayesian analysis of the photons detected from the readout ion to extract information on the state of the qubit ion. The fidelity of the state readout can also be estimated by comparing the integrated fluorescence signal from the readout ion for the two states of the qubit as explained in Section 4.1 [54]. For practical applications, the qubit state should be read out swiftly, with as high fidelity as possible. Bayesian analysis provides optimized processing of the fluorescence signal that includes information about the temporal correlations and the timing between the detected photons. This leads to faster readout with higher fidelity than that possible when the readout is based solely on the integrated fluorescence signal.

In this model, the decay rate of the excited state of the readout ion is replaced by the detection rate. Furthermore, the frequency shift due to the dipole-dipole interaction between the qubit ion and the readout ion must be significantly greater than 1/decay rate, in order to block the excitation of the readout ion and hence separate the qubit states. The frequency shift due to the dipole-dipole interaction is given by the following approximation [73]:

$$\Delta\nu_{ij} = \frac{\Delta\mu_i \Delta\mu_j}{4\pi h \epsilon_0 r^3}\kappa, \tag{4.4}$$

where $\Delta\mu_i$ and $\Delta\mu_j$ are changes in the static dipole moment between the ground and the excited state of the the qubit and readout ions, respectively. h is Planck's constant, ϵ_0 is the permittivity of vacuum, r is the separation between the two ions, and κ quantifies the angular dependence of the interaction. The change in the dipole moment between the ground and excited states has been measured previously for Pr^{3+}ions [73]. For two Pr^{3+}ions separated by 5 nm, a frequency shift of $\sim$ 10 MHz is expected. This can be used as an-order-of magnitude estimate of the frequency shift between a Nd^{3+} ion and a Pr^{3+}ion. It should be noted that the doping concentration of the qubit ion can be optimized such that there is an an abundance of qubit ions strongly interacting with the readout ion.

In order to ensure a clear distinction between the qubit states, we assume that the interaction shift is 10 times the desired detection rate, i.e., 1 MHz. The detection rate can be expressed as:

$$\text{Detection rate} = \text{Decay rate} \times \text{Optical efficiency}, \tag{4.5}$$

where the optical efficiency here includes the collection efficiency and the detection efficiency. In order to achieve a 1 MHz detection rate with the proposed readout ion, Nd^{3+} , we consider Purcell enhancement of the excited state to reduce the lifetime to 100 ns (corresponding to a homogeneous linewidth of 1.6 MHz using Equation 2.3) using a fiber-based microcavity with a total optical efficiency of 10%. Such a collection efficiency is reasonable for fiber-based microcavities since the fiber is used both as a mirror and for collection.

Using Pr^{3+}as a qubit ion, with an excited state lifetime of 140 μs [72], and given the assumptions above, a readout fidelity of 94% is expected after 10 μs, based on Bayesian analysis [55]. If Eu^{3+} is instead considered as a qubit ion, with an excited state lifetime of $\sim$ 2 ms [8, 67], the readout fidelity increases to $\sim$ 99% after 10 μs. This fidelity is limited by the finite lifetime of the qubit ion, which causes loss of the state information if it spontaneously decays during the detection.

4.3.1 Cavity and material requirements

Finally, given the measurements in Section 4.2 and the assumptions above, Equation 3.43 can be used to estimate the Purcell factor needed to obtain this level of readout fidelity. In order to shorten the lifetime of the proposed $^4\mathrm{F}_{3/2}(Y_1) - {}^4\mathrm{I}_{9/2}(Z_1)$ readout transition of Nd^{3+} from 540 μs to 100 ns, an effective Purcell factor of $\sim$ 5000 would be required, which takes into account the 23% branching ratio of the transition. Such Purcell enhancement could be achieved using a cavity with a finesse of 3×10^5 and a length of 3λ, where $\lambda = 892$ nm in our case. It would be difficult to obtain this level of finesse using the 380 nm nanocrystals discussed in this chapter, since the scattering losses introduced by a single nanocrystal are a few percent. The scattering losses scale with $1/r^6$, where r is the radius of the nanocrystal; this dependence is discussed in more detail in the next chapter. If we instead consider a nanocrystal that is 80 nm in diameter, the scattering losses would be reduced to 5 ppm. Using this nanocrystal in a microcavity with mirrors that have a total transmission of 10 ppm, which is experimentally feasible [74], would give the required 3×10^5 finesse, based on Equation 3.36.

CHAPTER 5

TOWARDS SINGLE NEODYMIUM ION DETECTION IN A MICROCAVITY

This chapter describes the experiments carried out using the microcavity. Section 5.1 discusses the technical aspects considered during the design of the cavity. The overall structure of the microcavity and its main components are then presented in Section 5.2. One of the main cavity components is the fiber mirror, and Section 5.3 describes the machining and characterization of this mirror on the fiber facet, followed by the coating procedure. Section 5.4 describes the stability requirements and cavity locking. In order to use the cavity for ion detection, a suitable nanocrystal must first be identified. This was achieved by mapping the scattering losses inside the cavity using scanning cavity microscopy. Different methods of doing this and an experimental demonstration are presented in Section 5.5. The optical setup used for pulse creation and fluorescence detection is presented in Section 5.6. Finally, room-temperature and cryogenic measurements are discussed in Sections 5.7 and 5.8, respectively.

5.1 Technical considerations

Before designing and constructing the microcavity, the following criteria were considered.

Cryogenic compatibility

Since this work was aimed at detecting a single Nd^{3+} ion, which will be used to read out the state of a qubit, it is important to protect the qubit from decoherence. Phonons are one of the main contributors to the loss of coherence [75, 76]. In order to eliminate phonons or minimize their effects, the experiments must be performed at a low temperature. In this work, this is achieved

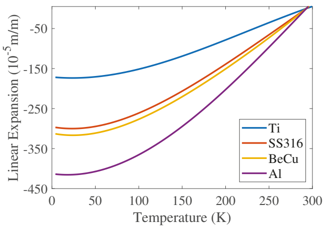

Figure 5.1. *Linear expansion as a function of temperature for: Titanium (blue), grade 316 stainless steel (SS216) (red), beryllium copper (yellow) and aluminum (purple) [77].*

by placing the whole cavity setup in a bath cryostat that can be cooled down to a temperature of 2.17 K. The properties of materials change significantly when they are cooled to such low temperatures. One such property that must be considered when deciding which materials to use in the cavity is the thermal expansion. Figure 5.1 shows the linear expansion of some common solids as a function of temperature [77], where it can be seen that titanium has a lower thermal expansion coefficient than some other materials. Titanium was thus chosen as the building material for all cavity components. The stepper positioners used in the setup are also made of titanium, which makes the relative expansion/contraction of the whole assembly rather low. Grade 4 titanium screws were mostly used to attach different parts together. Stycast 1266 cryogenic epoxy was also used.

Mechanical stability

A high degree of mechanical stability is necessary to ensure that the cavity mode overlaps well with the $^4\mathrm{F}_{3/2}(Y_1) - {}^4\mathrm{I}_{9/2}(Z_1)$ transition of the Nd^{3+} ion throughout the measurement time. This becomes especially important when working with high-finesse cavities. Since the cavity is placed inside a cryostat, it will be directly coupled to several sources of vibration such as pumps, boiling cryogenics, etc. This places high demands on the mechanical stability of the cavity setup, especially along the cavity axis.

Scannability

In order to identify a “suitable” single nanocrystal, the relative position of the fiber tip with respect to the substrate must be scannable on the nano-scale. The cavity length should also be tunable in sub-wavelength steps to compensate for fast vibration and slow drifts in the cavity resonance.

Space limitation (compactness)

The size of the space available for the sample inside the cryostat is 25 mm, which places an upper limit on the size of the cavity setup.

5.2 Cavity structure overview

Although it is possible to meet some of the requirements above separately, meeting all at the same time was found to be difficult. In particular, the limited space lead to cavity structures that are inherently unstable. The cavity structure used in this work is shown in Figure 5.2 where the main components are included. The fiber is glued to a 5 × 5 × 1.8 mm v-grove fixed to a small piezoelectric chip [1]. The piezo chip is glued to a larger adaptor

---

[1] Thorlabs Shear Piezoelectric Chips PL5FBP3

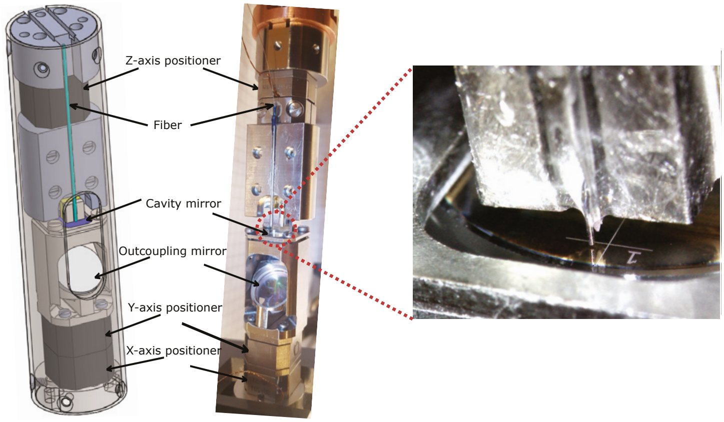

Figure 5.2: Left: Illustration and photograph of the cavity assembly showing the main components, Right: A close-up of the fiber-mirror interface, showing a cross pattern machined on top of the mirror. The reflection of the fiber can also be seen on the mirror.

that is attached to an ANPz51 stepper attocube positioner. The attocube itself is attached via a titanium adapter to a 1 m long sample rod used to introduce the cavity setup into the cryostat sample chamber. In the lower half of the cavity, the other cavity mirror, with a diameter of 12.4 mm, is mounted on top of a cage holder. A fixed mirror inside the cage at an angle of 45°is used to out-couple cavity transmission out of the cryostat to a photo-diode through the cryostat window. The cage holder is mounted on top of two ANPx51 stepper attocube positioners mounted on top of each other. The positioners are discussed in more detail below.

5.2.1 Positioners

Attocube stepper positioners, ANPx51 and ANPz51 were used in the cavity, due to their small size, cryogenic compatibility, micro-scale tuning, and availability at the beginning of this work. The steppers work by the slip-stick mechanism, which uses the non-linear form of friction together with saw-tooth-like driving in order to push the stage forward. This has the advantage of giving relatively long scanning ranges, 3 mm for the ANPx51, and 2.5 mm for the ANPz51, making them suitable for long-range tuning of the cavity in three directions. However, there are some drawbacks. Slip-stick motion has low reproducibility, which makes it difficult to reliably map an area on the mirror. This is be discussed in more detail in Section 5.5.1. The other disadvantage of the slip-stick mechanism is the vibration introduced when it is driven. The resonance frequencies under an applied load can be

Axis / Pos.	m_0 (g)	f_0 (Hz)	m_L (g)	f_L (Hz)
X / ANPx	1.63	2462	3	1460
Y / ANPx	1.63	2462	10	921
Z / ANPz	4.16	2576	15	1200

Table 5.1: Resonance frequencies of the stepper positioners used in the cavity. m_0 is the intrinsic mass carried by the stepper piezo without any additional load and f_0 is the frequency without any load. m_L is the mass carried on top of each attocube, and fL is the frequency with a load.

calculated using the following expression [78]:

$$f_{res}(m_L) = \frac{1}{2\pi}\sqrt{\frac{K}{m_0 + m_L}} \tag{5.1}$$

where K is the stiffness of the system, which is 0.39 N/μm for ANPx51, and 1.09 N/μm for ANPz51, according to the manufacturer [78]. m_0 and m_L are the intrinsic mass resting on top of the stepper piezo and the load mass, respectively. Table 5.1 gives the resonance frequencies of the different positioners with and without the load each carries once assembled in the cavity.

The two ANPx51 steppers, mounted on top of each other at an angle of 90°, are used to move the mirror in the horizontal plane with respect to the fiber. This is used later in the scanning microscopy imaging of the sample prepared on top of the mirror and to locate a suitable nano-crystal on which to perform the measurements. The ANPz51 positioner is used for coarse vertical positioning of the fiber, and thus tuning the cavity length. This is useful to compensate for drifts in cavity length when cooling the cavity, or when performing SCM, as well as other slower drifts in the cavity length. Additionally, the shear piezo on top of which the fiber is glued was also used for fast and fine tuning of the vertical fiber position along the cavity axis. It has a scan range of ~ 1.3 μm at room temperature and a resonance frequency of 1.9 MHz (without load), it is used for fast cavity locking [2]. Cavity locking is further discussed in Section 5.4.

5.3 Fiber machining and coating

The fiber mirror is one of the key components of the cavity. In order to create the desired profile on the end facet of the fiber, high power 10.6 μm CO_2 laser pulses were used to melt and evaporate certain regions of the end facet. This was done in collaboration with the group of Professor David Hunger at KIT using their setup. A detailed description of their setup has been presented previously

---

[2] PL5FBP3 - Shear Piezo Chip from Thorlabs

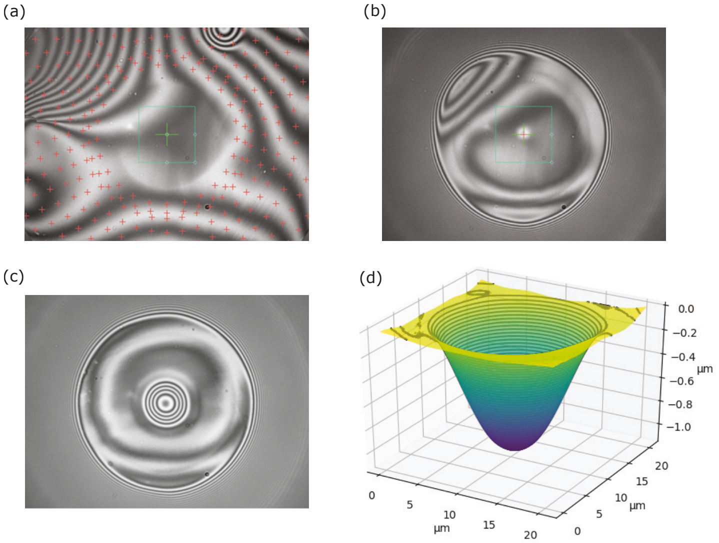

Figure 5.3: White light interferometric image of the endfacet of a fiber (a) before and (b) after cropping the outer edge of a fiber. (c) A cropped fiber After shooting its profile in the center. (d) 3D reconstruction of the machined profile on the end facet of the fiber (same fiber in (c)), giving a ROC=30 μm, depth=1.2 μm extracted from a parabolic fit.

[79]. The fibers used throughout the present work were custom-made, single-mode, copper coated, pure silica core fibers [3]. Firstly, the copper coating was removed from $\sim$ 30 mm of the fiber end by soaking it in an iron chloride ($FeCl_3$) solution for $\sim$5 minutes.[4] The etched fiber was then cleaned using low-lint wipes and ethanol to remove any residual copper and FeCl3 solution. The fiber was then cleaved using a commercial cleaver. The cleaved fibers were then mounted on a holder that can accommodate up to 11 fibers. The holder was designed by David Hunger's group to facilitate the positioning of fibers in the machining setup, and to later stack several holders in the coating chamber [79]. The machining setup consists of three main stages; a microscope with a wide angle of view to locate the fiber, a 10.6 μm high-power pulsed CO_2 laser to create the desired structures on the fiber end facet, and a white-light interferometer to measure and analyze the machined profiles. The fiber holder is fixed in a 3-axis micro-positioner that can align the fiber in any of the three stages mentioned above. By tuning the beam waist of the CO_2 light on the cleaved fiber end facet,

---

[3] The fiber were custom made by IVG Fibers

[4] This solution was prepared by mixing 50 g of $FeCl_3$ powder with 60 ml distilled water, iron(III) chloride hexahydrate puriss sigma-aldrich id:31232-250g-M).

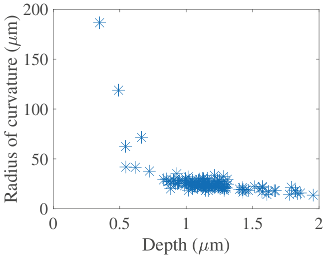

Figure 5.4. *The distribution of the obtained radius of curvature against the depth. Majority of the machined profiles had* $\sim 1\ \mu m$ *depth, and* $\sim 30\ \mu m$ *radius.*

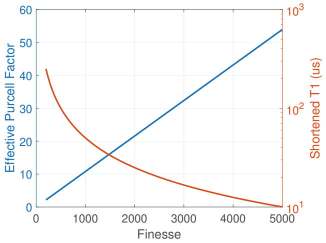

Figure 5.5. *Effective Purcell factor (blue) and the shortened lifetime (orange) as a function of the finesse.*

the pulse power, the number of pulses, and the duration between pulses, it is possible to obtain a wide range of radii of curvature and depths, while maintaining a rather low surface roughness to allow for high reflectivity coating [48, 80].

Before machining the mirror profile, the outer edge of the fiber was cropped using high-power pulses. This makes it possible to obtain shorter cavity lengths and allows for angular alignment. Figures 5.3 (a) and (b) show white-light interferometric images of the cleaved fiber end facet before and after cropping, respectively. In this work, the targeted ROC was between 20 μm and 30 μm and the depth was $\sim$1 μm. The machining parameters, such as the number of pulses, duration, etc., were tested and adjusted on sample fibers to obtain the target ROC and depth. Once the target was reached, the parameters were fixed and machining was conducted on the experimental fibers.

A white-light interferometric image of one of the machined profiles is shown in Figure 5.3 (c). White and black lines show the interference fringes, and knowing the wavelength ($\lambda_{WLI} = 463.25nm$), it is possible to deconvolute the phase to reconstruct a contour map of the profile created, as shown in Figure 5.3 (d), containing information on the ROC and depth [48, 49]. In total, over 150 fibers were machined, and the distribution of the obtained ROC is shown as a function of the depth in Figure 5.4.

5.3.1 Mirror coating

In this work, the aim was to initially use three values of finesse, namely 600, 1000, and 3000. These correspond to shortened lifetimes of $\sim$ 80, 50 and 20 μs, respectively, as can be seen from Figure 5.5 [5]. To achieve this, the mirror coating was designed to give reflectivities of 99.5% and 99.9% reflectivities at the ${}^4F_{3/2} - {}^4I_{9/2}$ transition of Nd^{3+} at 892 nm. Coating was performed by LaserOptik (Garbsen, Germany), and the transmission from the high-reflectivity coating is shown in Figure 5.6. In order to be able to have the samples closer to the field maximum in the cavity, and hence ensure a strong interaction with the ions, a layer of SiO_2 with a thickness of 0.847 $\frac{\lambda}{4}$, corresponding to a phase shift of 40°, was added as the top most layer of the Bragg mirror. Additionally, two mirrors each with a reflectivity of 99.994% at 900 nm were obtained from David Hunger's group. Combined with a fiber mirror with R = 99.9%, this provides a finesse of $\sim$ 6000.

---

[5] Here I ignore the reduction in finesse due to scattering by the samples, and I assume a cavity length of 30μm and a fiber mirror with ROC of 5λ

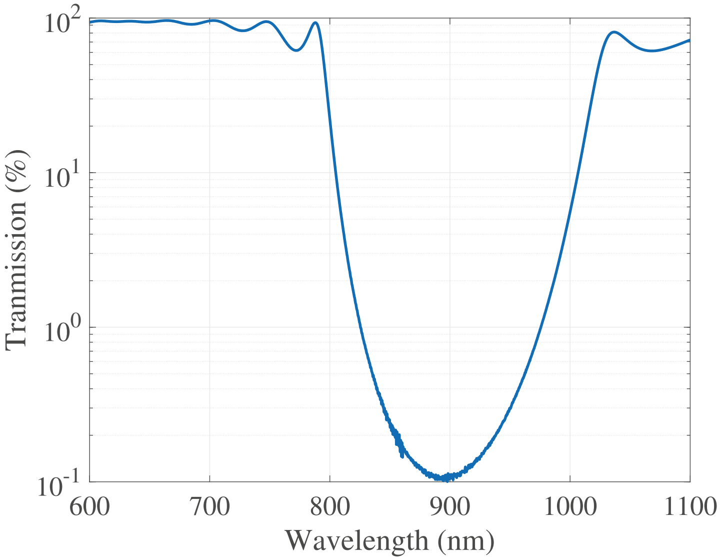

Figure 5.6: Transmission as a function of wavelength of the high reflectivity mirros measured by LaserOptik. The reflectivity at the central wavelength of 892 nm is 99.9%

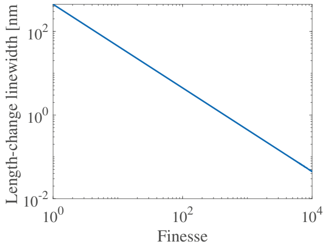

Figure 5.7. *Length-change linewidth as a function of finesses for a central wavelength of 892 nm.*

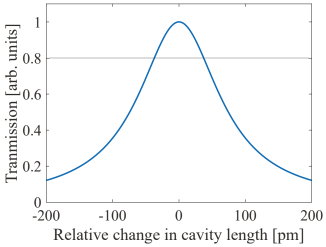

Figure 5.8. *Cavity resonance for a cavity with a finesse of 3000. The horizontal line indicates 80% transmission level. The tolerance in cavity length stability to ensure transmission is above 80% is 74 pm.*

5.4 Stability and locking

In order to ensure maximal coupling between the cavity mode and the ions, the cavity length must be highly stable. In order to estimate the tolerance in cavity length stability, the cavity resonance linewidth can be rewritten in terms of the change in cavity length (δd) ([81, 82]):

$$\delta d = \frac{\lambda/2}{\mathcal{F}} \tag{5.2}$$

Figure 5.7 shows the 'length-change linewidth' as a function of finesses for a central wavelength of 892 nm. At the highest relevant finesse in this work, which is 3000, the corresponding length-change linewidth is 148 pm. Assuming that the transmission of the cavity should be above 80% of the maximum, this translates into a cavity length stability of better than 74 pm, as shown in Figure 5.8.

.

This degree of mechanical stability is difficult to achieve passively in the present cavity, given the nature of the stepper positioners used, and the structure of the cavity, as discussed in Section 5.2, and the fact that it will be used inside a cryostat. In order to obtain such a high degree of stability, active stabilization will have to be employed. Several cavity stabilization techniques can be used, and detailed description of different schemes and their applicabil-

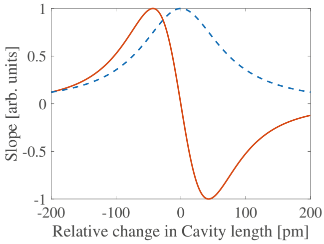

Figure 5.9. *Slope of the Lorentzian resonance (Orange) as a function of relative cavity length for a cavity with a finesse of 3000. The resonance of such cavity is shown in dashed blue.*

ity to the stabilization of the present setup can be found in Ref. [83]. PDH locking is one of the most common techniques used for laser locking [84]. However, due to the broad linewidth in short cavities (∼ 100 GHz), it would be difficult to find an electro-optic modulator that can generate such large frequency shifts between the carrier and the sideband, which is required for the PDH locking implementation.

Two locking schemes were investigated in this work: side-of-fringe locking and tilt locking [85]. The former was implemented and used in the experiments presented in this thesis. Tilt locking was investigated in a separate setup for potential use in future cavity setups. Only side-of-fringe locking is discussed in more detail here. A detailed discussion of the tilt locking implementation can be found in Ref. [83].

5.4.1 Side of fringe locking

In this method, the cavity transmission of a narrow-linewidth laser is used to generate an error signal. Ideally, the length of the cavity should be locked where the transmission is a maximum, i.e. at maximum resonance. Taking the maximum of the cavity fringe as the point of reference, if the cavity length drifts on either side of the maximum transmission, there is no way of knowing which side it was simply by looking at the cavity transmission. In order to obtain this kind of information, the reference point must be on either side of the fringe. This way, the transmission will increase or decrease depending on whether the cavity drifts towards shorter or longer lengths. In order to achieve maximum sensitivity to length change, the point with maximum slope on the side of the fringe is chosen as the locking point. The slope across the Lorentzian fringe for a 3000 finesse cavity is shown in Figure 5.9. The transmission at the point of maximum slope will be ∼ 75% of the maximum transmission.

By continuously monitoring the cavity transmission level, any change in the cavity length will be thus seen as a deviation in transmission from that in the reference point. Knowing the conversion factor between piezo chip driving voltage and the corresponding change in length, the deviation in transmission can be converted to an error signal that is fed back to the piezo chip to compensate for the change in cavity length.

A field-programmable gate array (FPGA) module running at a clock rate of 125 MHz with two inputs and two outputs of 14 bits, and a minimum latency of 200 ns [6], was used as a digital feedback controller. An open-source software package, (PyRPL) written in Python and installed on a client computer connected to the FPGA unit, was used to configure the FPGA [86]. This

---

[6] Red Pitaya STEMlab 125-14

allowed the module to be used as an arbitrary waveform generator (AWG), an oscilloscope, or as a proportional–integral–derivative (PID) controller. First, the cavity length is scanned across the resonance. To do this, the piezo chip is driven by a ramp waveform, generated by the FPGA and amplified externally by two amplifiers with gains of ×10 and ×20 before it is sent to the piezo [7]. The transmission is detected with a photodiode [8], and the output is sent to a transimpedance amplifier [9] before it is fed back to the oscilloscope module of the FPGA. A set point is then chosen on the side of the fringe to be used as a locking reference. Any deviation in the transmission from the setpoint will be translated into an error signal by the PID module of the FPGA, and a correction signal will be generated and fed back to the piezo chip to correct for the deviation. The PyRPL lockbox module used allows for complex functionality such as auto re-lock, which is rather useful when the cavity locking is lost, the piezo is then swept through its entire scan range, and if fringe is still within the scan range of the piezo, the cavity will be locked to the same reference point.

Apart from the cavity stabilization, the side-of-fringe scheme can also be used for vibration characterization. This is done by measuring the transmission over time by a photodiode while the cavity is locked. Applying a Fourier transform gives the vibration spectrum in units of voltage. This can be converted to units of length using voltage-to-length conversion factor calculated from the finesse, the maximum transmission of the cavity fringe, and the transmission at the reference point. First, the length-change linewidth is calculated from the finesse using Equation 5.2. The time trace of the scanned resonance is then fitted to a Lorentzian function, such as that shown in Figure 5.8, with the calculated length-change linewidth from the finesse. Assuming that the side of the resonance is well approximated by a straight line, the conversion factor can be calculated by taking the slope of the Lorentzian at the reference point. A more detailed discussion of the derivation of the conversion factor can be found in Ref. [82].

5.5 Scanning cavity microscopy

A fiber-based microcavity can be used for efficient optical imaging of nanostructures with significant signal enhancement compared to diffraction-limited microscopy [50]. Different methods of measuring extinction losses and the sizes of nanostructures using the cavity are discussed in Section 5.5.1. In order to calibrate the

---

[7] The first amplifier was a home-built operational amplifier, while the second was a TD250 6-Channel 250V amplifier from PiezoDrive (NSW, Australia)

[8] Hamamatsu photo-diode S5973

[9] FEMTO DHPCA-100 variable gain transimpedance amplifier

scanned areas, markers were machined on top of the substrate and imaged using the cavity. This is described in Section 5.5.2.

5.5.1 Extinction mapping

In order to find a "suitable" nanocrystal to characterize, scanning cavity microscopy (SCM) technique was used to identify areas with high extinction losses that could be attributed to nanocrystals [50]. The cavity length was continuously scanned across one fringe using the piezo chip. At the same time, the two horizontal positioners were used to raster scan an area of the sample the sample in the horizontal plane, while the z positioner was used to compensate for any slow drifts in the cavity length during the horizontal scan.

In Section 3.4.2, it was shown that the finesse is inversely proportional to the cavity losses. The presence of nanocrystals in the cavity contributes to these losses by scattering light out of the cavity. Consequently, changes in the finesse during the horizontal scan can be used to locate these nanocrystals. The cavity finesse can be written in terms of the different loss channels as:

$$F = \frac{2\pi}{T_1 + T_2 + A_1 + A_2 + 2B} = \frac{2\pi}{L_c + 2B} \tag{5.3}$$

where T1 and T2 are the transmission of the fiber mirror and substrate mirror, respectively, A1 and A2 denote the absorption of the two mirrors, B is the loss due to the crystal, which will mostly be scattering losses, and L_c is the total loss from the empty cavity, $L_c = T_1 + T_2 + A_1 + A_2$. Using the definition of finesse in Equation 3.36, and knowing that the FSR is independent of the losses, Equation 5.3 can be rewritten in terms of linewidth to give Equation 5.4 [50]:

$$\delta v = \frac{c(T_1 + T_2 + L_1 + L_2 + 2B)}{4\pi d} \tag{5.4}$$

Another way of monitoring the scattering losses due to the crystal is by measuring the maximum transmission of the cavity fringe. The transmission can be written as a function of the scattering losses [50]:

$$T_{max} = \epsilon \frac{4T_1T_2}{(T_1 + T_2 + L_1 + L_2 + 2B)^2} \tag{5.5}$$

where ϵ is the mode matching coefficient between the cavity mode and the fiber mode. Throughout this work, the maximum transmission was used to obtain extinction loss maps. Once B is known, the extinction cross section C_{ex}, which is the effective area of the nanocrystal that the beam should hit for scattering or absorption to take place, can be calculated from the expression:

$$C_{ex} = \frac{B\pi\omega_0^2}{4} \tag{5.6}$$

where ω_0 is the cavity mode waist. The extinction cross section can also be calculated theoretically using:

$$C_{ex} = (\frac{2\pi}{\lambda})^4 \frac{\alpha^2}{6\pi} \tag{5.7}$$

where α is the polarizability of the crystal, which can be calculated knowing the crystal volume, its permittivity and the permittivity of the surrounding medium using the Lorentz–Lorenz equation, which can be expressed in terms of the refractive indices [87]:

$$\alpha = 3\epsilon_0 V \frac{n_{nc}^2 - n_m^2}{n_{nc}^2 + 2n_m^2} \tag{5.8}$$

where ϵ is the dielectric constant of vacuum, V is the nanoparticle volume, and n_{nc} and n_m are the refractive indices of the nanoparticle and the surrounding medium respectively. Since the refractive indices of the nanocrystals and the surrounding medium are fixed, the crystal volume can be inferred by measuring the losses induced by its scattering of the light, which can be obtained by comparing the transmission with a nanocrystal in the cavity mode to that of an empty cavity.

5.5.2 Mirror markers

In order to perform SCM to identify a suitable nanocrystal, the area scanned must be known. This is possible if the steppers used for the raster scanning are calibrated. However, the steppers used in this work were open loop attocubes without feedback, and since they employ the slip stick mechanism, its motion is not very reproducible and depends highly on the initial conditions (load, friction, etc.). In order to calibrate the scanning area, a well-defined pattern was machined on top of the mirror using the same CO2 laser as that used for fiber profile machining. A graphical representation of the pattern created is shown in Figure 5.10 (a). The pattern consisted of a cross, dividing the scannable area into four quarters, each one containing a 4×4 checker-board pattern, as shown in the insert of Figure 5.10 (a). Each square of the checker-board is $\sim 50 \times 50$ μm, and can be identified by a letter and a number, making it possible to repeatedly identify the same area on the mirror. The whole pattern is located in an area 1.5 mm away from the edge of the mirror, which is within the area scannable by the fiber, and is repeated at three different locations. A wide-angle microscopic image of part of the pattern is shown in Figure 5.10 (b). The pattern created was then characterized by obtaining a white light interferometric images and deconvoluting the phase to reconstruct the structure. A top view of three machined points after reconstruction is shown in Figure 5.10 (c). The average spacing between the centers of two neighboring dots was ~ 10 μm

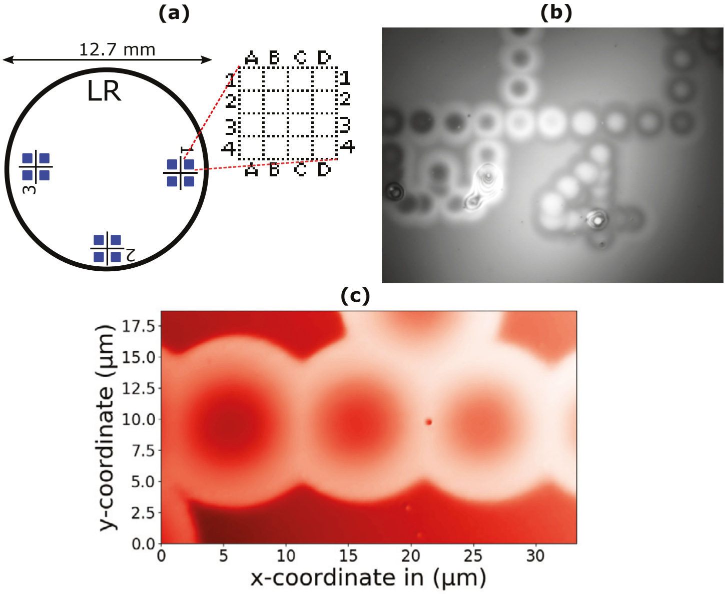

Figure 5.10: (a) Schematic of the machine checker-board patterns on the mirror, with an enlargement of one of the checker-boards (not-to-scale). (b) Wide-angle microscopic image of one corner of a checker-board. (c) Reconstruction of three machined points of the pattern from a white light interferometric image. Markers were machined by Timon Eichhorn

Once the scanned areas have been determined, the transmission method discussed in Section 5.5.1 can be used to perform SCM. The piezo is scanned across one cavity resonance, while the horizontal steppers are used to raster scan the sample. The changes in the shape and size of the resonance fringe are then used to determine the particle size, as explained above. Figure 5.11 shows a scan of a 100 $\times$ 60 μm area of two of the checker-boards before adding the nanocrystals. The bright spots, indicating higher transmission, indicate the checker-board formed by CO2 laser shots. The higher transmission is probably due to better angular alignment between the fiber and certain areas on the curved profiles machined on the mirror. The laser shot were also expected to melts the uppermost spacer layer of the coating leading to greater field penetration depth. During the raster scan, the ANPz attocube was used to compensate for drifts in the cavity resonance. This compensation is sometimes slower than the drift itself, and as a result, the fringe disappears from the scan range of the piezo chip (no transmission) for a few points before it is brought back by the ANPz attocube. This leads to some discrete glitches in the final image, as can be seen on the top part of Figure 5.11.

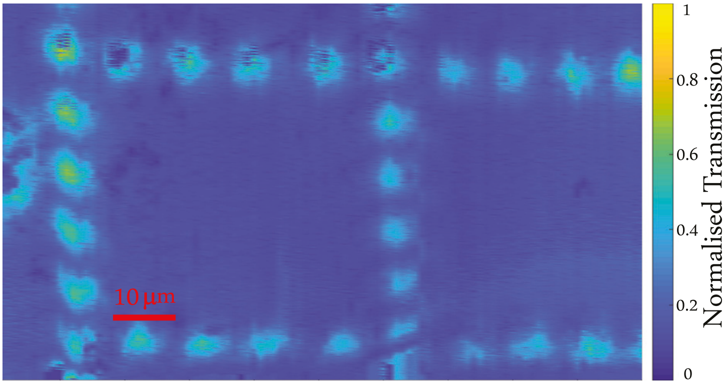

Figure 5.11: Scanning cavity microscopic (SCM) image of a 100 × 60 μm of an empty substrate taken by measuring the peak of the fringe as the mirror is raster scanned with respect to the fiber. The bright spots are the boundaries of the check-board.

5.6 Optical setup

The setup used in the cavity-based experiments is shown in Figure 5.12. The light emitted by the Ti:Sapphire laser passes into a double-pass acousto-optic modulator setup (AOM1). AOM1 is used to shape the optical pulses used in the experiments experiments, based on the radio frequency pulses generated by an AWG that drives the AOM. The light is then sent to the experimental table through a single mode optical fiber. The light emerging from the other end of the fiber passes through a second double-pass setup (AOM2), used to attenuate the light when aligning the single-photon avalanche detector (SPAD), and for gating of any light leaking through AOM1, preventing it from reaching and saturating the SPAD when it is on. The light is then coupled to a 2×2 fiber splitter. 10% of the light is coupled into the cavity fiber through a mating sleeve, while 90% is dumped in a terminator. The cavity fiber is then inserted into the cryostat and sealed using the configuration shown in Figure 5.13. The signal transmitted through the cavity is collected outside the cryostat window and directed to either a spectrometer or a photodiode. The photodiode output is amplified using a transimpedance amplifier before being sent into the FPGA. The FPGA was used as a signal generator to drive the piezo chip, as an oscilloscope to view the transmission photodiode output, and as a lockbox as discussed above. The light emitted by the ions into the cavity mode couples into the cavity fiber, which guides it outside the cryostat. 90% of the light is directed into one arm of the fiber splitter, from which it is sent to the detection setup. The light in the detection setup is passed into a gating single-pass AOM3 to prevent the excitation light from

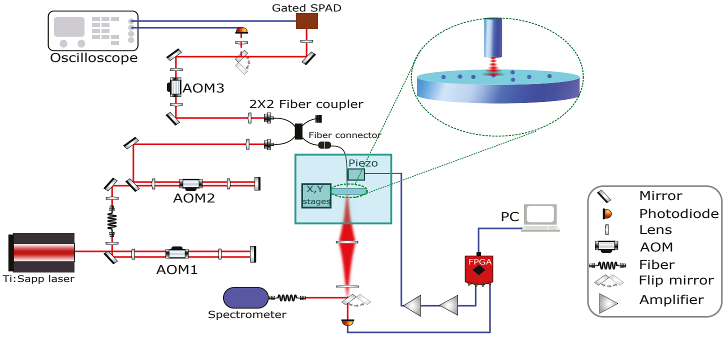

Figure 5.12: Experimental setup of the Ti:Sapphire laser used for pulse shaping and fluorescence detection.

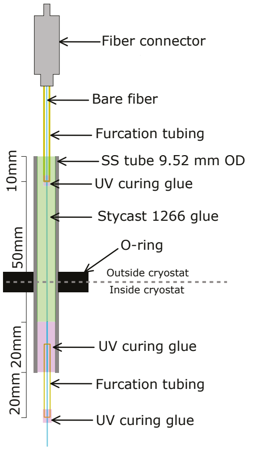

Figure 5.13. *Schematic showing the method used to introduce the fiber into the cryostat while preserving the vacuum seal. The Stycast glue forms a seal around the bare fiber, and the O-ring forms a sealing around the outer wall of the stainless steel tube.*

reaching the SPAD. The output of AOM3 is then directed and focused into the gated SPAD. A flip mirror is also used to provide the option of monitoring the cavity reflection using a photodiode. A transimpedance amplifier is also used here to amplify the output of the photodiode. The reflection photodiode is used to calibrate the number of photons for initial alignment of the SPAD.

Fiber cryogenic sealing

In order to introduce the fiber into the cryostat without breaking the vacuum seal, the setup shown in Figure 5.13 was used. An 80 mm long stainless steel tube with a 9.52 mm outer diameter and 0.2 mm wall thickness, through which the bare fiber passes, was filled with Stycast 1266 epoxy to form a seal around the bare fiber. As the cryostat cools down, the glue tends to shrink away from the tube wall. The thin wall ensures that the stainless steel can flex maintaining the vacuum seal. Vacuum sealing was achieved around the outer wall of the tube using an O-ring.

5.7 Room temperature measurements

This Section describes the room temperature characterization of the cavity and the samples prepared on the cavity mirror. It also summarizes room temperature spectroscopic measurements performed on the nanocrystals in the cavity.

5.7.1 Cavity characterization

The length of the cavity is measured by coupling a broad white-light source into the cavity and measuring the transmission using a broadband spectrometer. The cavity length is then obtained by measuring the FSR and using Equation 3.33. Figure 5.14 shows the transmission spectrum measured when coupling white light into the cavity, and a length of 4.16 μ m was inferred from the 95.11 nm FSR.

Although the minimum cavity length is theoretically $\frac{\lambda}{2}$, the minimum cavity length obtained in these experiments was $\sim 3.5\mu$m. There are several reasons for this. The fiber mirror is concave and has a depth of ~ 1 μm, which forms a physical limitation on the minimum separation between the two mirrors. Imperfections on the fiber end-facet created while shooting the mirror profiles could also contribute to this limitation. Finally, if the fiber and the mirror are not perfectly aligned, which usually is the case, this will also limit the minimum achievable cavity length.

To measure the finesse, the piezo chip was scanned across two or more resonances, by driving it with ± 200 V, corresponding to a displacement of ~ 1 μm. Figure 5.15 shows a length scan of 800 nm obtained for a cavity with a mirror reflectivity of 99.5% for both the fiber and the mirror.

The side-of-fringe locking scheme was used to characterize the stability of the cavity as discussed above. The piezo is scanned across one fringe, a reference point on the side of the fringe with some transmission level is chosen as a lock point, and locking was engaged as discussed in Section 5.4. The fluctuations in the transmission detected in voltage is then converted to nm using the conversion steps discussed above. The measured vibration spectrum can be seen in figure x, with the time length fluctuations shown in figure xb.

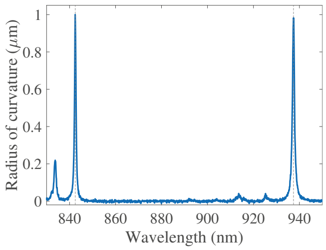

Figure 5.14. *FSR measurement. Transmission spectrum from the cavity when coupling white light in. The FSR is $\sim$ 95.11 nm, corresponding to a cavity length of $\sim$ 4.16 μ m.*

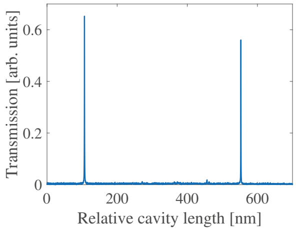

Figure 5.15. *Finesse measurement by scanning the cavity length across two fringes. The finesse measured here was 700.*

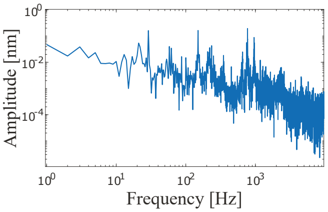

Figure 5.16. *Vibration spectrum measured with side-of-fringe lock for a cavity with 700 finesse. Measurement performed at room temperature, with the fiber tip touching the mirror to increase the stability.*

5.7.2 Sample preparation and characterisation

Two Y_2O_3 nanocrystal samples were synthesized by the group of Professor Philippe Goldner at CNRS, Paris, these will be referred to as F4 and F5. Sample F4 was co-doped with 100-ppm of Nd^{3+} and Pr^{3+} , and had an average nanocrystal size of 180 nm, as shown in Figure 5.18 (a). Sample F5 had the same doping of Nd^{3+} , but 200-ppm of Pr^{3+} , and had an average nanocrystal size of 250 nm, as shown in Figure 5.18 (b). The nanocrystals used for the cavity experiments are from the F4 sample. Two different methods were used to deposit nanocrystals on top of the mirror. In the first, the nanocrystals were mixed in a Poly-methyl methacrylate (PMMA) matrix, which was spin coated on the surface of the mirror. This has the advantage of reducing the scattering losses since the refractive index of PMMA is 1.48, while that of the Y_2O_3 nanocrystals is 1.87 at 900 nm [88, 89]. Figure 5.17 shows the expected scattering losses at different crystal sizes, with and without PMMA coating. The disadvantage of PMMA is that it leaves some traces on the fiber mirror when the fiber touches the mirror (which happens often). This deteriorates the fiber coating and eventually damages it.

It was difficult to observe any fluorescence from samples prepared using this method with the cavity setup.

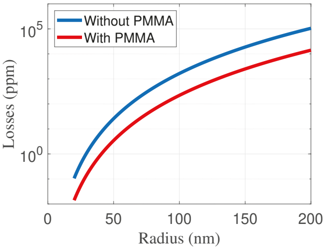

Figure 5.17. *Expected scattering losses vs particle size with (red) and without (blue) PMMA surrounding the crystals.*

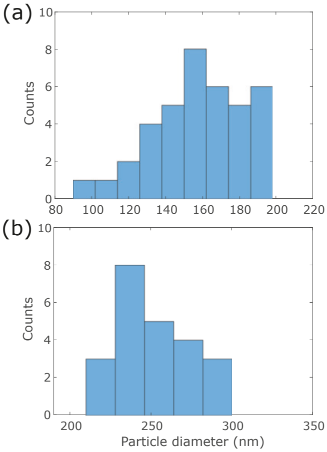

Figure 5.18. *Nanoparicles size distribution from a scanning electron microscopy (SEM) image of (a) sample F4, with* Pr^{3+}-Nd^{3+}:Y_2O_3 *nanocrystals with an average radius of* ~ *80 nm, and (b) sample F5 with an average crystal radius of 125. Measurement performed by Diana Serrano at CNRS, Paris.*

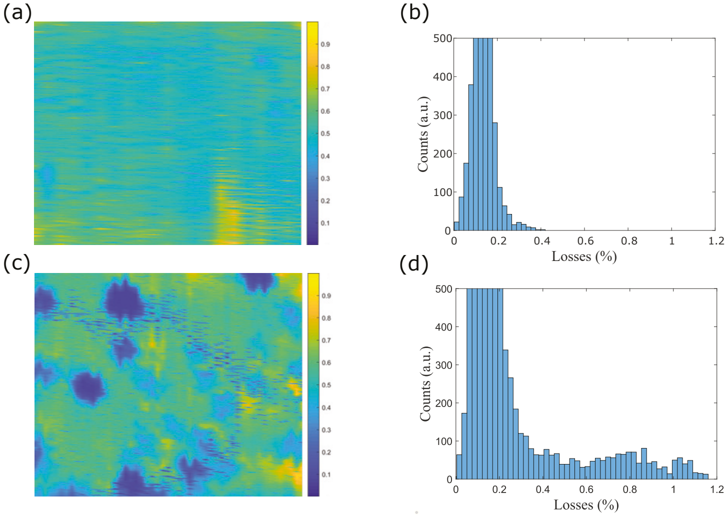

Figure 5.19: Sample characterization using scattering losses in a cavity with 800 finesse. (a) Scan of an area of $\sim 40\mu m^2$ for a clean mirror before adding the sample. (b) A histogram showing the extinction losses at each point of the scan (a); the cavity resolution is limited to 0.2% (corresponding to particle radius of 100 nm). This is due to the relatively low finesse of the cavity, fringe drifts during the scan, and power fluctuations. (c) Scan of an area of $\sim 40\mu m^2$ after adding the nanoparticles by drop-casting. (d) Histogram of extinction losses of scan (c)

In the other method used to prepare the samples, the nanocrystals were mixed in a high purity (99.9%) ethanol solution and treated in an ultrasonic bath for ~ 15 minutes in order to break aggregates. The mixture was then deposited on the surface of the mirror by drop-casting while the mirror was inside a dry ultrasonic machine to evenly distribute the nanocrystals across the surface and break aggregates during drop casting. The samples discussed in the next Sections were prepared using this method.

The SCM technique discussed in Section 5.5 was then used to characterize the quality of the deposited sample. The measured finesse of the empty cavity used here was about 800. Figure 5.19 shows two transmission scans at different locations before and after adding the nanocrystals. The histograms in Figures 5.19 (b) and (d) show the extinction losses at each point of the scans in the empty and the loaded cavities, respectively. At this level of finesse, and within the fringe stability, the resolution was limited to 0.2% extinction, corresponding to a particle radius of 100 nm, as shown in Figure 5.20. From the histogram and Figure 5.20, particle radii ranging from 100 nm to 150 nm can be seen (excluding the unresolved < 100 nm radii particles). This is still withing the size distribution obtained from the scanning electron microscopy (SEM) image, shown in Figure 5.18, but also indicates particle aggregation.

For cavity enhancement and fluorescence detection experiments, the particle size should be large enough to provide enough ion ensembles, but small enough to maintain high finesse and good out-coupling efficiency. Once a suitable nanocrystal has been identified, the next step is to run the experimental pulse sequence while locking is engaged. In this case, the same laser was used for both locking and excitation. In order to enable that, the pulse sequence consisted of a 10 ms long pulse at a shifted central frequency f_0+10 MHz from the excitation frequency, which was for locking. This pulse is followed by a separate 10 μs long excitation pulse at frequency f_0. The reason for the frequency shift in the locking pulse is to avoid any effect from it on the targeted ions, such as hole burning, this is only relevant for cryogenic measurements. The fluorescence detection window is an interval of a few ms after the excitation pulse. This sequence can be repeated many times to collect more fluorescence.

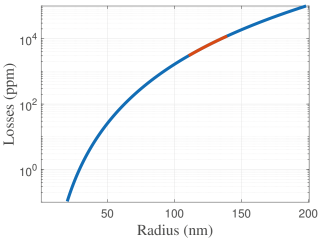

Figure 5.20. *Nanoparticle size vs scattering losses for Y_2O_3 at a wavelength of 892 nm. The orange segment of the curve represents the resolved crystal size distribution for the sample shown in Figure 5.19. Smaller crystals may exist, but can not be resolved using transmission losses at this finesse.*

5.7.3 Fluorescence detection

In order to enable fluorescence detection, the following procedures were followed:

- The cavity finesse was measured on an empty spot, with a continuous wave (cw) light as cavity input.
- SCM was performed on an area of $\sim 50 \times 50 \mu m$ to help find a suitable nanocrystal to study.
- After deciding which nanocrystal to investigate, the horizontal scanner were used to move to the nanocrystal location. It is advisable to perform another smaller scan across the nanocrystal to confirm it is the desired one.
- The finesse was measured at the nanocrystal's location, as well as the cavity length, in order to estimate the Purcell factor later.
- The pulse sequence was then used, and a set point was chosen (This depends on how stable the cavity is, higher stability allows for a higher set point). Side-of-fringe locking was then activated.
- Finally, data acquisition was started.

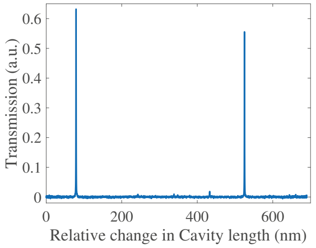

Figure 5.21. *Finesse* $\sim$ *800 measured on a clean mirror before adding nanoparticles.*

The cavity used for fluorescence detection experiments is asymmetric, and consisted of a fiber mirror with 99.5% reflectivity, and a substrate with 99.9% reflectivity. Figure 5.21 shows the finesse measured for an empty cavity before adding the nanocrystals. A finesse of 800 was measured, which is less than the value of 1000 expected from from the coating shown in Figure 5.6. The discrepancy is an indication of additional losses (apart from the expected 0.06% transmission from the mirrors), which could be due to scattering by the mirrors, absorption, or other undesired scatterers on the mirror. The total losses for the empty cavity (L_c) were estimated from Equation 5.3 to be 0.79%.

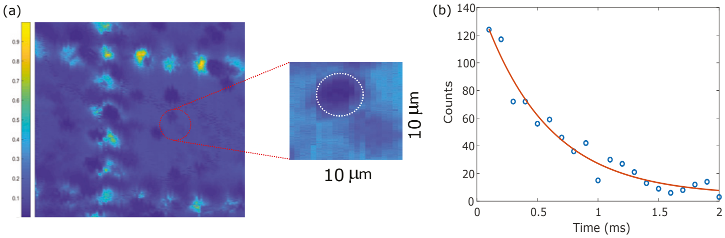

Figure 5.22: (a) is a SCM image of an area of 70 × 70 μm after adding the nanocrystals to the surface of the mirror by drop-casting. A finer scan of a smaller area containing an isolated crystal is shown in the insert. (b) Binned fluorescence counts (blue) detected during 2 ms after excitation and accumulated from 10^4 shots. The orange curve is a single exponential fit to the data giving a lifetime of 547 μs

Figure 5.22 (a) shows a scan of a $\sim$ 70 × 70 μm area after adding the nanocrystal sample to the surface of the mirror by drop-casting. The insert shows a finer scan of the area indicated by the red circle in 5.22 (a), which shows three isolated particles. The nanocrystal indicated by the white circle in the enlargement scan was chosen for measurements. The size of the particle was estimated using two different methods. A direct finesse measurement was made at the particle location (shown in Figure 5.23), revealing a finesse of $\sim$ 300. Using Equation 5.3, this corresponds to scattering losses of 1.3% from the nanocrystal, indicating a radius of 140 nm, which is still within the size distribution of the particles measured in this sample as shown in Figure 5.19. In addition, the transmission method discussed in Section 5.5.1 was also used to verify the size estimation. The transmission at the particle location was $\sim$ 8% of the maximum transmission. Using Equation 5.5 gives a $\sim$ 1% scattering loss for this level of transmission, corresponding to a particle radius of 136 nm, which is in good agreement with the previous estimate. With 100 ppm Nd^{3+}

doping concentration, the number of Nd^{3+} ions in a single crystal with a radius of 140 nm can be estimated to be $\sim 3 \times 10^4$ ions. Using the pulse sequence described above, with side of fringe locking engaged, it was possible to detect Nd^{3+} fluorescence at 892 nm from the particle scanned in Figure 5.22 (a) at room temperature. The fluorescence accumulated from 10^4 shots over a period of 2 ms after excitation is shown in Figure 5.22 (b). An exponential fit gave a lifetime of 547 μs, which is similar to the Nd^{3+} lifetime measured in free space, as discussed in Section 4.2.3. In order to estimate the number of ions that were excited, it was assumed that all the excited ions had decayed by the end of the detection time. The total number of counts after subtracting dark count for 10^4 shots, is ~ 800. The number of excited Nd^{3+} ions can be estimated using:

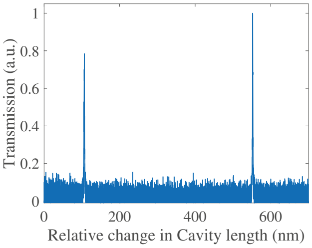

Figure 5.23. *Finesse of $\sim$ 300 measured at the particle location indicated by the white circle in Figure5.22 (a).*

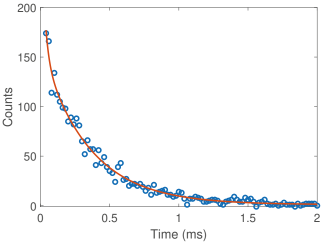

Figure 5.24. *Room temperature measurement of fluorescence from a different nanocrystal where the extinction losses were 0.1%, indicating a particle radius of 90 nm.*

$$\text{No. of excited } \mathrm{Nd}^{3+} \text{ ions} = \frac{\frac{\text{Counts}}{\text{No. of shots}}}{\mathrm{B} \times \eta} \tag{5.9}$$

where B denotes the branching ratio, and is 23% for the ZPL $^4\mathrm{F}_{3/2}(Y_1) - {}^4\mathrm{I}_{9/2}(Z_1)$ transition at 892 nm, as discussed in Section 4.2.1. The detection efficiency, η, is 1.2% (including 20% optical efficiency, 40% quantum efficiency of the SPAD, 15% out-coupling efficiency). The number of Nd^{3+} ions contributing to the signal was thus deduced to be ~ 30 ions. This is significantly less than the 3×10^4 ions available in a 140 nm radius nanoparticles. Several factors could have contributed to this discrepancy: the particle size could have been overestimated. This is possible if the observed transmission losses (and the lower finesse) were due not only to the particle, but also to some contamination on the substrate close to the particle. This would lead to an overestimation of the particle size, and reduce the collection efficiency. Secondly, in order to avoid saturation of the detector, there is a waiting time of 15 μs after excitation before detection is started. The counts during this period are not measured, which means the actual signal emitted by the ions is underestimated.

In order to mitigate the first factor, the fluorescence of different nanocrystal was measured. Figure 5.24 shows the fluorescence measured from this nanoparticle, where the extinction losses were $\sim 0.1\%$, corresponding to a particle radius of ~ 90 nm. The total number of counts accumulated from 500 shots was 2770, which, according to Equation 5.9, means that ~ 2000 ions contributed to the signal. With a 50% excitation probability at saturation intensity, this means that about 13% of the $\sim 3 \times 10^4$ ions available in the crystal were excited. Since some counts are lost during the 15 μs waiting time between excitation and detection, the actual number of excited ions should be even higher than that estimated here. The collected fluorescence of this nanocrystal decays much faster during the first 100 μs of the detection time. A double

exponential fit to the data gave two decay rates, corresponding to $T_{fast} = 26\ \mu s \pm 20\ \mu s$, and $T_{slow} = 343\ \mu s \pm 31\ \mu s$. Similar multiple decay rates have been reported for Er^3+ cavity-enhanced emission, and the observation was attributed to contributions from emitters experiencing different degrees of enhancement depending on their position with respect to the electric field ($P \propto |E|^2$) [90]. The obtained decay rates indicate Purcell factors of 20 ± 9 for the strongly enhanced ions, and 1.57 ± 0.13 for the majority of the ions, which are weakely enhanced.
As mentioned above, in order to avoid saturation effects, and to make sure that all counts at the beginning were contributions from the ions, the SPAD was activated 15 μs after the excitation pulse [10]. The data lost during the 15 μs waiting time at the beginning could explain the large error in the fast decaying component.

A transmission loss of 0.1% corresponds to a finesse of $\sim$ 700. For a cavity with this finesse, a length of 3 μm, and with a fiber mirror with ROC = 20 μm, the expected effective Purcell factor would be $\sim$ 12, which is less than that measured for the fast decaying ions above, but still within uncertainty of the fit. The finesse used to estimate the Purcell factor was estimated from the total losses, which only provides an approximate estimate of the real finesse. The real design finesse could reach as high as 1000 without losses. If the real finesse at the particle location was underestimated, then the estimated Purcell factor could be closer to that measured for the fast-decaying ions.

5.8 Cryogenic measurements

Fluorescence measurements of nanocrystals in the microcavity were then performed at cryogenic temperatures. When the cavity is cooled from room temperature to 2.1 K, the length of the cavity and the relative position of the fiber with respect to the mirror will change rapidly due to thermal contraction of the cavity components. This makes it difficult to maintain the room temperature optimization. When the cavity reaches the base temperature of 2.1 K, the scan range of the shear piezo becomes limited to a few nm, which makes it difficult to obtain maps of the nanocrystals similar to those obtained at room temperature. Instead, the horizontal positioners were stepped manually to find areas that

---

[10] According to the SPAD manufacturer, LaserComponents, even when the SPAD is not triggered, the incident light can create electron-hole pairs. However, they will not be accelerated due to the absence of a reverse-biased voltage. As soon as the reverse-biased voltage is applied, the remaining pairs from the "inactive detector" stage will be accelerated together with the the ones created by the incoming photons from the experiment. In the extreme case, with a lot of light while the SPAD is triggered off, the SPAD can be damaged. But in an usual case (low light levels), electron-hole pairs created while the SPAD is inactive will either not be accelerated at all, or will be partially accelerated, giving rise to a very short high signal during the first few nanoseconds.

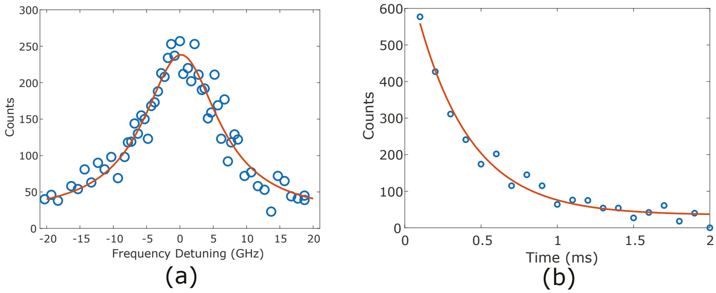

(a) (b)

Figure 5.25: (a) Inharmonious line of the $^4F_{3/2} - {}^4I_{9/2}$ measured at 2.17 K: (Blue) Counts collected during 200 μs after excitation and accumelated from 10^4 shots, (Red) is a Lorentzian fit with 13.74 GHz FWHM linewidth. (b) Binned Fluorescence counts (blue) detected during 2 ms after excitation and accumulated from 10^5 shots, and a single exponential fit (red) with a lifetime of 354 μs

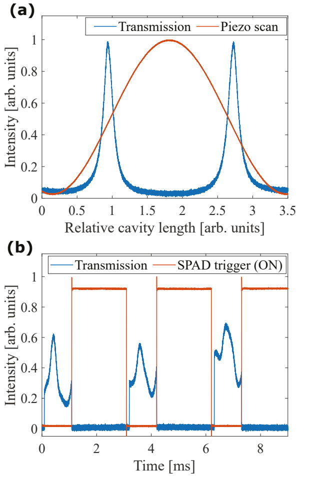

Figure 5.26. *(a) A piezo scan (red) back and forth a cross a cavity resonance (blue). (b) Pulse sequence used for fluorescence measurement consisting of 1 ms long excitation pulse followed by 2 ms detection time. Blue is the transmitted normalised to the fringe peak in (a), Red is the SPAD trigger (detection time). The input pulses used are uniform square pulses, but the blue trace is not due to cavity length fluctuations*

showed a decrease in transmission, indicating a higher probability of nanocrystals. Figure 5.26 (a) shows a scan of cavity length across a resonance back and forth, where it can be seen that the range of the scan has decreased significantly.

The pulse sequence used for the fluorescence measurements is shown in Figure 5.26 (b), consisting of a 1 ms excitation pulse followed by a 2 ms long detection window. Due to the limited scan range of the piezo chip, no locking was used here. However, once at 2.1 K, the passive stability of the cavity improved considerably, and an offset DC voltage was applied to the piezo chip to compensate for slow drifts in cavity length. The Intensity of the pulses shown in Figure 5.26 (b) was normalised to the maximum of the resonance shown in Figure 5.26 (a). From the figure, it can be seen that the cavity length fluctuates around 0.5 of the maximum of the resonance.

Measuring the inhomogeneous linewidth would give some indication of the crystal quality. The inhomogeneous linewidth was measured by collecting data for the first 200 μs after the excitation pulse and accumulating fluorescence counts from 20000 shots. The laser wavelength was scanned across the inhomogeneous line, and the measured spectrum is shown in Figure 5.25 (a). A FWHM linewidth of 13.74 GHz was obtained by fitting the data to a Lorentzian. This is close to what was measured in nanocrystals with 380 nm diameter discussed in Chapter 4.

Figure 5.25 (b) shows a fluorescence spectrum of Nd^{3+} at 2.1 K after subtracting the dark counts. The data were fitted with a single exponential, giving a lifetime of 354 μs ± 60 μs, which is slightly shorter than the 540 μs measured in the nanocrystals discussed in Chapter 4, indicating some degree of enhancement.

5.8.1 Estimating the number of ions

The number of ions can be estimated in two ways: one based on the total number of photons collected (indicated the number of excited ions), and the other on the particle size, doping concentration, homogeneous and inhomogeneous linewidth, and the excitation power (indicating the number of targeted ions).

The number of excited ions was first estimated from the total number of photons collected after excitation. The sum of the counts shown in Figure 5.25 (d), after subtracting the dark count, was 2818, accumulated from 10^5 shots. Assuming that all the excited ions would have decayed during the 2 ms detection time, Equation 5.9 can be used to estimate the number of ions contributing to the signal, resulting in $\sim$ 10 ions.

In order to estimate the number of targeted ions using the second method, we assumed a nanocrystal radius of 140 nm, which is the largest size measured on this sample (see Figure 5.19). Such a particle would have a total of $\sim 3 \times 10^4$ Nd^{3+} ions. With a homogeneous linewidth of 100 kHz (measured for larger nanocrystals as discussed in Section 4.2.4), and an inhomogeneous linewidth pf Γ_{inh} = 13.74 GHz, we estimated 0.21 ions per frequency channel, which means that the ions are spectrally separated by about 4.7 linewidths, which makes it unlikely that a single ion can be addressed at such low level of excitation power.

For these experiments, the cavity input was $\sim$ 100 nW, this is amplified by a factor of $\frac{\mathcal{F}}{\pi}$. For a 140 nm particle radius, the scattering losses are $\sim$ 1.25%, which corresponds to a finesse of $\sim$ 300. The power inside the cavity was thus estimated to be $\sim$ 10 μW, which is much higher than that needed for saturation excitation. In order to estimate the power broadening, the following equation was used [24]:

$$FWHM = \sqrt{\Gamma^2 + 2\Omega_R^2} \tag{5.10}$$

where Γ is the transition linewidth ($1/T_1$), and Ω is the Rabi frequency, which can be calculated if the electric field of the excitation pulse and the transition dipole moment, μ, are known[91]:

$$\Omega_R = \frac{\mu E}{\hbar} \tag{5.11}$$

Equation 5.12 was the used to calculate μ [91]:

$$\mu = \sqrt{\frac{3g_1}{2g_2} \frac{\hbar e^2}{m_e \omega_{21}} f_{12}} \tag{5.12}$$

where g_1 and g_2 are the degeneracy factors of the ground and the excited levels, respectively, ($g_1 = g_2 = 2$), ω_{21} is the angular frequency between the two levels, m_e is the electron mass, and f_{12} is the oscillator strength, which is 1.4×10^{-6} for the $^4F_{3/2}$ −

^{4}I$_{9/2}$ transition [92]. This gives a value of $\mu = 5.48 \times 10^{-32}$ C·m. Using Equation 5.11, gives a Rabi frequency of $\Omega_R = 14$ MHz. The power broadening thus can be calculated using Equation 5.10, giving a broadening of $\sim$ 20 MHz, which means that the total number of targeted ions is $\sim$ 35. Given the uncertainties in the various estimates, this is in good agreement with the measured value. This indicates that at this level of finesse, we are in the few-ion regime. By reducing the power broadening from 20 MHz to 0.5 MHz, it would be possible to target a single ion, on average. This can be done using 1 nW of power as the cavity input.

In order to estimate the Purcell factor, the 540 μs lifetime measured at room temperature for slightly larger nanocrystals can be used as a reference. This gives an estimate of an effective Purcell factor P$_{eff} = \frac{540\,\mu s}{354\,\mu s} \sim 1.54$.

The effective Purcell factor can also be calculated using Equation 3.43. The finesse used was $\sim$ 300, and the cavity length was 5 λ, which gives a value of P$_{eff}$ of 3.2, which is a factor of 2 higher than the measured value.

Although the cavity linewidth ($\sim$ 1.5 nm) and the ^{4}F$_{3/2}(Y_1)$ – ^{4}I$_{9/2}(Z_1)$ transition linewidth ($\sim$ 1.2 nm [93]) are comparable, the two lines do not completely overlap as the cavity set point is $\sim$ 50% of the fringe peak as shown in Figure 5.26 (b). This could reduce the calculated Purcell factor. Similarly, different emitters couple differently to the cavity mode depending on the dipole moment orientation, and this could also reduce the expected effective Purcell factor.

5.9 Outlook

An ensemble of Nd^{3+} ions has been detected using low finesse cavity enhancement at cryogenic temperature. Some improvements could be made that may allow single-ions detection. First, using a piezo chip with longer scan range at cryogenic temperature would be beneficial. It would then be possible to scan an FSR and measure the finesse more precisely, which is necessary to obtain an accurate estimate of the Purcell factor. A longer scan range would also allow larger areas to be scanned so that extinction maps could be obtained without 'losing' the fringe. This will be useful in more accurately identifying a crystal with a suitable size on which to perform measurements, as was done at room temperature.

A higher finesse would also be the natural next step. A finesse of 4000 has recently been measured a fiber reflectivity of 99.9% and a mirror reflectivity of 99.95%. With such a finesse, nanocrystals with a radius of 80 nm would easily be resolved, and an effective Purcell factor > 30 could be achieved, paving the way for single-ion detection. Once this is achieved, the dipole-dipole interaction between the Nd^{3+} and Pr^{3+} ions can be measured. This will be

useful in assessing how close we are to realizing a high fidelity readout of the Pr^{3+} qubit state using dipole-blockade mechanism discussed in Section 4.1.
Recently, a single crystalline membrane of YSO doped with 0.01% Nd^{3+} was bonded to a mirror with reflectively of 99.9% by Roman Kolesov (Stuttgart, Germany). The membrane was $\sim 10\ \mu$m thick, making it suitable for studies on ion ensembles. It would be interesting to characterize this material using the cavity discussed above, both as a test of this new method of sample preparation, and to characterize the properties of Nd^{3+} in the membrane YSO host.

Chapter 6

Quantum Storage in Rare-Earth Ions

This chapter provides an overview of Quantum memories and their use in quantum communication. This is followed by more specific discussions on the AFC and the spin-wave schemes. Static dipole moment and Stark shift in REIs (Pr) is then discussed. It is then explained how a Stark shift is combined with the AFC and a spin-wave schemes to provide another tool to control those schemes.

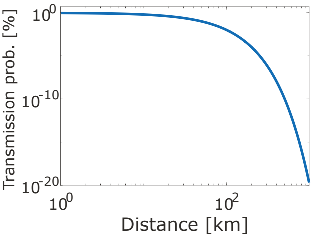

Figure 6.1. *Transmission probability as a function of distance for photons transmitted through a telecom fiber with 0.2 dB/km attenuation.*

6.1 Quantum memory for quantum repeaters

The distribution of quantum resources such as quantum entanglement over long distances is essential for quantum key distribution in quantum communication. The most common way to achieve such a distribution is to transmit the entangled quantum states, encoded on photons, through optical fibers. While this can be done for quantum state distributions over finite distances, it becomes impractical for distances exceeding a few hundred kilometers due to optical losses in the transmission channel. Figure 6.1 shows the decrease in transmission probability with distance for transmission through a telecom optical fiber with typical attenuation loss of 0.2dB/km. For classical communication, this problem can be solved by introducing classical repeaters along the communication path that amplify the transmitted signal at regular distances and resend it to the next repeater. However, this cannot be done in the case of quantum states since the no-cloning theorem forbids such operations [94]. A quantum repeater can be used to extend the communication distance without destroying the transmitted quantum states [14]. The principle of a quantum repeater is shown in Figure 6.2. It consists of two distant entangled pair sources, EPS1 and EPS2, each generate an independent pair of entangled photons

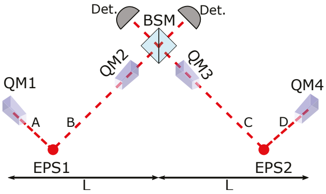

Figure 6.2. *Schematic showing the principle of a quantum repeater. Two pairs of entangled photons (A,B) and (C,D) are generated by the entangled pair sources EPS1 and EPS2, respectively. One photon of each pair (B,C) is sent towards an intermediate station where they are synchronized using quantum memories QM2 and QM3, while the other pair (A,B) is sent for storage in QM1 and QM4, respectively. A Bell state measurement (BSM) of the (B,C) pair swaps the entanglement, leading to an entanglement generated between the distant pair (A,C).*

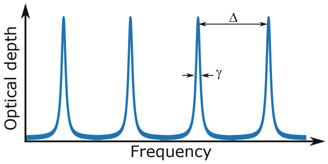

Figure 6.3. *Typical AFC absorption structure*

(A,B) and (C,D), respectively. One photon from each entangled pair, B and C, is sent towards an intermediate setup, while the two remaining photons, A and D, are stored in quantum memories QM1 and QM4, respectively. Quantum memories QM2 and QM3 are used to synchronize photons B and C by storing the first photon to arrive until the other one is ready. By performing a Bell-state measurement (BSM) on the (B,C) pair, in which they are projected onto one of the four Bell states, the two photons (A,D), stored in QM1 and QM4, become entangled, which leads to a distribution of the entangled states over a longer distance of 2L. This can be repeated with additional pairs of entangled photon and BSM to further increase the distance of the entanglement distribution. On-demand quantum memories are critical in quantum repeaters as they allows the signals arriving from different EPSs to be synchronized.

The performance of a quantum memory is characterized by it storage efficiency, fidelity, bandwidth, storage time, multi-mode capacity and the noise performance at the single photon level [11]. Several schemes have been proposed and investigated to realize an optical quantum memory. These include electromagnetically induced transparency (EIT) [95], gradient echo memories/controlled-reversible inhomogeneous broadening (GEM/CRIB) [96, 97], revival of silenced echo (ROSE) [98], hybrid photon-echo rephasing (HYPER) [99], and atomic frequency comb [19, 100, 101]. A comprehensive overview of the different schemes can be found in Ref. [11]. The work described in this thesis was based on the AFC scheme.

6.2 Atomic frequency comb

The AFC scheme was first proposed by Afzelius *et al.* [102, 103] in 2009. Since then, several experimental realizations of the AFC scheme have been reported for both classical light storage [104–106] and single-photon storage [20, 107, 108]. In the AFC scheme, the absorption profile of an inhomogeneously broadened optical transition $|g\rangle \to |e\rangle$ in an atomic ensemble is spectrally tailored by optical pumping to produce a comb-like structure, as shown in Figure 6.3. The AFC can be characterized by the peak width γ, and the frequency spacing between two neighboring peaks Δ. The finesse of an AFC (F) is defined as $F = \frac{\Delta}{\gamma}$. A photon with a bandwidth overlapped by the FWHM of the AFC is stored as a single excitation delocalized over all resonant atoms in the ensemble. This collective state can be expressed as [100]:

.

$$|\psi\rangle = \sum_{j=1}^{N} c_j e^{2\pi i \delta_j t} e^{-ikz_j} |g_1 ... e_j ... g_N\rangle\,, \tag{6.1}$$

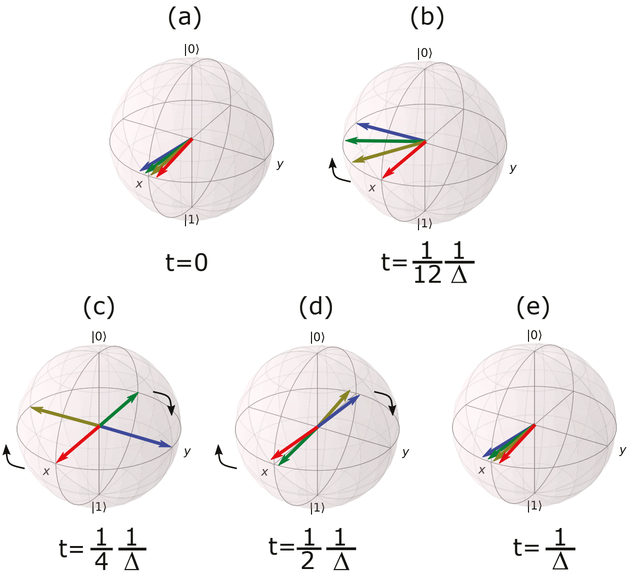

Figure 6.4: Phase evolution of the AFC peaks in a Bloch sphere at different times indicated under each sphere. The arrows different colors represent the ions in the different peaks in the AFC

where N is the number of atoms in the AFC, $|g_j\rangle$ and $|e_j\rangle$ are the ground state and the excited state, respectively, c_j is the probability amplitude that the input photon excites ion j, δ_j is the frequency detuning of ion j from the AFC peak center frequency ω_c, z_j is the spatial position of ion j, and k is the photon wave vector. Figure 6.4 shows the phase evolution of the collective excitation in a Bloch sphere. The photon storage can be summarized in the following steps.

- Before excitation, all atoms are in the ground state.
- At t=0, just after the photon has been absorbed by the collective atomic ensemble, the collective atomic excitation will be in a superposition state as shown in Figure 6.4 (a), and all the individual atom wave functions will be in phase.
- In the time interval $0 < t < \frac{1}{\Delta}$, each term in the superposition will acquire a phase $e^{i\delta_j t}$ depending on its detuning from the AFC peak center frequency ω_c, due the inhomogeneous distribution of its resonance frequency. Figures 6.4 (b,c) show the phase evolution of the atomic ensemble.
- At t $= \frac{1}{\Delta}$, thanks to the periodic AFC peak separation Δ, the atomic ensemble re-phase and the collective excitation

> state is restored, leading to re-emission of the stored photon as a coherent photon echo.

One of the features of the AFC storage scheme is its large bandwidth, despite the fact that its peaks are spectrally localized. This can be explained by the Heisenberg time-energy uncertainty principle. Consider an input pulse with a duration tau_p and a spectral distribution $\gamma_p = \frac{1}{\tau_p}$ that is larger than the peak separation Δ, but narrower than the total width of the AFC. For the time scale of the absorption of this pulse, which is set by its duration, the uncertainty of the optical transition will be on the order of the γ_p. Effectively, this leads to a spectral averaging of the narrow AFC peaks onto a uniform distribution across the input pulse bandwidth [100]. For an AFC echo emitted in the forward direction, the efficiency is limited by echo re-absorption. The maximum efficiency in this case is 54%. The storage efficiency for an echo emitted in the forward direction is given by [100]:

$$\eta_f = (\tilde{\alpha}L)^2 e^{-\tilde{\alpha}L} e^{-\frac{7}{F^2}} \tag{6.2}$$

where $\tilde{\alpha}$ is the effective absorption of the comb defined as $\tilde{\alpha} = \frac{\alpha}{F}\sqrt{\frac{\pi}{4\ln(2)}}$ with α being the absorption of the comb peaks, and L is the sample length. The storage efficiency can exceed this 54% limit by applying two counter-propagating control fields for phase matching, which forces the echo to propagate in the backward direction. The efficiency of the AFC in this case depends on two factors: the probability of absorption of the input field, which is higher for lower AFC finesse, and on the dephasing of the ensemble, which is reduced for higher finesse. For the backward propagation, the retrieval efficiency is written as [100]:

$$\eta_b = (1 - e^{-\tilde{\alpha}L})^2 e^{-\frac{7}{F^2}} \tag{6.3}$$

The storage time in this protocol is determined by the structure of the AFC and is given by $\frac{1}{\Delta}$. Longer storage times can be achieved by transferring the collective excitation into a long-lived spin level ,$|s\rangle$, in the ground hyperfine state, which has a long coherence lifetime compared to the optical coherence lifetime. The optical phase evolution freezes during spin storage. This transfer to the spin state can be achieved by applying an optical control pulse resonant with $|e\rangle - |s\rangle$. In order to recover the spin-wave excitation after time T_s to an optical excitation, a second optical control pulse is applied. If the transfer was done before time $\frac{1}{\Delta}$ after the second pulse, the AFC echo will be emitted after a time $\frac{1}{\Delta}+T_s$. This protocol is called spin-wave storage [19, 100]. Another advantage of spin-wave storage, besides the long storage times, is the possibility of choosing when to readout the stored field (on-demand) which is a crucial requirement for signal synchronization in a quantum repeater.

6.3 Static dipole moment and Stark shift

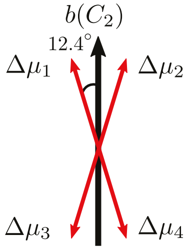

Figure 6.5. *The four possible orientations of the static electric dipole moments* $\boldsymbol{\Delta\mu}$ *of* Pr^{3+} *in* Y_2SiO_5 *.*

Y_2SiO_5 is a favorable host for REIs thanks to the low magnetic moments. The most abundant isotopes of Si and O have no nuclear magnetic moment, while yttrium has a small magnetic moment of $-0.13\mu_B$, where μ_B is the Bohr magneton [23]. This has positive effects on the coherence properties of REIs doped into this crystal. Y_2SiO_5 crystallizes as a monoclinic cell with a = 1.041 nm, b = 0.6726 nm, c = 1.249 nm, and the angle between a and c, denoted β, is 102.65°, [23]. It also has three principal axes; D_1, D_2, C_2, with three different refractive indices. In a monoclinic crystal, the three principal axes have different directions than the crystallographic axes. In the case of Y_2SiO_5 , b and C_2 are parallel, while D_1 is oriented at an angle of 79°relative to the a axis, and at 24°relative to the b axis. D_2 is perpendicular to D_1 and to C_2 (b) [23].

When Y_2SiO_5 is doped with Pr^{3+} , the Pr^{3+} ions can replace Y^{3+} in two nonequivalent sites; site 1 and site 2. One of the main differences between the Pr^{3+} ions in the two sites is the oscillator strength. Pr^{3+} ions in site 1 have an oscillator strength of 7.7×10^{-7}, which is about an order of magnitude higher than that of the ions in site 2 [73]. The experiments described in this thesis were performed using Pr^{3+} occupying site 1 only.

The ground state $|g\rangle$ and the excited state $|e\rangle$ in Pr^{3+}:Y_2SiO_5 have different static electric dipole moments, denoted $\boldsymbol{\mu}_g$ and $\boldsymbol{\mu}_e$, respectively. The difference in static electric dipole moment, $\boldsymbol{\Delta\mu} = \boldsymbol{\mu}_e - \boldsymbol{\mu}_g$, can have four different orientations as shown in Figure 6.5. When an electric field $\mathbf{E}$ is applied along the crystallographic b axis, this leads to two distinct classes of ions experiencing a Stark shift of equal magnitude but with opposite sign. These classes are here referred to as positive and negative electrically inequivalent classes. The magnitude of the Stark shift is given by Δf:

$$\Delta f = \frac{\boldsymbol{\Delta\mu} \cdot \mathbf{E}}{\hbar}, \tag{6.4}$$

where $\hbar$ is Planck's constant. This DC Stark shift has previously been used in combination with spectral hole burning in REIs to realize an optical frequency shifter [109], and to temporally compress optical pulses and control their group-velocity [110]. Furthermore, the Stark effect has been used as a means of coherent phase control of photon echoes [111–113] and of spin echoes [114]. It is also used in the CRIB memory scheme, where gradient electric fields are used to coherently control the collective emission from a narrow ensemble of ions microscopically [97, 115, 116].

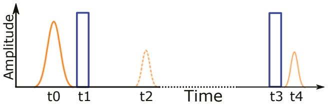

Figure 6.6. *Sequence used to implement Stark control of an AFC QM. At t0, the storage photon is sent through the crystal with a prepared AFC structure with a peak separation of Δ. Just after absorption, the first electric field pulse is applied at t1. Due to the phase difference of π between the two ion classes, echo emission is suppressed at $t2 = \frac{1}{\Delta}$. The second electric field pulse is applied during the time interval $\frac{n-1}{\Delta} < t3 < \frac{n}{\Delta}$, which removes the phase difference between the two ion classes, and the echo is emitted at $t4 = \frac{n}{\Delta}$*

6.4 Stark-controlled AFC memory

If the electric field is applied as a pulse, the two classes of frequency-shifted ions will accumulate a relative phase with respect to each other. For an arbitrary electric field pulse with a corresponding linear Stark frequency shift $\Delta f(t)$, and a duration T, the phase ϕ accumulated by the ions can be estimated as follows:

$$\phi = 2\pi \int_0^T \Delta f(t)\, dt, \tag{6.5}$$

For a square electric field pulse, the phases acquired by the two electrically inequivalent ion classes are $\pm 2\pi\Omega T$. In the study presented in Paper 2, phase control was used in combination with the AFC quantum memory to control the phase evolution of the ions. This was done by introducing a relative phase difference of π between the two ion classes using a suitable electric field pulse, which suppressed the echo emission. The phase difference between the ions is then eliminated by applying an opposite sing electric field pulse, and the phases of the ions continue to evolve as if they would before applying the electric field pulses. This effectively allows an on-demand readout of the stored field without the need for the bright control pulses used in spin-wave storage as described in Section 6.2.

In order to describe this atomic state, the collective excitation described in Equation 6.1 can be rewritten:

$$|\psi(t)\rangle = \frac{1}{\sqrt{2M}} \sum_{\ell=0}^{M-1} e^{i\Delta f_\ell t} \left[e^{i2\pi\Delta f T} \left|\psi_\ell^+\right\rangle + e^{-i2\pi\Delta f T} \left|\psi_\ell^-\right\rangle \right]. \tag{6.6}$$

where M is the number of peaks in the AFC, $\omega_\ell = 2\pi\Delta\ell$ (Δ is the AFC peak separation), and $\left|\psi_\ell^+\right\rangle$ and $\left|\psi_\ell^-\right\rangle$ are the wave functions of the positive and negative electrically inequivalent ion classes, which are defined as:

$$\left|\psi_\ell^\pm\right\rangle = \frac{1}{\sqrt{N_\ell^\pm}} \sum_{j=1}^{N_\ell^\pm} c_{\ell j}^\pm e^{2\pi i \delta_{\ell j}^\pm t} e^{-ikz_{\ell j}^\pm} \left| g_1 \ldots e_j \ldots g_{N_\ell^\pm} \right\rangle, \tag{6.7}$$

Where ± denotes the positive and negative electrically inequivalent ion classes. $N_\ell^\pm$ is the number of ions in peak ℓ that experience a positive/negative Stark frequency shift due to $\mathbf{E}$. The other parameters have similar definitions to those in Equation 6.1, with the exception that the two ion classes are distinct from each other.

The sequence used for Stark control to achieve on-demand retrieval of the stored photon is shown in Figure 6.4. Figure 6.7

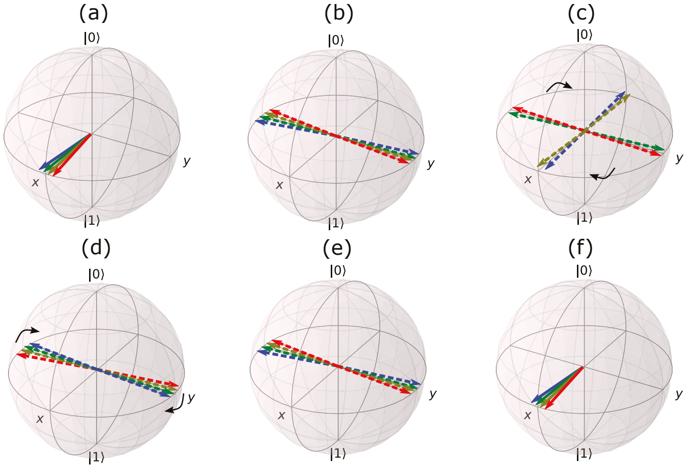

Figure 6.7: Phase evolution of the Stark-controlled AFC peaks on a Bloch sphere. The solid arrows represent all ions in the AFC peaks before applying the electric field, the dashed arrows represent the split of the two electrically inequivalent ion classes after applying the electric field. (a) after absorbing the storage photon, (b) after applying the first electric field pulse, (c) at $t = \frac{1}{4\Delta}$, (d) at $t = \frac{1}{2\Delta}$, (e) at $t = \frac{1}{\Delta}$, and (f) after applying the second electric field pulse in the time interval $[\frac{n-1}{\Delta}, \frac{n}{\Delta}]$ for $n \in \mathbf{Z}$

shows excerpt of the phase evolution of the AFC peaks, represented by colored arrows, on the Bloch sphere from the moment the storage photon is absorbed, to the moment it is emitted. The Stark controlled AFC scheme can be summarized using the Bloch representation as follows:

- At time T=0, after photon absorption, collective atomic excitation is initialized in a superposition state and are initially in phase. This is indicated in Figure 6.7 (a) by arrows of different colors, corresponding to ions in different AFC peaks, pointing in the same direction.

- During the time interval $0 < t < \frac{1}{\Delta}$, an electric field pulse with a duration $T = 1/4\Delta f$ is applied. This will introduce a difference in phase of $\pm\frac{\pi}{2}$ to the $\left|\psi_\ell^\pm\right\rangle$ wave functions, respectively. In Bloch representation, each vector will split into two with a phase difference π. Figure 6.7 (b) shows the vector when the electric field is applied just after the photon is absorbed and before the ions start to dephase.

- The two electrically in- equivalent ion classes, with a phase difference of π will continue to oscillate out-of-phase. Different ions will oscillate at different rates depending on their detuning from the central frequency of the AFC. Figures 6.7 (c) and (d) illustrate the phases at $t = \frac{1}{4\Delta}$, and at $t = \frac{1}{2\Delta}$, respectively.

- At $t = \frac{1}{\Delta}$, ions within the same class will oscillate in phase, but there will still be a phase difference of π between the two classes, and hence echo emission is suppressed. This moment on the Bloch sphere is shown in Figure 6.7 (e).

- During the time interval $\frac{n-1}{\Delta} < t < \frac{n}{\Delta}$, a second electric field pulse is applied with the opposite polarity. This will induce a phase difference of the same magnitude as the first applied pulse, but opposite in sign, and will thus remove the phase difference between the two ion classes, and the ions will continue to rephase. At times $t = \frac{n}{\Delta}$ for $n \in \mathbf{Z}$, all the ions will oscillate in phase as shown in Figure 6.7 (f), and the stored field is recalled (on-demand) as a coherent echo.

The addition of Stark phase control pulses provides an on-demand AFC protocol without the need for additional control pulses for spin-wave storage. The AFC recall efficiency in this scheme is limited by by the linewidth of the AFC peak as will be explained in the next chapter.

6.5 Stark-controlled spin-wave memory

Spin-wave storage scheme utilizes the long coherence time of ground-state hyperfine levels to provide longer storage times and an on-demand recall of the stored photons. However, this scheme is challenging to realize at single photon levels as the strong control pulses required to transfer the collective excitation create a lot of optical noise [20, 117, 118]. Consequently, in order to separate the stored photons from the inevitable optical noise, complex filtering schemes has to be implemented.

Stark phase control can be combined with spin-wave storage similarly to that discussed in Section 6.4. Figure 6.8 shows the pulse sequence required to implement the Stark-controlled spin-wave scheme. When the first electric field pulse is applied directly after absorption and before the first optical control pulse, it suppresses echo emission. The second electric field pulse is applied after the optical control pulse, and similarly, it removes the phase difference between the two ion classes in the AFC peaks, and recalls the suppressed coherent echo. At the same time, the ions excited by the second optical control pulse that contribute to the coherent optical noise are brought out-of-phase by the second electric field pulse, which suppresses the coherent optical noise emitted by those ions. An additional advantage of combining Stark-control with spin-wave storage is the flexibility it introduces to the timing

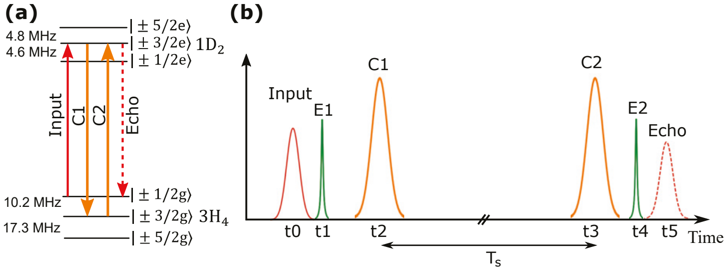

Figure 6.8: (a) Typical level configuration for realizing spin-wave storage. The AFC is prepared in the ground state $|g\rangle$ by optical pumping to an auxiliary state $|aux\rangle$, and the storage light is resonant with $|g\rangle \rightarrow |e\rangle$. Two optical control pulses are used to transfer the excitation to and from the long lived spin level $|s\rangle$. The echo is emitted after the second control pulse. (b) Pulse sequence used for the combined scheme of spin wave storage and Stark phase control. An electric field pulse is applied after absorption to switch off the echo emission before the first transfer pulse. Another electric field pulse is applied after the second spin control pulse to switch the echo emission on and at the same time switch all other coherent optical noise off.

and the duration of the spin transfer pulses. In spin-wave storage, the first optical control pulse has to be applied before echo re-emission, i.e. during the time interval $0 < t < \frac{1}{\Delta}$, which could be technically challenging. However, it would be possible to have the flexibility to apply the optical control pulse, without risking a partial re-emission of the echo during transfer, by applying a short electric field pulse that switches off the echo emission.

Chapter 7

Experimental Realization of a Stark-Controlled AFC QM

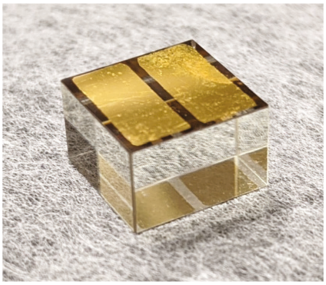

Figure 7.1. *Pr^{3+}:Y_2SiO_5 crystal used in the AFC QM experiments, showing the cold-coated electrodes (courtesy of Sebastian Horvath).*

This chapter discusses the experimental realization of Stark control in AFC and spin-wave quantum memories, which was presented in Paper II and Paper III. Section 7.3 describes the preparation of the AFC structure in Pr^{3+}:Y_2SiO_5 , where a six-level Bloch simulator was used to optimise the preparation sequence. The AFC was tested by storing a classical intensity pulse and retrieving it. This was followed by a measurement of the Stark coefficient as described in Section 7.2. Section 7.3 presents the work done towards realizing a Stark controlled AFC storage. It also describes the results obtained for storage of both classical and weak-coherent light states, and the effect of the peak width on the storage time is characterized. A theoretical model that describes this dependence on the peak width is also presented and used to estimate the potential of the presented scheme in other materials. Section 7.4 discusses the progress towards realizing Stark controlled spin-wave storage and the potential of this control in improving the noise performance of spin-wave storage at the single photon regime. Finally, Section 7.5 describes attempts to use Stark control to spectrally split and combine light pulses, and to coherently control the free induction decay (FID) emission.

7.1 AFC storage

The QM experiments discussed in this Chapter were performed on the Pr^{3+}:Y_2SiO_5 crystal shown in Figure 7.1. The doping concentration of Pr^{3+} was 500 ppm, and the crystal dimensions were $10 \times 10 \times 6$ mm, corresponding to the $D_1 \times D_2 \times b$ axes, respectively. The light used in the experiments was polarized along the D_2 optical extinction axis in order to make use of the high optical

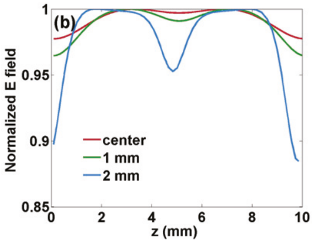

Figure 7.2. *COMSOL simulation of the electric field (red) at the center of the crystal, (green) 1 mm off the center, and (blue) 2 mm off the center, all along the direction of light propagation axis (D_1) [119].*

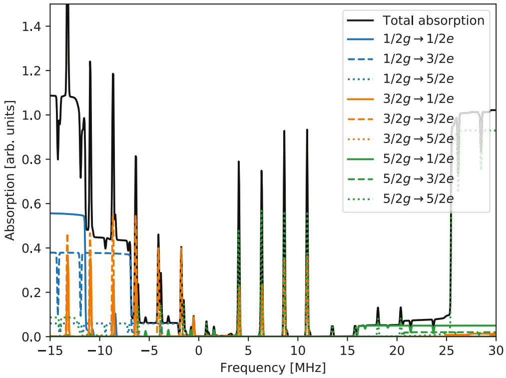

Figure 7.3: Absorption structure from six level Bloch simulation using the sequence described in the Appendix of Paper II. Different colors correspond to contributions of transitions between individual hyperfine levels. The black line is the combined absorption profile.

depth of that axis [23]. The two surfaces perpendicular to the *b* axes are coated with a pair of gold electrodes to allow an electric field to be applied along the *b* axis for Stark control experiments as discussed in Section 6.3. Figure 7.2 shows the simulated electric field across the crystal.

The hyperfine level structure of Pr^{3+}:Y_2SiO_5 was shown in Figure 2.2. An ion in one of the three hyperfine ground states can be excited to any of the three hyperfine excited states with different probabilities depending on the oscillator strength of each transition. The oscillator strength of the nine possible transitions can be seen in Table 2.1. Before creating any structures, optical pumping was used to depopulate the $|1/2g\rangle$ and $|3/2g\rangle$ levels to create an 18 MHz wide spectral pit using the pulse sequence described by Amari *et al.* [120]. A six level Bloch simulator, developed by the Quantum Information Group at Lund University, was then used to optimize burn-back sequences used to create the spectral structures used in the experiments. A detailed description of the simulator can be found in Ref. [121] Figure 7.3 shows the results of simulations when using the pulse sequence described in the Appendix A of Paper II to burn-back four AFC peaks. In order to increase the effective absorption depth of the AFC, and consequently the storage efficiency, the peaks were formed by burning back four distinct narrow ion ensembles, separated by 2.4 MHz for their $|5/2g\rangle \rightarrow |5/2e\rangle$ transition, to the $|5/2g\rangle$ state. In order to further increase the absorption of the peaks, two further ion ensembles that had their $|3/2g\rangle \rightarrow |1/2e\rangle$ or $|3/2g\rangle \rightarrow |3/2e\rangle$ spectrally overlapped with the $|5/2g\rangle \rightarrow |5/2e\rangle$ peaks.

The absorption coefficient, α, along the D_2 axis in a Pr^{3+}:Y_2SiO_5 crystal with 500 ppm doping has been determined to be 47 ± 5 cm^{-1}, compared to 3.6 ± 0.5 cm^{-1} along the D_1 axis [23]. At such high absorption levels, probe light travelling through the crystal allow to readout of the absorption structure will be completely absorbed, making it difficult to characterize the structures created. One way to overcome this, is to propagate the light along the b axis, create the structures with light polarized along the highly absorbing D_2 axis, and probe the structure using weak light polarized along the weakly absorbing D_1 axis. This was not possible in the crystal described above as it had two pairs of gold-coated electrodes on the surfaces perpendicular to the b axis. Therefore, a different crystal with the same Pr^{3+} doping concentration but 12 mm long was used to test the burning sequence and characterize the structures. In this crystal, the light propagates along the b axis, and and can be polarized along either D_1 or D_2. Figure 7.4 (a) shows the absorption structure probed by light polarized along the D_1 axis ($\alpha L \sim 0.8$). A value of $\alpha L \sim 9$ was estimated for light polarized along D_2 in the crystal used for the memory experiments shown in Figure 7.1. The width of the AFC peaks was determined to be $\gamma = 140$ kHz (see Appendix B of Paper II for detailed discussion about the peak width measurement), and the peak separation $\Delta = 2.3$ MHz. With such a comb, the theoretical AFC efficiency estimated using Equation 6.2 was 17%. Figure 7.4 (b) shows the transmission of a Gaussian optical pulse with FWHM of 150 ns propagating through the crystal, before and after preparing the comb structure. The retrieval efficiency of the stored pulse was 35%, suggesting an optical depth of $\alpha L \sim 15$. The discrepancy between the absorption depths estimated in the two crystals could be attributed to a shift of the center frequency of the inhomogeneous absorption profile and/or broadening of the absorption profile due to different crystal mounting or inherent differences in the sample [122].

7.2 Stark coefficient

A high-speed operational amplifier with a gain of 13 V/V was used to apply the required electric fields [1]. Two such amplifiers were connected in a push-pull configuration to increase the supplied voltage across the crystal to 26 V. In order to further increase the field experienced by the ions, a DC voltage of +26 V was constantly applied across the crystal, and flipping the polarity of this applied voltage will cause the ions to experience an electric field of 86.7 V/cm (52/0.6). Larger electric field enables shorter pulses to control the ions.

---

[1] THS3491DDA Evaluation Module. The amplifier has a default gain of 5 V/V, but it was modified to give a gain of 13 V/V (see the circuit)

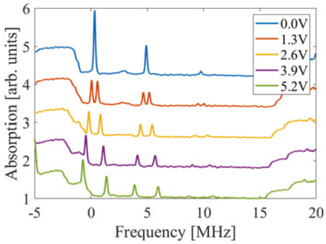

Figure 7.5. *The absorption structure of a narrow peak in the $|1/2g\rangle$ state at different applied DC electric fields. The three peaks in the blue trace corresponds to transition from the $|1/2g\rangle$ to $|1/2e\rangle$, $|3/2e\rangle$, and $|5/2e\rangle$. When applying electric field, the two ion classes in the peak experience equal and opposite stark shifts, which lead to the splittings in shown in the lower traces.*

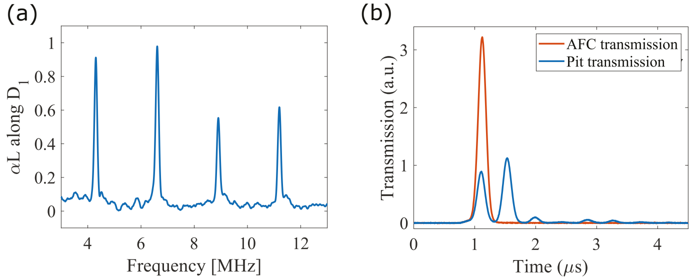

Figure 7.4: (a) Measured absorption structure along the D_1 axis of the AFC created using the optimised sequence discussed in Appendix of Paper 1. The peak width $\gamma = 140$ kHz and the peak separation $\Delta = 2.3$ MHz, which means that the AFC echo is emitted after 435 ns. (b) Transmission through an empty spectral pit (red), and through the AFC (blue). The first peak in the blue trace is the part of the input pulse transmitted directly through the AFC, the second peak is the first echo, and later peaks are higher-order echoes. By comparing the intensity of the first echo with that of the direct transmission through an empty pit, the retrieval efficiency of the AFC was estimated to be 35%.

In order to measure the Stark coefficient, a narrow ensemble of ions was burned back to the $|1/2g\rangle$ level. The absorption structure of this peak is shown by the blue trace in Figure 7.5. When the electric field was applied across the b axis of the crystal, the spectral peak split into two equal peaks due to the two electrically inequivalent ion classes experiencing opposite Stark shifts. Varying the magnitude of electric field causes the magnitude of the Stark shift to change as shown in Figure 7.5. Figure 7.6 shows the obtained Stark shift at different applied voltages, and a Stark coefficient of 121 kHz/(V/cm) was obtained from the slope. This agrees with a previously reported Stark coefficient of 112 kHz(V/cm) in Pr^{3+}:Y_2SiO_5 [113]

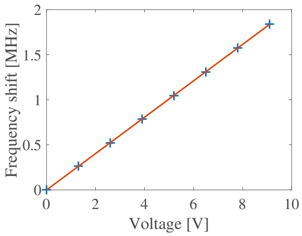

Figure 7.6. *Frequency shift as a function of the applied voltage.*

It is then possible to estimate the pulse duration required to introduce a phase difference of π between the two electrically inequivalent ion classes ($\pm\frac{\pi}{2}$ to each ion class, respectively). Assuming a square electric field pulse, the relation between the pulse duration, T, and the frequency shift, Δf, that would introduce such a phase difference can be calculated using Equation 6.5, and is given by:

$$T = \frac{1}{4(\Delta f)} \tag{7.1}$$

For an electric field of 86.7 V/cm, a pulse duration of 24 ns would give a phase difference of π between the two ion classes. These parameters were used for the AFC switching discussed in Sections 7.3 and 7.4.

7.3 A Stark-controlled AFC

This section discusses the results presented in Paper II, where the Stark effect was utilized to realize on-demand recall of the field stored in an AFC QM, without the need for Spin-wave storage. The storage was performed with both classical intensity light and with weak coherent states.

7.3.1 Experimental setup

The optical setup used for the experiments is shown in Figure 7.7. The light source used was a Coherent 699-21 ring dye laser, locked to an external ultra-low expansion (ULE) cavity at 494.723 THz, resonant with the $^3H_4 \rightarrow {}^1D_2$ of Pr^{3+} in site 1. The external locking has been described in detail elsewhere [119]. Light pulses were generated through a combination of a double-pass AOM1 and a single-pass AOM2 in series, through which it is possible to arbitrarily tailor the phase, frequency and amplitude of the pulses. Both AOMs were driven by an arbitrary waveform generator. Besides pulse tailoring, these AOMs were used to attenuate the light down to the single photon level for the weak-coherent state storage experiments. After the AOMs, the light propagates through a polarization maintaining fiber towards the experimental setup. 10% of the light is reflected by a 90:10 beam splitter towards a reference detector before passing through the crystal. This reference light is used later to compensate for power fluctuations. In order to further attenuate the light, an optional neutral density filter is attached to a motorized mount. A $\frac{\lambda}{2}$ waveplate and a Glan-Thompson polarizers were used to ensure light polarization along the D_2 crystal axis. The light is then focused into the crystal, which is mounted inside a bath cryostat where it is cooled to 2.1 K. The light is collected after propagating through the crystal and focused into the detector. For weak coherent state measurements, a Laser Component Count 50N avalanche photodiode was used, which has a quantum efficiency of 0.69 at 606 nm and a dark count of 26 Hz.

Figure 7.8 shows the modified circuit of the THS3491 high-speed, high-voltage, low-distortion-current feedback amplifier [123]. This amplifier was used to generate the electric field pulses used throughout the QM experiments. A 61.9 Ω resistor replaced the default 187 Ω resistor, as the later gave a non-inverting gain of 5V/V. The 61.9 Ω resistor increased the gain to 13 V/V.

Additionally, a 49.9 Ω resistor replaced several resistors on the output side of the amplifier. Two such amplifiers were connected together in a push-pull configuration to get to a gain of 26V/V. To further increase the electric field experienced by the ions, a DC 26 V was applied across the crystal all the time, the electric field pulses were applied by flipping the polarity of the applied field.

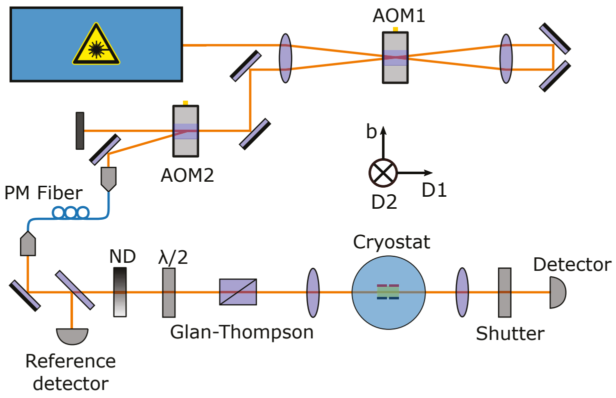

Figure 7.7: Optical setup used in the Stark-controlled AFC QM experiments.

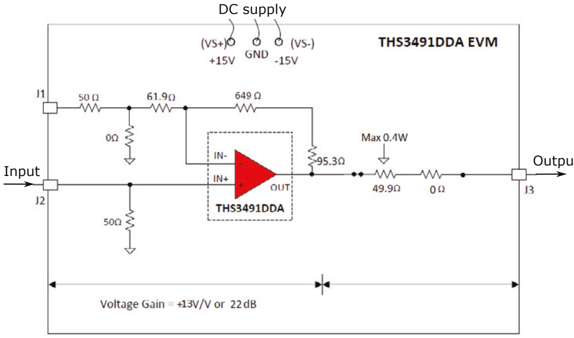

Figure 7.8: The modified circuit of the THS3491 fast amplifier used to apply the voltage across the crystal. The gain was 13V/V.

This lead to an effective voltage difference of 54 V applied to the ions, allowing for the use of very short electric field pulses for the switching.

7.3.2 Experimental realization

The AFC structure used for the experiments was the same as that described in Section 7.1. However, a DC voltage difference of 26 V was constantly applied to the gold-coated electrodes before, during and after preparing the spectral pit and the AFC peaks. The stored light consisted of a Gaussian pulse resonant with the central frequency of the AFC and with a FWHM of 150 ns. The electric field pulses were applied by flipping the polarity of the constantly applied field across the crystal, giving an effective field of 86.7

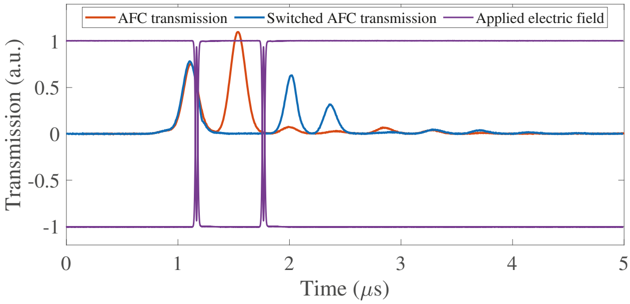

Figure 7.9: AFC transmission without (red), and with (blue) application of electric field pulses (purple). The first peak in the red and blue traces is the part of the input pulse directly transmitted through the comb. The second peak is the first recalled echo, followed by higher order echoed. The electric field pulses were applied by flipping the polarity of the constantly applied DC voltage.

V/cm experienced by the ions. The FWHM of the electric field pulses was 23 ns.

Figure 7.9 shows the AFC echo with and without application of the electric field pulses. Light emission was completely quenched after applying the first electric field pulse directly after absorption of the input. The second electric field pulse was applied such that the echo is re-emitted at the second rephasing cycle ($\frac{2}{\Delta}$), and the intensity of the electrically switched echo was $\sim$ 71% of that of the non-switched echo. This reduction in the memory efficiency is limited by the FWHM of the AFC peaks. This dependence will be discussed in more details below.

The time before applying the second electric field pulses was varied in steps of 50 ns while recording the AFC transmission at each step. Figure 7.10 (a) shows a map of the echo recall efficiency at different times. It should be noted that the echo could only be recalled at the discrete times $T = \frac{n}{\Delta}$ for $n \in \mathbf{Z}$. In order to demonstrate the usefulness of this protocol at the single-photon level, the experiment was repeated using weak-coherent states, with an average of 0.097 ± 0.004 photons per pulse, as memory input. The recall efficiency for weak coherent state storage is shown in Figure 7.10. The power of the light was calibrated by removing the crystal from the beam path, and attenuating the light to the aforementioned level of 0.097 photons per pulse, after compensating for the detector quantum efficiency and the losses in cryostat window. The obtained efficiency map for is shown Figure 7.10 (b). Each storage trace in the figure was obtained by accumulating 3×10^4 storage-pulses; over 15 AFC creation cycles, and 2000 storage-pulses per AFC creation cycle.

Apart from the on-demand readout of the stored photons, an-

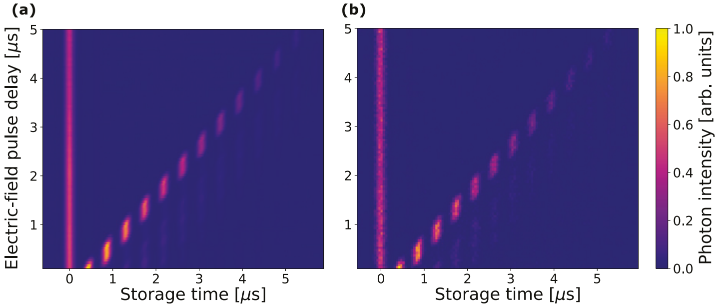

Figure 7.10: Light transmission through the AFC QM using (a) classical light as memory input, and (b) using weak coherent states with an average of 0.097 ± 0.004 photons per pulse.

other important advantage of this scheme is the high SNR due to the absence of any bright control pulses like the ones used in spin-wave storage scheme. The SNR for weak coherent states with an average of 0.097 ± 0.004 photons per pulse and a storage time of 850 ns was measured and found to be 570 ± 120. The SNR was estimated by dividing the accumulated echo signal from $3{\times}10^4$ shots in a 350 ns time bin by the noise floor. The noise floor here was the dark count accumulated over $3{\times}10^4$ shots in a time bin of the same duration. Consequently, an order of magnitude higher SNR can be expected if a single-photon Fock state is used for storage. For comparison, an SNR of $\sim$ 10 has been reported for a storage time of 1 μs, using 1 photon per pulse as memory input.

7.3.3 Effect of AFC peak broadening

The decrease in the echo recall efficiency for longer storage times, shown in Figures 7.10 (a) and (b), is attributed to the comb-peak width (140 kHz), which leads to decoherence and a loss of phase information in the peak ensembles. In order to investigate this effect, the analytical model presented by Afzelius *et al.* [100] was modified to include the effect of Stark phase control. The echo recall efficiency in this case can be written:

$$\eta = (\tilde{\alpha}L)^2 e^{-\tilde{\alpha}L} e^{-t^2\tilde{\gamma}^2}, \tag{7.2}$$

where, $\tilde{\alpha} = \frac{\alpha}{F}\sqrt{\frac{\pi}{4\ln(2)}}$ is the effective absorption of the AFC, $\tilde{\gamma} = \frac{2\pi\gamma}{\sqrt{8\ln(2)}}$ is the comb FWHM, and t is the storage time.

In order to measure the effect of peak width on the recall efficiency, the storage experiment was repeated for several comb-peak widths. The burning sequence was optimized on the 12 mm long crystal mentioned in Section 7.1 where light used to create the structure was polarized along D_2 axis, while the light used to

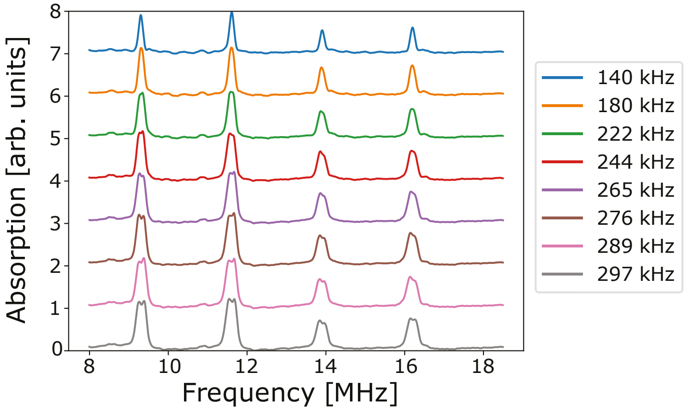

Figure 7.11: Absorption of multiple AFCs with different peak widths measured along D_1 axis in the 12 mm long crystal. The widths were obtained by fitting the peaks to a Gaussian.

probe the created structure was polarized along D_1 axis. The AFC peaks were burned back into the empty spectral pit using complex hyperpolic secant (sechyp) pulses [124, 125]. Different peak widths were obtained by varying the frequency width of the sechyp pulses, and the intensity was scaled to achieve a similar peak absorption. Figure 7.11 shows the absorption of multiple AFC structures with different peak widths, measured along D_1. The peak widths were estimated from a Gaussian fit to the peaks, and an uncertainty of 5% in the peak width was estimated from multiple measurements. Refer to Appendix B of Paper II for a detailed discussion of the peak width estimate.

Figure 7.12 shows the recall efficiency measured at different storage times, and for AFCs with different peak widths γ. The recall efficiency was obtained by comparing the intensity of the echo to the intensity of a pulse transmitted through an empty 18 MHz wide spectral pit. The data were fitted to the recall efficiency calculated using Equation 7.2. The good agreement between the data and the model indicates that the decay rate of the echo is limited only by the linewidth of the AFC peaks, which is limited by the optical coherence time of 152 μs Pr^{3+}:Y_2SiO_5 [60]. If the electric field pulses were to perturb the phases, this would have been seen on the recall efficiency. We thus conclude that this scheme is phase preserving, and capable of storing quantum states with high fidelity.

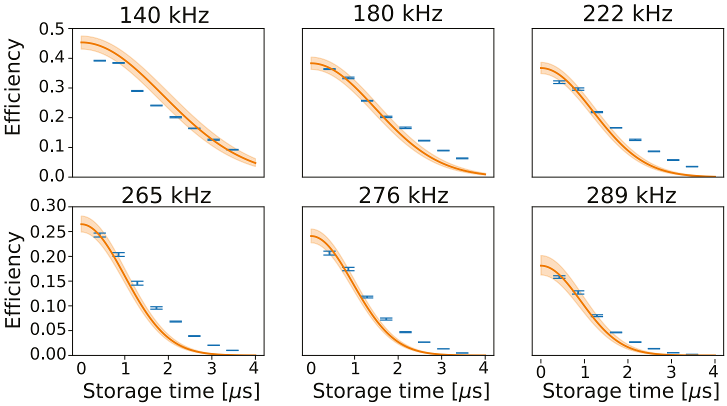

Figure 7.12: A set of efficiencies measured for different peak-width fitted to the efficiency estimated using Equation 7.2 of the main text. Uncertainties of measured efficiencies correspond to the standard error, while the model efficiency is calculated form a 5% uncertainty in the peak linewidth

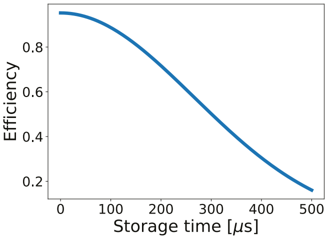

Figure 7.13. *Recall efficiency as a function of storage time for an AFC in an impedance matched cavity. See text for parameters used in the AFC and the cavity*

7.3.4 Potential of Stark-controlled AFC scheme in other materials

The model presented in Equation 7.2 allows the assessment of the potential of the Stark-controlled memory scheme in other materials with longer optical coherence times. In order to further increase the recall efficiency, one can consider combining the AFC with an impedance matched optical cavity [101]. This will have no effect on the dephasing term in Equation 7.2, but will significantly enhance the absorption of the storage photon. The impedance matching condition will be fulfilled when the absorption per cavity round trip exactly matches the transmission of the coupling mirror[101]. In this case, the recall efficiency of a Stark-controlled AFC QM in an optical cavity is given by:

$$\eta_{\text{cav}} = \frac{4(\tilde{\alpha}L)^2 e^{-2\tilde{\alpha}L}(1-R_1)^2 R_2 e^{-t^2\tilde{\gamma}^2}}{(1-\sqrt{R_1R_2}e^{-\tilde{\alpha}L})^4}, \tag{7.3}$$

where R_1 and R_2 are the mirror reflectivities. Figure 7.13 shows the recall efficiency based on this modified model as a function of storage time for an AFC memory in an impedance matched cavity. The AFC here is assumed to have a peak linewidth of $\gamma =$ 1 kHz, peak separation of $\Delta = 50$ kHz, and an optical depth of $\alpha L = 1$ [18]. The reflectivities of the cavity mirrors are $R_1 = 96\%$ and $R_2 = 99.9\%$. From the model, one can expect a memory recall efficiency of 88% for a photon stored for $\sim 100\mu$s. Such a storage time and recall efficiency would be practical in a second-generation quantum repeater [126], and could be achievable using a Eu^{3+}:Y_2SiO_5 crystal, in which persistent holes with a width on the order of kHz have been used extensively for laser frequency stabilization [122, 127, 128]. When using Eu^{3+}:Y_2SiO_5 , it would require up conversion to telecom wavelength, e.g., using periodically poled nonlinear crystals. Such frequency conversion may also have an intrinsic efficiency of 100% for single photons [129]. An alternative material, avoiding the complication of frequency conversion, may be Er^{3+}:Y_2SiO_5 . However, it is not trivial to achieve good hole-burning in Er^{3+}:Y_2SiO_5 since Er^{3+} is a Kramers ion, which is a key requirement for AFC-based quantum memories. Although successful hole-burning has been achieved in spin-polarized $^{167}Er^{3+}$:Y_2SiO_5 with a large external magnetic field [130], it may be challenging to realize the necessary conditions simultaneously with the magnetic field requirements necessary for narrow homogeneous linewidths [131, 132].

7.4 Stark-controlled Spin-Wave storage

This section describes the experimental work performed towards realizing Stark-controlled spin-wave storage, which is presented in Paper III. It is generally challenging to realize spin-wave storage at the single photon regime due to the optical noise created by the strong control pulses used for the spin transfer [20, 117]. The optical noise could be due to spatial leakage from the control pulses into the memory input mode due to scattering or reflection from optical surfaces (crystal surface, cryostat windows, and AOMs). This noise is usually reduced by a gated detection since the control and the input are temporally separated. It can also be reduced by having the control pulses propagating through the crystal at different angle than the input mode (spatial filtering). The other source of the optical noise is due to emission from ions excited by the control pulses. This emission could be incoherence fluorescence from ions on the sides of the spectral pit that were off-resonantly excited by the bright control pulses. It could also be coherent emission from residual population in the spin storage state due to imperfect optical pumping, which gives rise to an FID emission when excited by the control pulses. Furthermore, the control pulses could also off-resonantly excite the AFC, leading to an undesired echo emission at the same frequency as the input field, but temporally separated [117]. These types of emission are more difficult to reduce, and it usually requires complex spectral and temporal filtering techniques for the spin-wave storage scheme to work at the single photons level.

One of the main advantages of using Stark-control in spin-wave scheme is suppression of the coherent background noise, which improves the scheme performance for single photons storage. Furthermore, switching the echo emission using the first electric field pulse would give more time to apply the first control pulse without the echo being emitted too soon during the spin transfer.

7.4.1 Experimental setup

The setup used for spin-wave storage experiments is shown in Figure 7.14.

The spin-wave storage experiment was first performed without using spectral filtering (the blue block in the figure), then we added that to filter off resonant background.

The light source used was a Coherent 699-21 ring dye laser, locked to an external ultra-low expansion (ULE) cavity at 494.723 THz, resonant with the $^3H_4 \rightarrow {}^1D_2$ transition of Pr^{3+} in site 1. Light pulses were generated with a combination of a double-pass AOM1 and a single-pass AOM2 in series, making it possible to arbitrarily tailor the phase, frequency and amplitude of the pulses. Both AOMs were driven by an arbitrary waveform

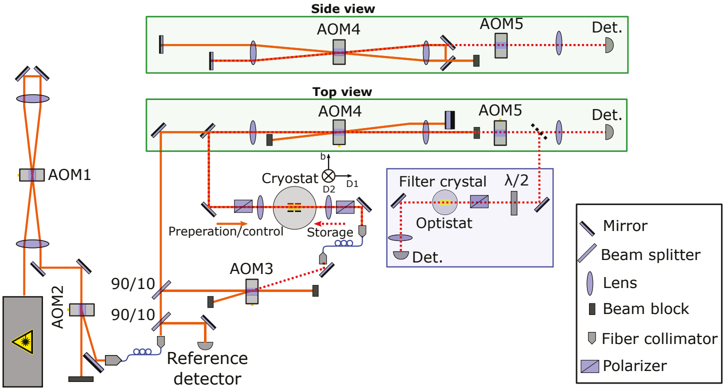

Figure 7.14: Optical setup used for spin-wave storage of weak coherent states

generator. These AOMs were also used to attenuate the light to the single-photon level for the weak coherent state storage experiments. After the AOMs, a 90:10 beam splitter was used to reflect 10% of the light towards a reference detector used to compensate for power fluctuations. The rest of the light was split once more by another 90:10 splitter, and the weaker beam passed through the single-pass AOM3, and propagated through the crystal in the forward direction (red dotted line). This light was used for storage. The crystal was mounted inside a bath cryostat and cooled to 2.1 K. The rest of the light transmitted through the second beam splitter passes through the double pass AOM4 setup, and then propagates through the crystal in the backward direction (solid orange line). This light was used for pit burning, AFC preparation, and spin-transfer. The memory output (propagating in the forward direction) passes through AOM4 in a single pass when it is off (0^{th} order), and is spatially separated and directed towards the gating AOM5, after which it is detected.

The storage was first performed with classical light intensities as an input, and the memory output was detected by a photo-diode [2] connected to a transimpedance amplifier [3]. Then, weak coherent states were used as a memory input, and the noise performance of the scheme was investigated with and without spectral filtering before detection. The spectral filtering was implemented using a narrow spectral hole filter prepared in a second crystal that was cooled to 4 K in a flow cryostat (optistat). The spectral hole filter setup is shown in the blue-shaded box in Figure 7.14. The setup for spectral hole filter preparation is not shown in the figure. An additional AOM was added after the second 90:10 beam splitter,

---

[2] Hamamatsu photo-diode S5973

[3] FEMTO DHPCA-100 variable gain transimpedance amplifier

the 0^{th} order of this additional AOM (off) was used to prepare the spectral pit and the AFC structure in the experimental crystal. After which, the AOM was switched on, and the 1^{st} order diffracted beam was directed towards the filter crystal for filter preparation.

7.4.2 AFC preparation

The six-level Bloch simulator was used for initial optimization of the burning pulse sequence used to create the AFC for this experiment. The goal was to create 4 narrow peaks with FWHM =140 kHz, separated by $\Delta = 600$ kHz. The pulse sequence used to create the comb structure is given in Table 7.1, and the simulated absorption structure is shown in Figure 7.15 (a).

The burning sequence was then tested and optimized further on a 12 mm long Pr^{3+}:$\mathrm{Y_2SiO_5}$ crystal with nominally equivalent doping concentration of Pr^{3+} . After creating an 18 MHz spectral window in the center of the inhomogeneous line, four distinct narrow group of ions separated by 600 kHz for their $|1/2g\rangle \rightarrow |1/2e\rangle$ transitions were burned back to the $|1/2g\rangle$ state. As a result of this, some undesired ions were burned back in the pit. These were cleaned away using hybrid pulses combining the edges of a sechyp pulse with a linear frequency chirp with a frequency scan range of 8.5-14.5 MHz.

Pulse name	ν (MHz)	ν_{width} (MHz)	t_{FWHM} (μs)	t_{cutoff} (μs)	Target transition	Reps
BurnbackAFC1	23.1	0.1	11.2	40	$\lvert 5/2g\rangle \rightarrow \lvert 1/2e\rangle$	40
BurnbackAFC2	23.7	0.1	11.2	40	$\lvert 5/2g\rangle \rightarrow \lvert 1/2e\rangle$	40
BurnbackAFC3	24.3	0.1	11.2	40	$\lvert 5/2g\rangle \rightarrow \lvert 1/2e\rangle$	40
BurnbackAFC4	24.9	0.1	11.2	40	$\lvert 5/2g\rangle \rightarrow \lvert 1/2e\rangle$	40
CleanAFC	11.5	0.5	3.0	86	$\lvert 3/2g\rangle \rightarrow \lvert 5/2e\rangle$	200

Table 7.1: The ν column lists the relative center frequencies of the pulses. The frequencies are defined with respect to the $|1/2g\rangle \rightarrow |1/2e\rangle$ transition, for an arbitrary ion class, which is set to be at zero. The light intensity for each pulse was chosen such that it matches the Rabi frequency to the relative oscillator strength of the target transitions, shown in the sixth column. The cleaning pulse utilized a hybrid pulse combining the edges of a sechyp pulse with a linear frequency chirp. The parameters indicated in the table pertain to the sechyp parameters, whereas the linear frequency scan for cleaning pulse was 6 MHz. The Reps column shows the number of repetitions used for each of the pulses used.

Figure 7.15 (b) shows the measured absorption structure of the AFC probed with light polarized along the D_1 axis in the 12 mm long crystal. Despite the fact that the probe pulse was polarized along D_1, the absorption of the peaks was too high to obtain a reliable readout of the peaks optical depth αL.

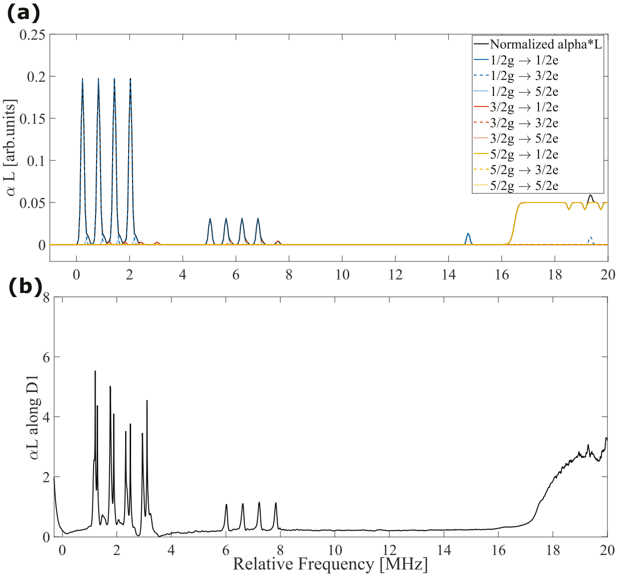

Figure 7.15: (a) Absorption structure from six level Bloch simulation. Different colors correspond to contributions of transitions between individual hyperfine levels. The black line is the combined absorption profile. (b) Measured absorption structure along D1 crystal axis in a different sample with the same doping concentration. Due to the high αL, the peak width and the absorption are not resolved. The four peaks around 2 MHz correspond to the $|1/2g\rangle \rightarrow |3/2e\rangle$ transition used for storage, while the ones around 6.2 MHz correspond to the $|1/2g\rangle \rightarrow |5/2e\rangle$ transition

7.4.3 Storage of bright pulses

Before implementing the full spin-wave storage scheme, the AFC was first tested by storing a bright optical pulse and delaying its recall using electric field pulses, and the recall efficiency obtained for a storage time of 3.3 μs was 8.4 %. The pulse sequence used for the full spin-wave storage scheme combined with Stark-control is shown in Figure 7.16 (b). The sequence consists of a Gaussian input pulse with FWHM = 500 ns, resonant with the $|1/2g\rangle \rightarrow |3/2e\rangle$ transition sent through the crystal. The first electric field pulse was then applied during the time $0 < t < \frac{2\pi}{\Delta}$ to add a phase difference of π between the two electrically inequivalent ion classes, and consequently, quench echo re-emission. Shortly afterwards, the first bright control pulse, resonant with the $|3/2e\rangle \rightarrow |3/2g\rangle$ transition, was used to bring the collective excitation to the $|3/2g\rangle$ hyperfine ground state. After a variable time duration T_s, a second identical bright pulse was used to bring the collective excitation back from the spin level to the $|3/2e\rangle$ state. The second electric

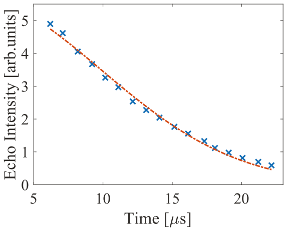

Figure 7.17. *The crosses indicate the measured echo intensity at different spin storage times, the red line is a Gaussian fit to Equation 7.4, where an inhomogeneous spin linewidth of 26.8 ± 0.8 kHz was obtained.*

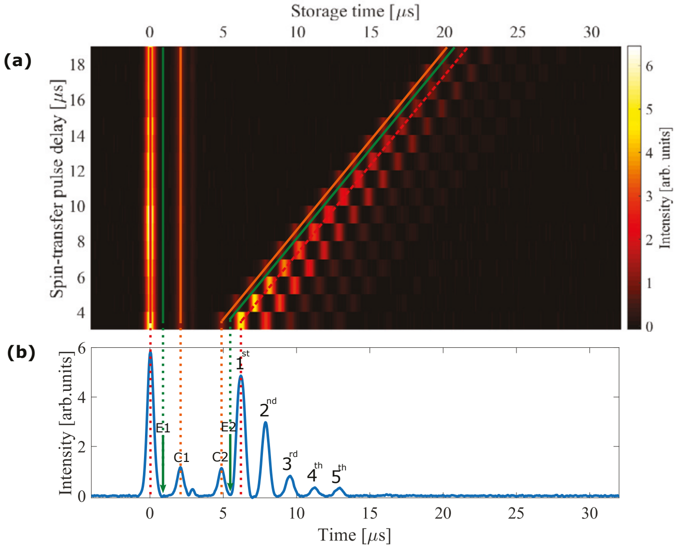

Figure 7.16: (a) Spin-wave storage with classical intensity input for varying storage times, and (b) for the shortest storage time. The first pulse marked by the solid red line in the map is the part of the storage light directly transmitted through the AFC without being stored. The first electric field pulse was applied directly after absorption at the time marked by the first green line. The second faint pulse marked by the orange line is scattering of the first control pulse that leaked into the detection path. The second orange line (tilted) is scattering from the second control pulse applied at varying times. This is followed by another electric field pulse marked by the second green line (tilted). The dashed red lines is the restored echo after rephasing. The rest of the peaks peaks are higher order echoes.

field pulse was then applied during the time interval $\frac{n-1}{\Delta} < t < \frac{n}{\Delta}$ to remove the π phase difference between two the ion classes, and allow the collective excitation to rephase and emit the stored pulse as a coherent echo. Figure 7.16 (a) shows the recalled echoes for several storage times, where the timing of the second electric field pulse and the second bright control pulse was delayed to obtain a longer storage times. The recall efficiency changed from 2.8% for the shortest storage time of 6.2 μs, to 0.64% fora storage time of 21.2 μs.

The exponential decay of the echo intensity, which can also be seen in Figure 7.17, is due to the inhomogeneous broadening of the spin transition. This was confirmed by fitting the echo intensity against the spin storage duration (T$_s$) to the following Gaussian [133]:

$$\mathrm{I}(\mathrm{T}_s) = \mathrm{I}_0 \times \exp\left[\frac{-(\gamma_{IS}T_s)^2}{2\ \log(2)/\pi^2}\right], \tag{7.4}$$

where I_0 is a constant, and γ_{IS} is the inhomogeneous spin linewidth. A spin inhomogeneous linewidth of 26.8 ± 0.8 kHz was obtained from the fitting, in agreement with previous measurements in the same material[19, 20]. This confirms that the Stark control, when combined with spin-wave storage scheme, does not contribute to any additional dephasing.

It should be noted that, without applying an electric field, the echo is re-emitted after 1.67 μs. The control pulses used for spin transfer were 1.5 μs long. If the first control pulse was to be applied without using Stark phase control to switch off echo re-emission, a major part of the ion ensemble would rephase before it was transferred to the spin state, and hence the transfer efficiency would be rather poor. Thanks to the Stark control, spin-wave storage can be applied in AFCs where it otherwise will not be possible.

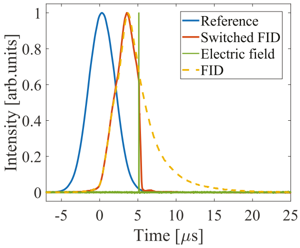

Figure 7.18. *FID quenching using an electric field pulse. The blue line is the Gaussian pulse before propagating through the crystal. The yellow dashed line is the transmission after going through the narrow peak, with an extended FID emission. The green line shows the electric field pulse applied to switch the FID emission. The orange line shows the switched FID.*

7.4.4 Switching-off coherent emission

As mentioned earlier, one of the noise sources in spin-wave scheme is FID emission by remaining population in the spin state which are excited by the control pulses. In order to demonstrate the capacity of Stark-control to suppress this FID emission, a single 140 kHz peak was burned-back in an empty 18 MHz spectral pit. An optical Gaussian pulse with FWHM of 4 μs at the same frequency as the peak was sent through the crystal. After absorption, the atoms are put in a superposition state where they oscillate in phase and emit coherently in the form of FID. The atoms continue to emit for as long as they are still in phase. The dephasing time, $\mathrm{T}_2^\star$, is defined by Equation 2.2, and for the 140 kHz peak ensemble, $\mathrm{T}_2^\star = 1.87$ μs. By applying a suitable electric field pulse, the two electrically nonequivalent ions classes contributing to the FID emission were put out of phases, which consequently lead to a quenching of the FID emission. Figure 7.18, shows the FID emission with and without applying the electric field.

7.4.5 Noise characterization at the single photon regime

In order to assess the effectiveness of Stark phase control in suppressing the coherent background excited by the transfer pulses in spin-wave scheme, the sequence shown in Figure 7.19 (a) was applied without including the storage pulse. The background was measured after the second spin transfer pulse using a single photon counter, with and without the second electric field pulse.

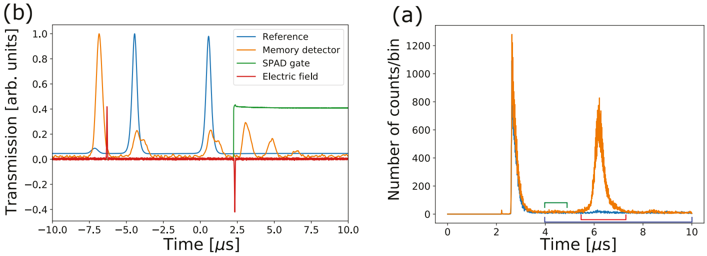

Figure 7.19: (a) Pulse sequence use for optical noise characterization of Stark-controlled spin-wave storage scheme. For the initial noise characterization the storage pulse was omitted, and only the two control pulses were used. See the legend for description of different traces. (b) Measured counts during a 10 μs detection window after the second control pulse with (blue) and without (orange) electric field pulses to switch off the coherent noise. The control pulses used were sechyp with a Rabi frequency of 1.53 MHz. The first spike is due to detector saturation effect. The peak centered at 6.2 μs is a two-pulse photon echo created by the two control pulses.

Figure 7.19 (b) shows the results of this experiment when a sechyp control pulse with a Rabi frequency of 1.53 MHz was used for excitation. The measured counts were accumulated over 25 000 shots. This Rabi frequency is required for an efficient spin transfer, and was used for the storage presented in Figure 7.16 (a). The blue (orange) trace represents the measured counts with (without) the electric field. The initial spike in both traces is due to detector saturation effect caused by the bright control pulse [4]. An unexpected strong coherent emission in the form of an echo can be seen at 6.2 μs. The timing at which it was emitted suggests that it was a two-pulse photon echo caused by reflection of the two control pulses by the cryostat window. This reflection propagates through the crystal along the forward direction (detection path), and excites the ions in the same manner as was described in Figure 4.7 leading to a strong coherent emission of a photon echo. This emission can be viewed as an additional noise source besides the ones mentioned earlier, and thus can be used to demonstrate the effectiveness of the Stark-control in suppressing the coherent noise.

The overall reduction in the background was measured by repeating the measurement in Figure 7.19 (b) using a range of Rabi frequencies in the control pulses. As the Rabi frequency increased, more ions were excited by the control pulses, which lead to an increase in the optical background. Figure 7.20 shows the result when comparing the total number of counts during the time win-

---

[4] The strong pulse creates electron-hole pairs in the detector before it is activated. These electron-hole pairs are then accelerated when the detector is activated leading to a spike in the number of counts for a short time.

dow 4 μs -10 μs (to exclude the effect of detector saturation), with and without the electric field pulses to switch off the coherent noise. A clear divergence can be seen between the two cases. For the largest Rabi frequency used, 1.53 MHz, the overall background was reduced by a factor of ~ 5.7. It should be noted that most of the reduction is due to effective suppressing of the two-pulse photon photon. To quantify the reduction of this echo by the electric field pulses, the total number of counts during the time interval [5.3 μs, 7.3 μs], when the echo was emitted, was measured and compared with and without electric field. The result is shown in Figure 7.21, where for the largest Rabi frequency used, the echo emission was attenuated by a factor of 13.5.

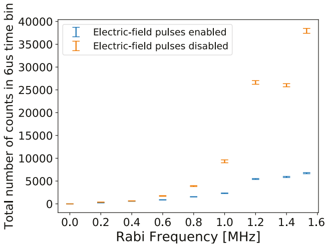

Figure 7.20. *Total number of counts for for control pulses with different Rabi frequencies, with (blue) and without (orange) electric field pulses. The counts were summed during the time period 4-10 μs of the detection window marked by a blue line in Figure 7.19 (b).*

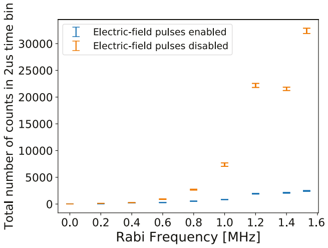

Figure 7.21. *Total number of counts for control pulses with different Rabi frequencies, with (blue) and without (orange) electric field pulses. The counts were summed over 2 μs during the time period 5.3μs to 7.3 μs, marked by the red line in Figure 7.19 (b).*

In order to estimate the reduction in other coherent background emitted by the ions remaining in and near the spectral pit only, we compared the total number of counts between 4 μs and 5 μs (To exclude the photon echo suppression) with and without application of the electric field pulses. A slight reduction of the noise can be seen in Figure 7.22 when an electric field pulse was applied for all used Rabi frequencies. For the largest Rabi frequency used, the background in this 1 μs time bin was reduced by a factor of 1.5 compared to no electric field.

Although the background was reduced at all Rabi frequencies used, thanks to the electric field pulses, it was still too high for single photon storage. An attempt to store weak coherent states with an average number of 10 photons per pulses was not successful, and the retrieved echo was dominated by optical background. The fact that the background was not affected by Stark phase switching suggests that most of the noise arises from an incoherent emission that can not be switched off by the presented technique. This emission is mostly fluorescence emitted by ions that were off-resonantly excited by the bright control pulses.

Noise reduction with a spectral hole filter

In order to mitigate the effect of the incoherent optical background arising from off-resonantly excited ions, a narrow-band spectral hole filter was added before the single-photon detector as was shown by the blow shaded box in Figure 7.14. The filter was based on spectral hole burning in a 12 mm long $Pr^{3+}:Y_2SiO_5$ crystal with a doping concentration of 500 ppm. The use of spectral hole filter to attenuate the noise in spin-wave storage has previously been used [20]. A readout of the 2 MHz wide hole created in the filter crystal is shown in Figure 7.23. The spectral hole filter was prepared at the same frequency as the that of the storage mode, which means that only light resonant with the storage mode will be transmitted. The rest of the light, such as the control pulses and fluorescence noise will be absorbed and attenuated by the ions out side the spectral hole.

The measurements presented in Figure 7.19 were repeated, with the filter added, using several Rabi frequencies for the control pulses. Figures 7.24 and 7.25 show the background detected during the 10 μs window and a 1 μs time bin, respectively, after the second control pulse with and without the application of electric field pulses. A clear reduction in the overall background can be seen in both cases compared to Figure 7.19 (b) where no spectral filter was used. This confirms the assumption that most of the noise arises from fluorescence emission by ions off-resonantly excited by the control pulses.

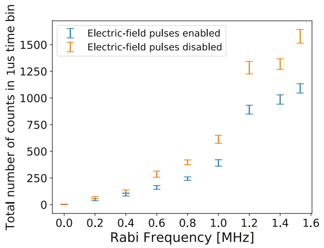

Figure 7.22. *Total number of counts for control pulses with different Rabi frequencies, with (blue) and without (orange) electric field pulses. The counts were summed over 1 μs during the time period 4 μs to 5 μs, marked by the red line in Figure 7.19 (b)*

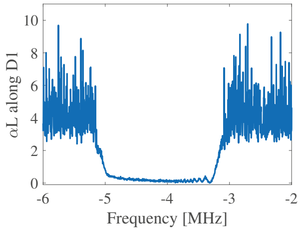

Figure 7.23. *Scanned readout of the 2 MHz optical filter using light polarized along the D_1 axis of the crystal.*

However, no obvious reduction in the background noise was observed when the electric field pulses were applied, compared to the case when no electric field was applied. This was somewhat surprising, given that some reduction was observed in the measurements performed without spectral hole filtering (Figure 7.20), although the noise was mostly from incoherent fluorescence emission. It was found that scattering of the control pulses from the crystal surface, cryostat windows, and the AMOS leaked into the filter crystal, which in turn excited the ions and lead to FID and fluorescence emission that leaked into the SPAD. Although attempts were made to overcome this by placing a gating AOM before the filter crystal and ensuring a clean polarization input into the filter crystal, it was not possible to completely remove this noise. This made it difficult to have a more rigorous evaluation the performance of our Stark phase control technique when combined with spin-wave storage.

Nevertheless, weak coherent states were successfully stored using the spin-wave scheme combined with Stark-control. The storage was repeated 5×10^5 times using an average of 0.1, 0.5, 1, 5, and 10 photons per pulse, and the SNR was evaluated in each case by comparing the total number of counts during the time when the echo was expected, to the counts during the same time without a storage input. The results from these measurements are shown in Figure 7.26. The SNR measured here for all inputs was less than that previously reported for a similar storage scheme in Pr^{3+}:Y_2SiO_5 in which Stark phase control was not employed [5] [20]. The higher background noise in the presented experiments is attributed to shortcomings in the optical setup, and not the performance of the Stark phase control itself.

---

[5] An additional difference in the experiment performed by Gündoğan *et al.* is that they propagated the control pulses at an angle relative to the storage pulses, leading to an extinction ratio of 10^{-5}. In our case, the spin transfer pulses and the storage pulse are counter propagating along the same axis, which makes the setup more susceptible to noise originating from back-scattering of the control pulses into the storage mode.

7.4.6 Fluorescence estimations and potential of scheme in other materials

Two attempts were made in the present work to combine Stark phase control with a spin-wave storage scheme for single photon-storage. In the first attempt, when no spectral hole filter was used, a slight reduction in coherent noise was demonstrated. The incoherent background emitted by ions in and outside the spectral pit was too high to perform single-photon storage with a sufficiently good SNR. In the second attempt, a spectral hole filter was used to attenuate the incoherent background. However, the filter crystal it self was a source of noise due to leakage of scattering of the control pulses from optical components into the filter crystal, creating coherent FID and incoherent fluorescence emission.

The results obtained in the first attempt show that Stark phase control can strongly suppress the coherent background, and thus has the potential to improve the SNR for single photon storage using a spin-wave scheme. The limiting factor for this technique is the fluorescence from off-resonant ex citations, which can not be switched off. In order to explore the potential of our technique, it would be useful to make an estimate of the fluorescence noise in other more suitable materials.

The source of the fluorescence emission is the off-resonant excitation of ions outside the spectral pit. To estimate the fluorescence noise, we look at the remaining absorption in an empty pit due to the Lorentzian tail of ions outside the pit. The total off-resonant absorption (α_c) at the center of a spectral pit can be written as [134]:

$$\alpha_c \sim \frac{2}{\pi}\frac{\Gamma_h}{\Delta}\alpha_0, \tag{7.5}$$

where Γ_h is the homogeneous linewidth of the ions, Δ is the width of the spectral pit, and α_0 is the absorption outside the pit. For a crystal of length L, and an input power P_{in}, the absorbed power (P_{abs}) by the off resonant ions can be written as:

$$P_{abs} = P_{in}[1 - e^{\alpha_c L}], \tag{7.6}$$

Equation 7.5 implies that materials with narrow homogeneous linewidth and in which wide spectral pits can be created are favourable to reduce the off-resonant excitation. From this perspective, Eu^{3+} is promising candidate material. Eu^{3+} has an optical homogeneous linewidth of 122 Hz in site 1, an excited state lifetime of 1.9 ms [59], and a branching ratio of $\sim 0.1\%$ to the 7F_0 zero phonon line. For a 1% doping concentration in Y_2SiO_5, the absorption depth of Eu^{3+} along the D_1 crystal axis is 3.9 cm^{-1} [18]. Using the equations above, it can be estimated that for a given input power, the part that will be off-resonantly absorbed by the ions outside a 40 MHz wide spectral pit in Eu^{3+} is $\sim$ 20 ppm

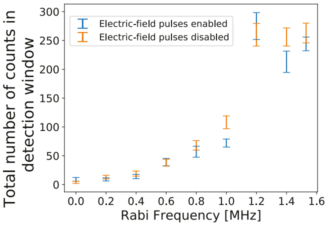

Figure 7.24. *Total number of counts during the 10 μs detection window for control pulses with different Rabi frequencies, with (blue) and without (orange) electric field pulses*

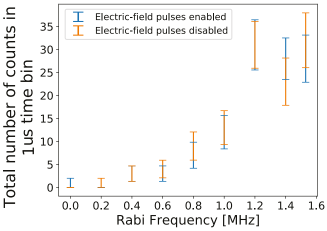

Figure 7.25. *Total number of counts for control pulses with different Rabi frequencies, with (blue) and without (orange) electric field pulses. The counts were summed over 1 μs time bin between 4.25 μs and 5.25 μs.*

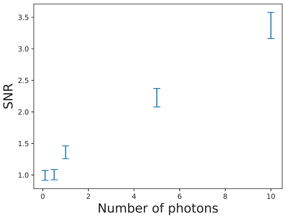

Figure 7.26. *SNR for weak coherent states input modes with different number of photons per storage pulse. The SNR was calculated by dividing the total number of signal photons in a 1.5 μs time bin, accumulated over 5×10^5 consecutive storage shots, by the noise floor, which is defined as the number of dark counts in a time bin of equivalent length, also accumulated over 5×10^5 consecutive shots*

of the input. Here we assume that all absorbed photons will be re-emitted as fluorescence. Out of the total isotropic fluorescence, only the part that is spatially overlapped with the echo emission contributes to the optical noise. If a diameter of 1 mm of the fluorescence light is collimated 20 cm after the crystal, this will be only 1 ppm of the total isotropic emission. In addition, since the fluorescence is emitted at different times given by the excited state lifetime, only photons emitted during the same time bin as the stored signal photon will contribute to the optical noise. If we look into a 1 μs time bin at the beginning of the fluorescence decay, the probability of photon emission will be $\sim 0.1\%$.

Assuming a 1 μs long control pulse with 100 mW power, the expected fluorescence noise emitted in a 1 μs time bin will be $\sim 10^{-5}$. With such low level on incoherent noise, our Stark-control technique can quench the other coherent noise emissions such FID and off-resonant echoes, allowing for single photon storage without the need for additional spectral filtering. It should be noted that the optical depth of Eu^{3+} used in the estimate above is too low, which could reduce the memory efficiency. However, this can be compensated for by a cavity to enhance the memory efficiency as have been demonstrated in Ref. [135].

7.5 Stark control of light

The Stark shift has been used previously in combination with spectral hole burning and the slow light effect to shift the frequency of an optical pulse, [109], and to compress a pulse in the time domain and control its group-velocity [110]. This section describes attempts to use the same effects to create an optical frequency splitter/combiner.

7.5.1 Frequency splitter

To understand how frequency splitter is achieved, we can consider a light pulse traveling through a narrow spectral hole. The group velocity, v_g, of the light in this case is defined as:

$$v_g = \frac{c}{n_g}, \tag{7.7}$$

where c is the speed of light, and n_g is the group refractive index, which is given by:

$$n_g = n + \omega \frac{\partial n}{\partial \omega}, \tag{7.8}$$

where n is the real part of the refractive index. The last term in Equation 7.8 is the dispersion, which can be tailored to control the group velocity of light traveling through the medium. In the

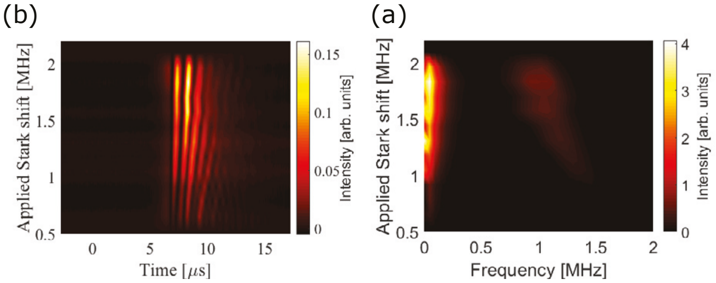

Figure 7.30: (a) Transmission through the crystal when applying multiple electric field across the crystal, showing the change in the period of the modulation, corresponding to change in the magnitude of frequency splitting. (b) Fourier transform of the light modulation shown in (a). The y-axis is the expected frequency splitting between the two pulses due to the applied Stark shift.

case of a narrow spectral hole, the dispersion is high, and consequently, the group velocity of light passing through the spectral hole is reduced compared to the speed of light in vacuum. Most of the energy of the slowed light is temporally stored in the ions that have a resonance frequency close to the spectral hole. If the dispersion is high enough, the whole energy of the pulse will be temporarily stored in the ions, and this is one of the requirements to create a frequency splitter. It is also necessary to isolate the ions that store the energy of the slowed light pulse from rest of the ions using spectral hole burning. Once the light pulse is absorbed by the isolated ions, a DC stark shift can be used to electrically manipulate them while the energy is still stored in them, which translates into a manipulation of the frequency of the light itself when it is re-emitted.

The principle of frequency splitter scheme is shown in Figure 7.27. The absorption structure consists of two isolated spectral ensembles of ions prepared in a wide spectral hole. The two ensembles (peaks) are spectrally separated from each other. A light pulse propagating through the center of the structure will be absorbed by the ions in the two peaks, given that the optical depth is high enough. After absorption, a DC electric field is applied across the crystal, the two electrically inequivalent ion classes in each peak, represented by red and blue in the figure, will be Stark shifted by a magnitude Δ in opposite directions, and so does the pulse energy stored in them. This gives rise to two pairs of peaks, formed by the same ion class and separated by frequency Δ, and when the light is re-emitted, it will be composed of two pulses with frequencies $\nu_0+\Delta$ and $\nu_0+\Delta$, where ν_0 is the frequency of the original pulse.

In order to experimentally demonstrate the frequency splitter,

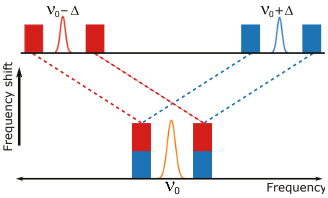

Figure 7.27. *An illustration of the frequency splitter. A light pulse with a central frequency* ν_0 *propagates through two spectrally isolated and separated peaks. A DC electric field is applied across the crystal after absorption, which split each peak into two electrically inequivalent ensembles (blue and red) that Stark shift in opposite directions by a magnitude* Δ*, giving rise to two pairs of peaks separated by* 2Δ*. When re-emitted, the light will contain two pulses with frequencies* $\nu_0+\Delta$ *and* $\nu_0+\Delta$*.*

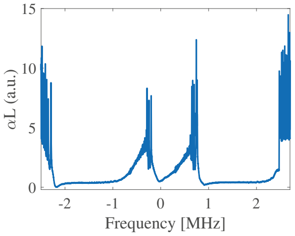

Figure 7.28. *Absorption of the spectral structure used for the frequency splitter experiments. The aim was to create a central hole that is 0.5 MHz wide, and two neighbouring peaks that are 0.5 MHz wide. Each of the side holes was 1.53 MHz wide. The peaks look narrower than expected and asymmetric, this is due to the high optical depth, makes it difficult to have a clear readout of the* αL *and the peak width. The peak width and the hole width are estimated from the frequency scans of the pulses used to create the structure.*

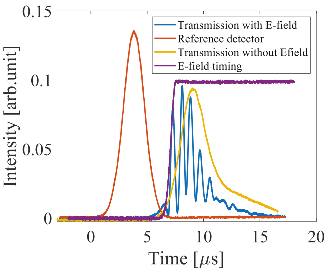

Figure 7.29. *The red line is a reference taken for a 2.2μs Gaussian pulse before it is sent to the crystal. The transmitted pulse through the 0.5 MHz spectral hole described in the main text is shown in yellow before applying the DC electric field, and in blue after applying the electric field. The purple line is the electric field in arbitrary unit. The light was delayed by ∼ 5.2 μs*

three optical holes separated by two 0.5 MHz wide peaks were created by optical pumping in the 10 mm crystal as shown in Figure 7.28. The central hole was 0.5 MHz wide, while the side holes were 1.53 MHz wide. The overall absorption structure is shown in Figure 7.28. A Gaussian pulse with FWHM =2.2 μs and a central frequency v_0 was sent through the central 0.5 MHz wide spectral hole. Due to the high dispersion, the light is slowed down, and get temporarily stored in the ions of the two neighboring 0.5 MHz wide peaks. Once the pulse was completely stored, a DC electric field was applied through the gold-coated electrodes across the b axis of the crystal. Figure 7.29 shows the transmitted Gaussian pulse before and after applying the electric field. In this case, the electric field applied was 4.9 V/cm, corresponding to a Stark shift of ± 590 kHz (the measured Stark coefficient was 121 kHz/(V/cm)). The beating of the frequency split pulse in this case is expected to be ∼ 1.2 MHz, and the beating frequency obtained from a Fourier transform of the measured signal was 1.27.

The results of this experiment are shown in Figure 7.30 for different magnitudes of the applied voltages. As the applied field was increased, the frequency splitting decreased. This is counter-intuitive, as a stronger field should split the two ion classes further away from each other, and should consequently lead to a greater frequency splitting of the light pulse stored in these ions. There two reasons that could explain this unexpected observation. First, the applied voltages were not high enough to completely separate the two pairs of peaks away from each other, and for most of the applied voltages, they peaks were overlapped. Second, the absorption structure, shown in Figure 7.28, was not suitable to demonstrate large frequency splittings because the side holes were relatively narrow. When larger Stark shifts are applied, the ions outside the structure shift towards the side holes and merge with the peaks in which the light is stored. Nevertheless, the frequency splitter scheme can be further optimized with a more sophisticated absorption structure preparation.

7.5.2 Frequency combiner

The frequency combiner is effectively the opposite of the beam splitter discussed above. The absorption structure used in this experiment, which is similar to that used for the frequency splitter, is shown in Figure 7.31. The optical input field was a Gaussian pulse with two frequency components (two-color pulse), $\nu_{\pm}$ separated by 1 MHz. The two color components were created using a single-pass AOM driven by a radio frequency (RF) signal containing two frequencies. Before the pulse reaches the crystal, a suitable DC electric field was applied across the b axis of the crystal. This has the effect of Stark-shifting the electrically inequivalent ion classes in both peaks by $\Delta = \pm$ 0.5 MHz, as shown by the orange trace in

Figure 7.31. The new shifted structure consists two 0.5 MHz wide holes, separated by 0.5 MHz wide peak, and flanked by two other 0.5 MHz wide peaks.

The two frequency components of the input pulse separated by 1 MHz, propagate along the crystal through the two central holes, also separated by 1 MHz. Provided the dispersion across the holes is sufficiently high, the energy of each frequency component will be stored in the ions located on sides of each of the central holes. Once the whole energy of the pulse has been stored inside the crystal, the applied electric field is switched off, leading to a recombination of the ± 0.5 MHz separated ion classes in each peak, and restoring the original absorption structure seen as the blue trace in Figure 7.31. As a result, when the light is re-emitted, its two frequency components $\nu_{\pm}$ become shifted by $\mp$ 0.5 MHz, giving a combined single frequency component as an output. Figure 7.32 shows the two-color pulse before (red) and after (blue) propagating through the combiner structure. The pulse has a FWHM of 2.5 μs, a duration of 15 μs, and $\Delta = 1$ MHz. Due to the relatively low dispersion, and the long pulse duration, the slow light effect was not sufficient for the pulse energy to be completely stored in the crystal at any time, so the light was not significantly affected by the applied electric field, and frequency combination was not achieved as expected. Nevertheless, an additional beating can be seen in the blue trace in Figure 7.32 just after switching off the DC electric field. This indicates that a third frequency component emerged and interfered with the two color pulse. More optimised experiments and analysis is needed to evaluate the potential of frequency combiner scheme.

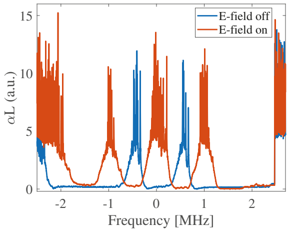

Figure 7.31. *Absorption structure used in the frequency combiner experiment.*

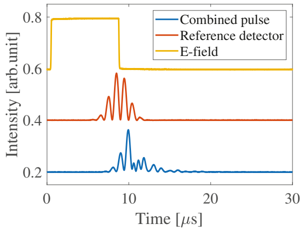

Figure 7.32. *Two color pulse with with 2.5μs FWHM and 15μs duration before (orange) and after (blue) propagating through the frequency combiner.*

7.5.3 FID switching

Stark phase control was used to switch off the FID, as was discussed in Section 7.4.4. This section describes an interesting phenomena that was observed when the FID is switched off and switched back on after a short time. An ensemble of ions with a FWHM of 450 kHz was burned back into the center of an 18 MHz wide optical pit, as shown in Figure 7.33. A Gaussian pulse with FWHM = 10 μs and a central frequency resonant with the peak was sent through the crystal. As the light propagates through the crystal, it is absorbed by the ions in the spectral peak, which, as a result, partially excite the ions into a superposition state, leading to an FID emission for a time given by the peak width. While the ions are emitting coherently, an electric field pulse, corresponding to a phase difference of π between the two electrically inequivalent ion classes, was applied across the crystal to switch-off the FID emission. After a short period, this was followed by a second identical electric field pulse to switch the FID emission back on. Figure 7.34 shows the results of these measurements. The time constant

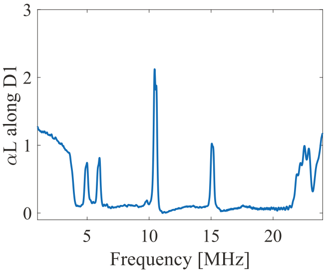

Figure 7.33. *Absorption structure of the peak used in the FID switching experiment. The 450 kHz wide peak was created by burning back ions resonant with the* $|3/2g\rangle \rightarrow |3/2e\rangle$ *transition. The relevant peak is centered at 10.5 MHz. The side peaks are created by the same burning sequence, and are irrelevant to the discussion.*

T_2 of the FID before switching was 6.7 μs, which suggests that the peak width was 475 kHz; close to the measured value from the absorption structure measurement shown in Figure 7.33. During the switching off period, the emission was effectively stopped, as can be seen by the dip in the green curve in Figure 7.34, but once the emission was switched back on and the ions re-phased, strong and rapidly decaying emission was observed. The decay time is much faster than the FID, which suggests that a different mechanism is causing the emission. In Ref. [136], Kalachev describes a similar system where an ensemble of ions in a collective superposition state are divided into two equal parts. A phase modulator introducing a phase shift of π between the two parts, converts it to a subradiant state, while when the phase difference is removed, it is converted to a superradiant state. More investigations and analysis are needed to fully describe the observed effect.

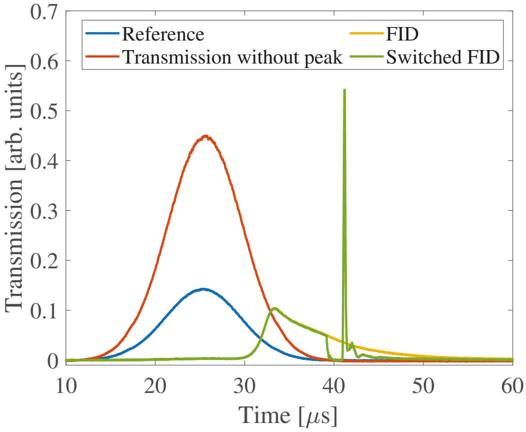

Figure 7.34: Switching of the FID using fast electric field pulses. The blue curve shows the reference light before propagating through the crystal, and the orange curve is transmission through an empty pit. The green curve shows the FID when an electric field pulse, introducing a phase difference of π between the two ion classes in the peak, is applied to switch off the FID at T = 40 μs, followed shortly by another electric field pulse to switch it back on. Strong emission can be seen as soon as the ions are back in phase, after the second electric field pulse was applied. The yellow line is light transmitted through the 450 kHz wide peak burned back into the pit where the FID can be seen.

APPENDIX A

CRYOSTATION FOR SECOND GENERATION MICROCAVITY

In order to preserve the coherence properties of the REIs, experiments must be carried out at liquid helium temperatures. In this work, an Oxford Instruments, liquid helium bath cryostat (Spectromag SM400) was used to cool the samples to 2.1 K temperature. Although this cryostat is adequate in terms of its cooling power, it was difficult to operate the microcavity setup in the cryostat, as the cavity setup had to be designed to fit in the limited sample space of the cryostat, which was 25 mm in diameter. This made it difficult to construct and operate a highly stable high finesse cavity that could be scanned in three dimensions.

At the beginning of my PhD studies, I surveyed the cryostats available in an attempt to find a suitable one in which the next-generation high-finesse microcavity could be operated. Apart from the microcavity experiments, the cryostat was also to be used for laser-frequency stabilization experiments, based on spectral hole burning [122]. The requirements of an optimal cryostat that could be used for both these applications are described below.

Temperature and cooling:

The system must be able to reach a base temperature of < 2 K with a cooling power of at least 10 mW in order to preserve the long coherence times of the REIs. The goal was to achieve this using a closed-cycle cryostat to ensure long operation time (several weeks) at a lower cost than the bath cryostat. It is generally difficult to achieve this base temperature by conductive cooling using closed-cycle cryostats. Direct cooling of the sample via an exchange gas is therefore preferable. Temperature stability of the sample, and temperature homogeneity around the sample are also critical for laser-frequency stabilization experiments. A system with high temperature stability, on the order of 1 mK over an hour at base temperature, and with a homogeneity onn the order of 10 mK across the sample chamber is therefore desirable.

Sample space:

Adequate sample space is necessary to ensure flexibility in the design of a high/ finesse microcavity with high passive stability, and the possibility of scanning it in along three axes. A minimum diameter of 50 mm, and a minimum height of 100 mm were deemed suitable. Furthermore, the sample chamber must be accessible with an optical fiber, and must have optical windows for transmission experiments. DC and RF electrical connections to the sample are also necessary for both types of experiment.

Sample mounting platform and stability:

Mechanical stability is also important for both the microcavity and the laser-frequency stabilization experiments. For example, in order to operate a microcavity with a finesse on the order of 10^5, the stability in cavity length should be on the order of 1 pm. This requires a highly stable mounting platform. Our aim was to have a system in which the vibration is less than 10 nm RMS. Furthermore, since the cryostat was to be used in two different experiments, a mounting platform that allows for easy and rapid exchange between the two setups in the cryostat, without having to disassemble the setups, was desirable.

While some of these requirements can be satisfied separately, combining all of them in the same system has proven to be challenging. Therefore, a custom made cryostat was designed and built by MyCryoFirm, based on our experimental requirements. A cross-sectional view of the CAD model of the system highlighting the main components is shown in Figure A.1. In order to reach to a base temperature of 2 K, the system was equipped with an oil-free, continuous flow loop of helium gas, which allows for liquefaction of helium in the 1 K pot (9) in the Figure A.1. In order to have the option of direct cooling of the sample via an exchange gas, an inner gas cell was constructed and mounted on top of the 1 K pot. The cell, shown in Figure A.2, is equipped with removable top flanges on which different experimental setups can be mounted. The flange on which the setup is mounted can be removed out of the cryostat through an ISO-K 100 port on the side of the outer vacuum chamber. The cell itself and the bottom part of the flange were made of CuETP copper to ensure high thermal conductivity and low temperature gradients across the cell. The cell is mounted inside a superconducting magnet which is capable of supplying a magnetic field of up to 2 T.

After the installation of the cryostat, several tests were performed to verify that it fulfilled the requirements. Figure A.3 shows cooling of the system from room temperature to a base

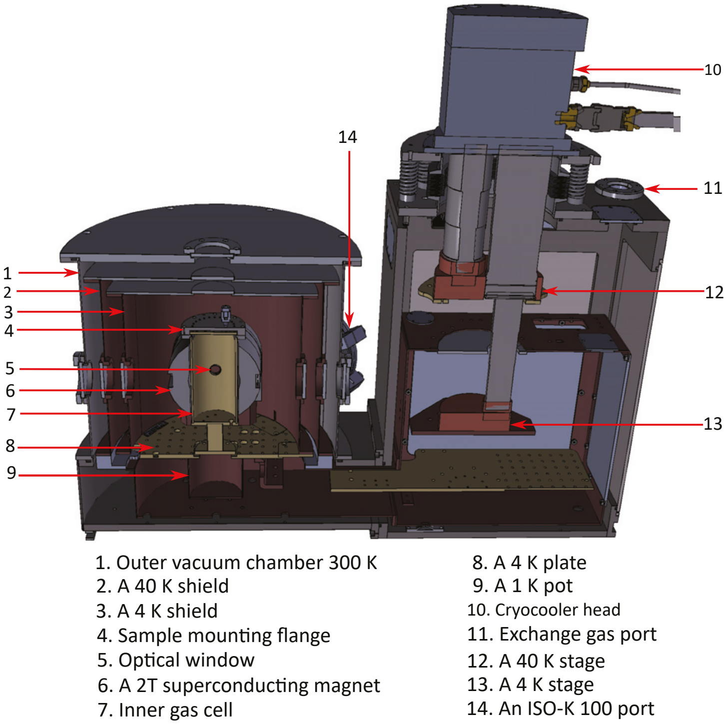

Figure A.1: CAD model of the cryostat showing the cryocooler (righ), and the experimental chamber (left). The main components are described under the figure. (courtesy of MyCryoFirm)

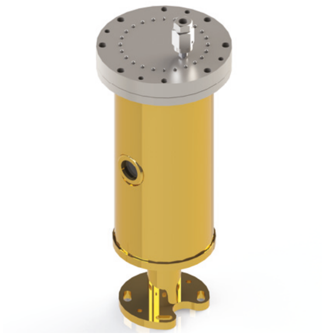

Figure A.2. *The inner gas cell with the top flange on which the setups are mounted. (Courtesy of MyCryoFirm)*

temperature of 1.25 K under 30 hours. Furthermore, the stability and homogeneity of the temperature were measured in the inner cell and in the 4 K plate under various conditions. The achieved values are given in Table A.1. Figures A.4 and A.5 show the cooling power measured at several temperatures for the inner cell and the 4 K plate, respectively. These measurements were made with a PID-controlled heater for active temperature stabilization.

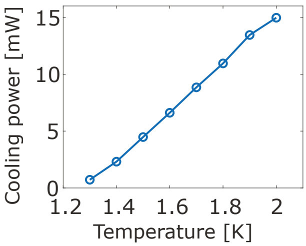

Figure A.4. *Cooling power measured at the inner cell with the following PID parameters: P=1, I=6, D=1.*

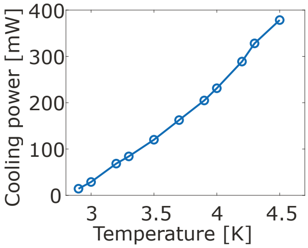

Figure A.5. *Cooling power measured at the 4 K plate with the following PID parameters: P=0.1, I=6, D=1.*

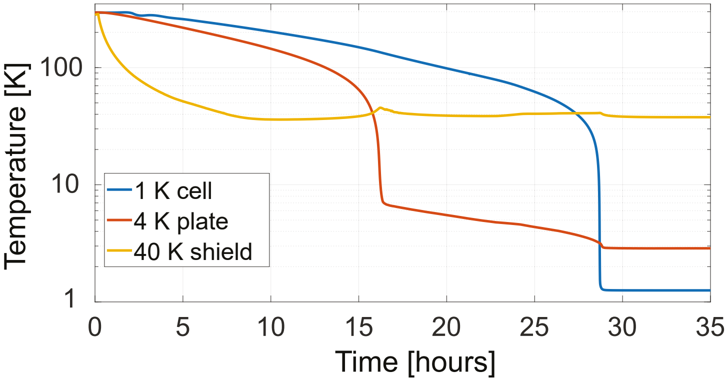

Figure A.3: A typical cooling of the cryostat showing the temperature of the 1 K cell (blue), the 4 K plate (red),and the 40 K shield (yellow), as a function of time. This was the first successful cooling of the cryostat after installation.

Measurement description	**Test result**
Base temperature of 4 K plate	2.8 K
Base temperature of the inner cell	1.25 K
Temperature stability on the 4 K plate at base temperature over an hour with (without) regulation	50 μK (0.9 mK) RMS
Temperature stability on the inner cell at base temperature over an hour with (without) regulation	3 μK (50 μK) RMS
Temperature homogeneity across the inner cell (between top and bottom plates of cell) for thermal power $<$ 4 mW	18 mK
Temperature rise on the 4 K plate during slow (fast) sweep of the magnetic field from 2T to -2T	90 mK (270 mK)
Temperature rise on the inner cell during slow (fast) sweep of the magnetic field from 2T to -2T	20 mK (82 mK)
Mechanical vibration measured on the 4 K plate	8.5 nm RMS

Table A.1: Initial tests performed after cryostat installation. The temperature homogeneity across the inner cell was measured in the factory before installation.

COMMENTS ON THE PAPERS

I **Optical coherence properties of nanoscale Kramers' rare-earth ions for quantum applications**
Mohammed K. Alqedra*, Chetan Deshmukh*, Sebastian P. Horvath, Safi Rafie-Zinedine, Abdullah Abdelatief, Lars Rippe, Stefan Kröll, Andreas Walther, Bernardo Casabone, Hugues de Riedmatten, Diana Serrano, Shuping Liu, Alban Ferrier, Alexandre Tallaire, Hugues de Riedmatten, and Philippe Goldner;
(*Authors contributed equally).
Manuscript in preparation.

The spectroscopic properties of erbium and neodymium ions in Y_2O_3 nanocrystals were investigated. The lifetime and inhomogeneous line of the two ions were measured at 2.17 K. The coherence properties of both ions were also investigated at different temperatures to identify the dephasing mechanisms. Based on, two quantum applications were proposed in which the investigated Nd^{3+} and Er^{3+} ions, doped in nanocrystals, would perform well: single qubit state readout and as a Fourier-limited single photon source.
I prepared and performed the experiments carried out on the Nd^{3+} ion and analysed the data, the ICFO group performed the experiments and analysis on Er^{3+}, and Paris group provided the nanocrystals and performed the initial material characterisation. Chetan Deshmukh and I wrote the manuscript together.

II **Noise-free on-demand atomic frequency comb quantum memory**
Sebastian P. Horvath*, Mohammed K. Alqedra*, Adam Kinos, Andreas Walther, Jan Marcus Dahlström, Stefan Kröll, and Lars Rippe;
(*Authors contributed equally).
Phys. Rev. Research **3**, 023099 (2021).

An extension of the atomic frequency comb protocol that utilizes the Stark effect to perform noise-free, on-demand control was demonstrated. Experiments were performed with both bright pulses and weak-coherent states. An unprecedented signal-to-noise ratio of 570 ± 120 was achieved using input pulses with an average photon number of ∼0.1. An established model was asapted to investigate an on-demand, wide-bandwidth quantum memory based on Eu^{3+}:$\mathrm{Y_2SiO_5}$ that could achieve a storage time as long as 100 μs without recourse to spin-wave storage.
I prepared and performed all experiments together with Sebastian Horvath, I performed the simulations, and I was involved in the discussions about the analysis. I contributed to the writing of the manuscript.

III **Stark control of solid-state quantum memory with spin-wave storage**
Mohammed K. Alqedra, Sebastian P. Horvath, Adam Kinos, Andreas Walther, Stefan Kröll, and Lars Rippe..
Manuscript in preparation.

In this paper, the Stark effect was combined with the spin-wave storage scheme, and a coherent control of the stored pulse was experimentally demonstrated. It was also shown this technique can be used to turns off the free induction decay of a narrow ensemble of ions, and can thus improve the noise performance of spin-wave storage at the single-photon level by quenching coherent optical noises created by the strong control pulses.
I prepared and performed all experiments together with Sebastian Horvath, we both did the data analysis, and I wrote the manuscript.

ACKNOWLEDGEMENTS

First, I would like to thank my main supervisor, Andreas Walther, for his continuous support, encouragement, and patience, and for always being available for discussions. I am grateful for the freedom I was given to follow my interests. I would also like to thank my co-supervisor, Stefan Kröll, for always being there to help and discuss, and for creating a nice atmosphere in the group. I thank Lars Rippe for giving me the opportunity to work on the quantum memory project, and for always coming up with interesting ideas and enlightening discussions. I thank Adam Kinos for his help and innate ability to explain and demystify physics.

I am thankful to the current members of the quantum information group, Alexander Bengtsson, Hafsa Syed, David Hill, David Gustavsson, Abdullah Abdelatief, Marcus Lindén, Kevin Shortiss, and Safi Rafie-Zinedine, for contributing to a friendly working environment, for the lunches, the coffee breaks, and for their help in the lab. I am also thankful to the former group members, especially Sebastian Horvath, for always being generous in sharing his expertise, wether it is about physics or about life, and for his great help in getting various experiments working during his time in the group. I thank Qian Li and Chunyan Shi for being friendly and helpful, Vassily Kornienko for helping out with the fiber machining. I also want to thank the students whom I have helped supervise: André Nüßlein for his efforts in the designing phase of the cavity, and Jannek Hansen for his efforts and discussions about cavity locking.

I am also grateful to to the international collaborators whom I have had the pleasure to work with: David Hunger and his group members, especially Timon Eichhorn, Maximilian Pallmann, and Larissa Kohler, for allowing me to use their resources to machine the fibers, and for the valuable discussions and help. In addition, I would like to thank Philipe Goldner and Diana Serrano for providing the nanorcrystals investigated in this work and for the initial characterizations, Hugues de Riedmatten and Chetan Deshmukh, for collaborating with the spectroscopy manuscript and for the useful discussions about the cavity project.

I am thankful to Michael Meyer and Håkan Ivansson for their help in machining many mechanical components used in this work, Leif Magnusson for providing us with liquid helium at the beginning of my PhD, and Romain Goncalves for continuing the helium supply.

I am grateful to other people in the Atomic Physics Division for helping out with more specific things, Nina Reistad and Anders Persson for letting me borrow their equipment, Anne Petersson-Jungbeck for assisting with the administrative issues, Jakob tested and Maria Algotsson for helping with the financial issues, Åke Johansson for taking care of all computer related issues, and the rest of the division members for creating a nice work environment.

I would like to express my deepest gratitude for my beloved parents, Noura and Kamal, for their unwavering support and encouragements all the time, regardless of the circumstances. To my family and friends, and all those who have supported me during my studies, thank you.

REFERENCES

1. R. P. Feynman. *Simulating physics with computers.* Int. J. Theor. Phys. **21**, 467–488 (1982).
2. P. Shor. *Algorithms for quantum computation: discrete logarithms and factoring.* In *Proceedings 35th Annual Symposium on Foundations of Computer Science* pages 124–134 (1994).
3. P. W. Shor. *Polynomial-Time Algorithms for Prime Factorization and Discrete Logarithms on a Quantum Computer.* SIAM Rev. **41**, 303–332 (1999).
4. L. Rolf. *Is quantum mechanics useful?* Philosophical Transactions of the Royal Society of London. Series A: Physical and Engineering Sciences **353**, 367–376 (1995).
5. S. Haroche and J.-M. Raimond. *Quantum Computing: Dream or Nightmare?* Phys. Today **49**, 51–54 (1996).
6. P. W. Shor. *Scheme for reducing decoherence in quantum computer memory.* Phys. Rev. A **52**, R2493–R2496(R) (1995).
7. A. M. Steane. *Error Correcting Codes in Quantum Theory.* Phys. Rev. Lett. **77**, 793–797 (1996).
8. M. Zhong, M. P. Hedges, R. L. Ahlefeldt, J. G. Bartholomew, S. E. Beavan, S. M. Wittig, J. J. Longdell and M. J. Sellars. *Optically addressable nuclear spins in a solid with a six-hour coherence time.* Nature **517**, 177–180 (2015).
9. L. Rippe, B. Julsgaard, A. Walther, Y. Ying and S. Kröll. *Experimental quantum-state tomography of a solid-state qubit.* Phys. Rev. A **77**, 022307 (2008).
10. D. P. DiVincenzo. *The Physical Implementation of Quantum Computation.* Fortschr. Phys. **48**, 771–783 (2000).
11. A. I. Lvovsky, B. C. Sanders and W. Tittel. *Optical quantum memory.* Nat. Photonics **3**, 706–714 (2009).
12. E. Knill, R. Laflamme and G. J. Milburn. *A scheme for efficient quantum computation with linear optics.* Nature **409**,

46–52 (2001).

13. P. Kok, W. J. Munro, K. Nemoto, T. C. Ralph, J. P. Dowling and G. J. Milburn. *Linear optical quantum computing with photonic qubits.* Rev. Mod. Phys. **79**, 135–174 (2007).

14. H.-J. Briegel, W. Dür, J. I. Cirac and P. Zoller. *Quantum Repeaters: The Role of Imperfect Local Operations in Quantum Communication.* Phys. Rev. Lett. **81**, 5932–5935 (1998).

15. G. H. Dieke and H. M. Crosswhite. *The Spectra of the Doubly and Triply Ionized Rare Earths.* Appl. Opt. **2**, 675–686 (1963).

16. W. T. Carnall, G. L. Goodman, K. Rajnak and R. S. Rana. *A systematic analysis of the spectra of the lanthanides doped into single crystal LaF3.* J. Chem. Phys. **90**, 3443–3457 (1989).

17. R. Withnall and J. Silver. *Physics of Light Emission from Rare-Earth Doped Phosphors* pages 1019–1028. Springer Berlin Heidelberg Berlin, Heidelberg (2012). ISBN 978-3-540-79567-4.

18. F. Könz, Y. Sun, C. W. Thiel, R. L. Cone, R. W. Equall, R. L. Hutcheson and R. M. Macfarlane. *Temperature and concentration dependence of optical dephasing, spectral-hole lifetime, and anisotropic absorption in* Eu^{3+}: $\mathrm{Y_2SiO_5}$. Phys. Rev. B **68**, 085109 (2003).

19. M. Afzelius, I. Usmani, A. Amari, B. Lauritzen, A. Walther, C. Simon, N. Sangouard, J. Minář, H. de Riedmatten, N. Gisin and S. Kröll. *Demonstration of Atomic Frequency Comb Memory for Light with Spin-Wave Storage.* Phys. Rev. Lett. **104**, 040503 (2010).

20. M. Gündoğan, P. M. Ledingham, K. Kutluer, M. Mazzera and H. de Riedmatten. *Solid State Spin-Wave Quantum Memory for Time-Bin Qubits.* Phys. Rev. Lett. **114**, 230501 (2015).

21. M. Nilsson, L. Rippe, S. Kröll, R. Klieber and D. Suter. *Hole-burning techniques for isolation and study of individual hyperfine transitions in inhomogeneously broadened solids demonstrated in* Pr^{3+}: $\mathrm{Y_2SiO_5}$. Phys. Rev. B **70**, 214116 (2004).

22. R. M. Macfarlane. *Inhomogeneous broadening of spectral lines in doped insulators.* J. Lumin. **45**, 1–5 (1990).

23. R. Hull, J. Parisi, H. Warlimont, G. Liu and B. Jacquier. *Spectroscopic Properties of Rare Earths in Optical Materials.* Springer Berlin, Germany (2005).

24. C. J. Foot and D. Of Physics Christopher J. Foot. *Atomic Physics.* OUP Oxford, England, UK (2005). ISBN 978-0-19850695-9. URL `https://books.google.se/books/`

about/Atomic_Physics.html?id=_CoSDAAAQBAJ&redir_esc=y.

25. A. Reiserer and G. Rempe. *Cavity-based quantum networks with single atoms and optical photons.* Rev. Mod. Phys. **87**, 1379–1418 (2015). URL https://link.aps.org/doi/10.1103/RevModPhys.87.1379.
26. S. J. van Enk and H. J. Kimble. *Single atom in free space as a quantum aperture.* Phys. Rev. A **61**, 051802 (2000).
27. M. K. Tey, Z. Chen, S. A. Aljunid, B. Chng, F. Huber, G. Maslennikov and C. Kurtsiefer. *Strong interaction between light and a single trapped atom without the need for a cavity.* Nat. Phys. **4**, 924–927 (2008).
28. G. Leuchs and M. Sondermann. *Light–matter interaction in free space.* J. Mod. Opt. **60**, 36–42 (2013).
29. M. Fox. *Quantum Optics : An Introduction.* Oxford University Press Oxford, England, UK (2006). ISBN 978-0-19856673-1.
30. S. Haroche and J.-M. Raimond. *Exploring the Quantum: Atoms, Cavities, and Photons.* OUP Oxford, England, UK (2006). ISBN 978-0-19850914-1.
31. G. S. Agarwal. *Quantum Optics.* Cambridge University Press Cambridge, England, UK (2012). ISBN 978-1-13903517-0.
32. J. Weiner and P.-T. Ho. *Light-Matter Interaction: Fundamentals and Applications.* Wiley (2003). ISBN 978-0-47125377-8.
33. R. J. Thompson, G. Rempe and H. J. Kimble. *Observation of normal-mode splitting for an atom in an optical cavity.* Phys. Rev. Lett. **68**, 1132–1135 (1992). URL https://link.aps.org/doi/10.1103/PhysRevLett.68.1132.
34. E. M. Purcell. *Proceedings of the American Physical Society.* Phys. Rev. **69**, 681 (1946). URL https://link.aps.org/doi/10.1103/PhysRev.69.674.2.
35. P. Goy, J. M. Raimond, M. Gross and S. Haroche. *Observation of Cavity-Enhanced Single-Atom Spontaneous Emission.* Phys. Rev. Lett. **50**, 1903–1906 (1983). URL https://link.aps.org/doi/10.1103/PhysRevLett.50.1903.
36. E. A. Hinds. *Cavity Quantum Electrod Ynamics.* In *Advances In Atomic, Molecular, and Optical Physics* volume 28 pages 237–289. Academic Press Cambridge, MA, USA (1990).
37. K. J. Vahala. *Optical microcavities.* Nature **424**, 839–846 (2003).
38. T. Zhong, J. M. Kindem, J. G. Bartholomew, J. Rochman,

I. Craiciu, V. Verma, S. W. Nam, F. Marsili, M. D. Shaw, A. D. Beyer and A. Faraon. *Optically Addressing Single Rare-Earth Ions in a Nanophotonic Cavity.* Phys. Rev. Lett. **121**, 183603 (2018). URL `https://link.aps.org/doi/10.1103/PhysRevLett.121.183603`.

39. J. M. Kindem, A. Ruskuc, J. G. Bartholomew, J. Rochman, Y. Q. Huan and A. Faraon. *Control and single-shot readout of an ion embedded in a nanophotonic cavity.* Nature **580**, 201–204 (2020).

40. A. Ruskuc, C.-J. Wu, J. Rochman, J. Choi and A. Faraon. *Nuclear spin-wave quantum register for a solid-state qubit.* Nature **602**, 408–413 (2022).

41. A. M. Dibos, M. Raha, C. M. Phenicie and J. D. Thompson. *Atomic Source of Single Photons in the Telecom Band.* Phys. Rev. Lett. **120**, 243601 (2018). URL `https://link.aps.org/doi/10.1103/PhysRevLett.120.243601`.

42. M. Raha, S. Chen, C. M. Phenicie, S. Ourari, A. M. Dibos and J. D. Thompson. *Optical quantum nondemolition measurement of a single rare earth ion qubit.* Nat. Commun. **11**, 1–6 (2020).

43. S. Chen, M. Raha, C. M. Phenicie, S. Ourari and J. D. Thompson. *Parallel single-shot measurement and coherent control of solid-state spins below the diffraction limit.* Science **370**, 592–595 (2020).

44. K. Xia, K. Xia, F. Sardi, F. Sardi, C. Sauerzapf, T. Kornher, H.-W. Becker, Z. Kis, L. Kovacs, D. Dertli, J. Foglszinger, R. Kolesov, J. Wrachtrup and J. Wrachtrup. *Tunable microcavities coupled to rare-earth quantum emitters.* Optica **9**, 445–450 (2022).

45. D. V. Strekalov, C. Marquardt, A. B. Matsko, H. G. L. Schwefel and G. Leuchs. *Nonlinear and quantum optics with whispering gallery resonators.* J. Opt. **18**, 123002 (2016).

46. D. S. Norman, F. Azeem, J. J. Longdell and H. G. L. Schwefel. *Measuring optical loss in yttrium orthosilicate using a whispering gallery mode resonator.* Mater. Quantum Technol. **2**, 011001 (2022).

47. K. Xia, F. Sardi, C. Sauerzapf, T. Kornher, H.-W. Becker, Z. Kis, L. Kovacs, R. Kolesov and J. Wrachtrup. *High-Speed Tunable Microcavities Coupled to Rare-Earth Quantum Emitters.* arXiv (2021).

48. D. Hunger, T. Steinmetz, Y. Colombe, C. Deutsch, T. W. Hänsch and J. Reichel. *A fiber Fabry–Perot cavity with high finesse.* New J. Phys. **12**, 065038 (2010).

49. D. Hunger, C. Deutsch, R. J. Barbour, R. J. Warburton and J. Reichel. *Laser micro-fabrication of concave, low-roughness features in silica.* AIP Adv. **2**, 012119 (2012).

50. M. Mader, J. Reichel, T. W. Hänsch and D. Hunger. *A scanning cavity microscope - Nature Communications.* Nat. Commun. **6**, 1–7 (2015).

51. B. Merkel, A. Ulanowski and A. Reiserer. *Coherent and Purcell-Enhanced Emission from Erbium Dopants in a Cryogenic High-Q Resonator.* Phys. Rev. X **10**, 041025 (2020).

52. A. Kinos, D. Hunger, R. Kolesov, K. Mølmer, H. de Riedmatten, P. Goldner, A. Tallaire, L. Morvan, P. Berger, S. Welinski, K. Karrai, L. Rippe, S. Kröll and A. Walther. *Roadmap for Rare-earth Quantum Computing.* arXiv (2021).

53. J. H. Wesenberg, K. Mølmer, L. Rippe and S. Kröll. *Scalable designs for quantum computing with rare-earth-ion-doped crystals.* Phys. Rev. A **75**, 012304 (2007).

54. A. Walther, L. Rippe, Y. Yan, J. Karlsson, D. Serrano, A. N. Nilsson, S. Bengtsson and S. Kröll. *High-fidelity readout scheme for rare-earth solid-state quantum computing.* Phys. Rev. A **92**, 022319 (2015).

55. K. Debnath, A. H. Kiilerich and K. Mølmer. *Ancilla-mediated qubit readout and heralded entanglement between rare-earth dopant ions in crystals.* Phys. Rev. A **103**, 043705 (2021).

56. Y. Yan. *Towards single Ce ion detection in a bulk crystal for the development of a single-ion qubit readout scheme.* PhD thesis Lund University (2013). URL `https://lup.lub.lu.se/search/files/3632686/4072077.pdf`.

57. Y. Yan, J. Karlsson, L. Rippe, A. Walther, D. Serrano, D. Lindgren, M.-e. Pistol, S. Kröll, P. Goldner, L. Zheng and J. Xu. *Measurement of linewidths and permanent electric dipole moment change of the Ce $4f$-5d transition in Y_2SiO_5 for qubit readout scheme in rare-earth ion based quantum computing.* Phys. Rev. B **87**, 184205 (2013).

58. J. Karlsson. *Cerium as a quantum state probe for rare-earth qubits in a crystal.* PhD thesis Atomic Physics (2015).

59. R. W. Equall, Y. Sun, R. L. Cone and R. M. Macfarlane. *Ultraslow optical dephasing in* Eu^{3+}:$\mathrm{Y_2SiO_5}$. Phys. Rev. Lett. **72**, 2179–2182 (1994).

60. R. W. Equall, R. L. Cone and R. M. Macfarlane. *Homogeneous broadening and hyperfine structure of optical transitions in* Pr^{3+}:$\mathrm{Y_2SiO_5}$. Phys. Rev. B **52**, 3963–3969 (1995).

61. G. Heinze, C. Hubrich and T. Halfmann. *Stopped Light and Image Storage by Electromagnetically Induced Transparency*

up to the Regime of One Minute. Phys. Rev. Lett. **111**, 033601 (2013).

62. D. Serrano, Y. Yan, J. Karlsson, L. Rippe, A. Walther, S. Kröll, A. Ferrier and P. Goldner. *Impact of the ion–ion energy transfer on quantum computing schemes in rare-earth doped solids*. J. Lumin. **151**, 93–99 (2014).
63. B. M. Walsh, J. M. McMahon, W. C. Edwards, N. P. Barnes, R. W. Equall and R. L. Hutcheson. *Spectroscopic characterization of Nd:Y2O3: application toward a differential absorption lidar system for remote sensing of ozone*. J. Opt. Soc. Am. B, JOSAB **19**, 2893–2903 (2002).
64. Y. Sun, C. W. Thiel, R. L. Cone, R. W. Equall and R. L. Hutcheson. *Recent progress in developing new rare earth materials for hole burning and coherent transient applications*. J. Lumin. **98**, 281–287 (2002).
65. M. J. Sellars, E. Fraval and J. J. Longdell. *Investigation of static electric dipole–dipole coupling induced optical inhomogeneous broadening in Eu3+:Y2SiO5*. J. Lumin. **107**, 150–154 (2004).
66. D. Serrano, J. Karlsson, L. Zheng, Y. Dong, A. Ferrier, P. Goldner, A. Walther, L. Rippe and S. Kröll. *Satellite line mapping in Eu3+–Ce3+ and Pr3+–Ce3+ codoped Y2SiO5*. J. Lumin. **170**, 102–107 (2016).
67. B. Casabone, J. Benedikter, T. Hümmer, F. Oehl, K. de Oliveira Lima, T. W. Hänsch, A. Ferrier, P. Goldner, H. de Riedmatten and D. Hunger. *Cavity-enhanced spectroscopy of a few-ion ensemble in Eu3+:Y2O3*. New J. Phys. **20**, 095006 (2018).
68. A. Khalid, K. Chung, R. Rajasekharan, D. W. M. Lau, T. J. Karle, B. C. Gibson and S. Tomljenovic-Hanic. *Lifetime Reduction and Enhanced Emission of Single Photon Color Centers in Nanodiamond via Surrounding Refractive Index Modification*. Sci. Rep. **5**, 1–12 (2015).
69. I. D. Abella, N. A. Kurnit and S. R. Hartmann. *Photon Echoes*. Phys. Rev. **141**, 391–406 (1966).
70. C. W. Thiel, N. Sinclair, W. Tittel and R. L. Cone. *Optical decoherence studies of* $\mathrm{Tm}^{3+}:\mathrm{Y}_3\mathrm{Ga}_5\mathrm{O}_{12}$. Phys. Rev. B **90**, 214301 (2014).
71. R. M. Macfarlane. *High-resolution laser spectroscopy of rare-earth doped insulators: a personal perspective*. J. Lumin. **100**, 1–20 (2002).
72. D. Serrano, C. Deshmukh, S. Liu, A. Tallaire, A. Ferrier, H. de Riedmatten and P. Goldner. *Coherent optical and spin*

spectroscopy of nanoscale $\mathrm{Pr}^{3+}: \mathrm{Y}_2\mathrm{O}_3$. Phys. Rev. B **100**, 144304 (2019).

73. F. R. Graf, A. Renn, G. Zumofen and U. P. Wild. *Photon-echo attenuation by dynamical processes in rare-earth-ion-doped crystals.* Phys. Rev. B **58**, 5462–5478 (1998).

74. F. Rochau, I. Sánchez Arribas, A. Brieussel, S. Stapfner, D. Hunger and E. M. Weig. *Dynamical Backaction in an Ultrahigh-Finesse Fiber-Based Microcavity.* Phys. Rev. Appl. **16**, 014013 (2021).

75. W. R. Babbitt, A. Lezama and T. W. Mossberg. *Optical dephasing, hyperfine structure, and hyperfine relaxation associated with the 580.8-nm* $^7\mathrm{F}_0$–$^5\mathrm{D}_0$ *transition of europium in* Eu^{3+}*:*$\mathrm{Y}_2\mathrm{O}_3$. Phys. Rev. B **39**, 1987–1992 (1989).

76. R. M. MacFarlane and R. M. Shelby. *Homogeneous line broadening of optical transitions of ions and molecules in glasses.* J. Lumin. **36**, 179–207 (1987).

77. Cryogenics - Property Graphing/Integrating Tool (2020). URL `https://trc.nist.gov/cryogenics/calculators/graphcalc.html`. [Online; accessed 11. Mar. 2022].

78. Attocube. *User Manual - Premium line Positioners & Scanners.* Attocube (2021).

79. M. Mader. *A scanning cavity microscope.* PhD thesis Ludwig-Maximilians-Universität München (2018). URL `https://edoc.ub.uni-muenchen.de/22946`.

80. H. S. Kaupp. *Coupling nitrogen-vacancy centers in diamond to fiber-based Fabry-Pérot microcavities.* PhD thesis Ludwig-Maximilians-Universität München (2017). URL `https://edoc.ub.uni-muenchen.de/21449`.

81. J. Benedikter. *Microcavity Enhancement of Silicon Vacancy Centers in Diamond and Europium Ions.* PhD thesis Ludwig-Maximilians-Universität München (2019). URL `https://pure.mpg.de/pubman/faces/ViewItemOverviewPage.jsp?itemId=item_3212955`.

82. T. Hümmer. *Cavity-enhanced Hyperspectral Raman and Absorption Microscopy.* LMU München (2019). URL `https://pure.mpg.de/pubman/faces/ViewItemOverviewPage.jsp?itemId=item_3213010_1`.

83. J. Hansen. Active stabilisation of a micro-sized fibre cavity using tilt locking to enable quantum operations on single ions (2021). Student Paper.

84. E. D. Black. *An introduction to Pound–Drever–Hall laser frequency stabilization.* Am. J. Phys. **69**, 79 (2000).

85. D. A. Shaddock, M. B. Gray and D. E. McClelland. *Frequency locking a laser to an optical cavity by use of spatial mode interference.* Opt. Lett. **24**, 1499–1501 (1999).

86. L. Neuhaus, R. Metzdorff, S. Chua, T. Jacqmin, T. Briant, A. Heidmann, P.-F. Cohadon and S. Deléglise. *PyRPL (Python Red Pitaya Lockbox) — An open-source software package for FPGA-controlled quantum optics experiments.* In *2017 Conference on Lasers and Electro-Optics Europe European Quantum Electronics Conference (CLEO/Europe-EQEC)* pages 1–1 (2017).

87. M. M. Wind, J. Vlieger and D. Bedeaux. *The polarizability of a truncated sphere on a substrate I.* Physica A **141**, 33–57 (1987).

88. G. Beadie, M. Brindza, R. A. Flynn, A. Rosenberg and J. S. Shirk. *Refractive index measurements of poly(methyl methacrylate) (PMMA) from 0.4–1.6 μm.* Appl. Opt. **54**, F139–F143 (2015).

89. R. J. Gaboriaud, F. Pailloux, P. Guerin and F. Paumier. *Yttrium oxide thin films, Y2O3, grown by ion beam sputtering on.* J. Phys. D: Appl. Phys. **33**, 2884–2889 (2000).

90. B. Casabone, C. Deshmukh, S. Liu, D. Serrano, A. Ferrier, T. Hümmer, P. Goldner, D. Hunger and H. de Riedmatten. *Dynamic control of Purcell enhanced emission of erbium ions in nanoparticles - Nature Communications.* Nat. Commun. **12**, 1–7 (2021).

91. R. C. Hilborn. *Einstein coefficients, cross sections, f values, dipole moments, and all that.* Am. J. Phys. **50**, 982 (1998).

92. X. Cui, J. Lu, C. Gao, C. Hou, W. Wei and B. Peng. *Luminescence properties of Nd3+-doped Y2O3 nanoparticles in organic media.* Appl. Phys. A **103**, 27–32 (2011).

93. G. Kumar, J. Lu, A. Kaminskii, K.-I. Ueda, H. Yagi and T. Yanagitani. *Spectroscopic and stimulated emission characteristics of Nd/sup 3+/ in transparent Y/sub 2/O/sub 3/ ceramics.* IEEE Journal of Quantum Electronics **42**, 643–650 (2006).

94. W. K. Wootters and W. H. Zurek. *A single quantum cannot be cloned.* Nature **299**, 802–803 (1982).

95. J. J. Longdell, E. Fraval, M. J. Sellars and N. B. Manson. *Stopped Light with Storage Times Greater than One Second Using Electromagnetically Induced Transparency in a Solid.* Phys. Rev. Lett. **95**, 063601 (2005).

96. M. P. Hedges, J. J. Longdell, Y. Li and M. J. Sellars. *Efficient quantum memory for light.* Nature **465**, 1052–1056 (2010).

97. M. Nilsson and S. Kröll. *Solid state quantum memory using complete absorption and re-emission of photons by tailored and externally controlled inhomogeneous absorption profiles.* Opt. Commun. **247**, 393–403 (2005).

98. J. Dajczgewand, J.-L. Le Gouët, A. Louchet-Chauvet and T. Chanelière. *Large efficiency at telecom wavelength for optical quantum memories.* Opt. Lett. **39**, 2711–2714 (2014).

99. D. L. McAuslan, P. M. Ledingham, W. R. Naylor, S. E. Beavan, M. P. Hedges, M. J. Sellars and J. J. Longdell. *Photon-echo quantum memories in inhomogeneously broadened two-level atoms.* Phys. Rev. A **84**, 022309 (2011).

100. M. Afzelius, C. Simon, H. de Riedmatten and N. Gisin. *Multimode quantum memory based on atomic frequency combs.* Phys. Rev. A **79**, 052329 (2009).

101. M. Afzelius and C. Simon. *Impedance-matched cavity quantum memory.* Phys. Rev. A **82**, 022310 (2010).

102. H. de Riedmatten, M. Afzelius, M. U. Staudt, C. Simon and N. Gisin. *A solid-state light–matter interface at the single-photon level.* Nature **456**, 773–777 (2008).

103. M. Afzelius, C. Simon, H. de Riedmatten and N. Gisin. *Multimode quantum memory based on atomic frequency combs.* Phys. Rev. A **79**, 052329 (2009). URL `https://link.aps.org/doi/10.1103/PhysRevA.79.052329`.

104. P. Jobez, N. Timoney, C. Laplane, J. Etesse, A. Ferrier, P. Goldner, N. Gisin and M. Afzelius. *Towards highly multimode optical quantum memory for quantum repeaters.* Phys. Rev. A **93**, 032327 (2016). URL `https://link.aps.org/doi/10.1103/PhysRevA.93.032327`.

105. M. Businger, A. Tiranov, K. T. Kaczmarek, S. Welinski, Z. Zhang, A. Ferrier, P. Goldner and M. Afzelius. *Optical Spin-Wave Storage in a Solid-State Hybridized Electron-Nuclear Spin Ensemble.* Phys. Rev. Lett. **124**, 053606 (2020).

106. Y. Ma, Y.-Z. Ma, Z.-Q. Zhou, C.-F. Li and G.-C. Guo. *One-hour coherent optical storage in an atomic frequency comb memory.* Nat. Commun. **12**, 1–6 (2021).

107. P. Jobez, C. Laplane, N. Timoney, N. Gisin, A. Ferrier, P. Goldner and M. Afzelius. *Coherent Spin Control at the Quantum Level in an Ensemble-Based Optical Memory.* Phys. Rev. Lett. **114**, 230502 (2015). URL `https://link.aps.org/doi/10.1103/PhysRevLett.114.230502`.

108. K. Kutluer, E. Distante, B. Casabone, S. Duranti, M. Mazzera and H. de Riedmatten. *Time Entanglement between a Photon and a Spin Wave in a Multimode Solid-State*

Quantum Memory. Phys. Rev. Lett. **123**, 030501 (2019).

109. Q. Li, Y. Bao, A. Thuresson, A. N. Nilsson, L. Rippe and S. Kröll. *Slow-light-based optical frequency shifter.* Phys. Rev. A **93**, 043832 (2016).
110. Q. Li, A. Kinos, A. Thuresson, L. Rippe and S. Kröll. *Using electric fields for pulse compression and group-velocity control.* Phys. Rev. A **95**, 032104 (2017).
111. A. J. Meixner, C. M. Jefferson and R. M. Macfarlane. *Measurement of the Stark effect with subhomogeneous linewidth resolution in* Eu^{3+}*:*YAlO_3 *with the use of photon-echo modulation.* Phys. Rev. B **46**, 5912–5916 (1992). URL `https://link.aps.org/doi/10.1103/PhysRevB.46.5912`.
112. Y. P. Wang and R. S. Meltzer. *Modulation of photon-echo intensities by electric fields: Pseudo-Stark splittings in alexandrite and* YAlO_3*:*Er^{3+}. Phys. Rev. B **45**, 10119–10122(R) (1992).
113. F. R. Graf, A. Renn, U. P. Wild and M. Mitsunaga. *Site interference in Stark-modulated photon echoes.* Phys. Rev. B **55**, 11225–11229 (1997).
114. A. Arcangeli, A. Ferrier and Ph. Goldner. *Stark echo modulation for quantum memories.* Phys. Rev. A **93**, 062303 (2016).
115. A. L. Alexander, J. J. Longdell, M. J. Sellars and N. B. Manson. *Photon Echoes Produced by Switching Electric Fields.* Phys. Rev. Lett. **96**, 043602 (2006).
116. B. Lauritzen, J. Minář, H. de Riedmatten, M. Afzelius and N. Gisin. *Approaches for a quantum memory at telecommunication wavelengths.* Phys. Rev. A **83**, 012318 (2011).
117. N. Timoney, I. Usmani, P. Jobez, M. Afzelius and N. Gisin. *Single-photon-level optical storage in a solid-state spin-wave memory.* Phys. Rev. A **88**, 022324 (2013).
118. P. Jobez, C. Laplane, N. Timoney, N. Gisin, A. Ferrier, P. Goldner and M. Afzelius. *Coherent Spin Control at the Quantum Level in an Ensemble-Based Optical Memory.* Phys. Rev. Lett. **114**, 230502 (2015).
119. Q. Li. *Quantum memory development and new slow light applications in rare-earth-ion-doped crystals.* PhD thesis Atomic Physics, Department of Physics, Lund University Lund, Sweden (2018). URL `https://lup.lub.lu.se/search/publication/a16f47ae-8cef-45d4-95d8-db4e7c72dcd3`.
120. A. Amari, A. Walther, M. Sabooni, M. Huang, S. Kröll, M. Afzelius, I. Usmani, B. Lauritzen, N. Sangouard, H. de Riedmatten and N. Gisin. *Towards an efficient atomic frequency comb quantum memory.* J. Lumin. **130**, 1579–1585

(2010).

121. A. Kinos, L. Rippe, S. Kröll and A. Walther. *Designing gate operations for single-ion quantum computing in rare-earth-ion-doped crystals*. Phys. Rev. A **104**, 052624 (2021).

122. M. J. Thorpe, L. Rippe, T. M. Fortier, M. S. Kirchner and T. Rosenband. *Frequency stabilization to 6 × 10-16 via spectral-hole burning - Nature Photonics*. Nat. Photonics **5**, 688–693 (2011).

123. T. Instruments. *User's Guide - THS3491DDA Evaluation Module*. Texas Instruments (2018). URL `https://www.ti.com/lit/ug/slou480/slou480.pdf?ts=1647254720165&ref_url=https%253A%252F%252Fwww.google.com%252F`.

124. I. Roos and K. Mølmer. *Quantum computing with an inhomogeneously broadened ensemble of ions: Suppression of errors from detuning variations by specially adapted pulses and coherent population trapping*. Phys. Rev. A **69**, 022321 (2004).

125. L. Rippe, M. Nilsson, S. Kröll, R. Klieber and D. Suter. *Experimental demonstration of efficient and selective population transfer and qubit distillation in a rare-earth-metal-ion-doped crystal*. Phys. Rev. A **71**, 062328 (2005).

126. S. Muralidharan, L. Li, J. Kim, N. Lütkenhaus, M. D. Lukin and L. Jiang. *Optimal architectures for long distance quantum communication - Scientific Reports*. Sci. Rep. **6**, 1–10 (2016).

127. O. Gobron, K. Jung, N. Galland, K. Predehl, R. Le Targat, A. Ferrier, P. Goldner, S. Seidelin and Y. Le Coq. *Dispersive heterodyne probing method for laser frequency stabilization based on spectral hole burning in rare-earth doped crystals*. Opt. Express **25**, 15539–15548 (2017).

128. D. R. Leibrandt, M. J. Thorpe, C.-W. Chou, T. M. Fortier, S. A. Diddams and T. Rosenband. *Absolute and Relative Stability of an Optical Frequency Reference Based on Spectral Hole Burning in* Eu^{3+}:$\mathbf{Y}_2\mathrm{SiO}_5$. Phys. Rev. Lett. **111**, 237402 (2013). URL `https://link.aps.org/doi/10.1103/PhysRevLett.111.237402`.

129. L. Ma, O. Slattery and X. Tang. *Single photon frequency up-conversion and its applications*. Phys. Rep. **521**, 69–94 (2012).

130. M. Rančić, M. P. Hedges, R. L. Ahlefeldt and M. J. Sellars. *Coherence time of over a second in a telecom-compatible quantum memory storage material*. Nat. Phys. **14**, 50–54 (2018).

131. T. Böttger, Y. Sun, C. W. Thiel and R. L. Cone. *Spectroscopy*

and dynamics of $\mathrm{Er}^{3+}:\mathrm{Y_2SiO_5}$ *at* 1.5 μm. Phys. Rev. B **74**, 075107 (2006). URL `https://link.aps.org/doi/10.1103/PhysRevB.74.075107`.

132. T. Böttger, C. W. Thiel, R. L. Cone and Y. Sun. *Effects of magnetic field orientation on optical decoherence in* $Er^{3+}:Y_2SiO_5$. Phys. Rev. B **79**, 115104 (2009). URL `https://link.aps.org/doi/10.1103/PhysRevB.79.115104`.

133. N. Timoney, B. Lauritzen, I. Usmani, M. Afzelius and N. Gisin. *Atomic frequency comb memory with spin-wave storage in 153Eu3 +:Y2SiO5.* J. Phys. B: At. Mol. Opt. Phys. **45**, 124001 (2012).

134. M. Nilsson. *Coherent Interactions in Rare-Earth-Ion-Doped Crystals for Applications in Quantum Information Science.* PhD thesis Atomic Physics (2005). Defence details Date: 2005-01-21 Time: 10:15 Place: Sal F, Fysiska Institutionen, Lund External reviewer(s) Name: Schmiedmayer, Jörg Title: Professor Affiliation: Physikalishes Institut, Universität Heidelberg —.

135. P. Jobez, I. Usmani, N. Timoney, C. Laplane, N. Gisin and M. Afzelius. *Cavity-enhanced storage in an optical spin-wave memory.* New J. Phys. **16**, 083005 (2014).

136. A. A. Kalachev. *Quantum memory based on optical subradiance: Optimization of the signal-to-noise ratio.* Bull. Russ. Acad. Sci.: Phys. **72**, 691–694 (2008).